Human skin investigations using nonlinear spectroscopy and microscopy

Xueqin Chen

ÉCOLE CENTRALE DE MARSEILLE

École Doctorale - Physique & Sciences de la Matière

THÈSE DE DOCTORAT

pour obtenir le grade de
DOCTEUR en Sciences de l'ÉCOLE CENTRALE de MARSEILLE
Discipline : Optique, photonique et traitement d'image

Human Skin Investigations using Nonlinear Spectroscopy and Microscopy

Développements en spectroscopie et microscopie non linéaire pour l'étude morphologique et fonctionnelle de la peau humaine

Xueqin CHEN

Soutenue le 11 Décembre 2014

Dr. Bernard Schoot	Président du jury
Dr. Nicolas Tricaud	Rapporteur
Pr. Richard Guy	Rapporteur
Dr. Sophie Brasselet	Examinateur
Dr. Hervé Rigneault	Directeur de thèse
Dr. Jean-Baptiste Galey	Co-directeur de thèse

Institut Fresnel - CNRS UMR 7249 - Équipe MOSAIC

Abstract

Skin is an organ that envelops the entire body, acts as a pivotal, efficient natural barrier towards various invaders. For the treatment of major dermatological diseases and in the cosmetic industry, topical applications on skin are widely used, thus many efforts in skin research have been aimed at understanding detailed molecular absorption and efficient penetration mechanisms. However, it remains difficult to obtain high-resolution visualization in 3D together with chemical selectivity and quantification in skin research. Nonlinear spectroscopy and microscopy, including two-photon excited fluorescence (TPEF), spontaneous Raman scattering, coherent anti-Stokes Raman scattering (CARS) and stimulated Raman scattering (SRS), are introduced in this work for unambiguous skin morphological identification and topical applied molecules detection. Several quantitative methods based on nonlinear spectroscopy and microscopy are designed for 3D chemical analysis in reconstructed skin, *ex vivo* and *in vivo* on human skin. Furthermore, to adapt to forthcoming clinical applications, an endoscopic design is investigated to bring nonlinear imaging in flexible endoscopes.

Keywords : skin, sweat gland, *in vivo*, nonlinear spectroscopy and microscopy, endoscopy

---

Résumé

La peau est un organe qui enveloppe le corps, elle est une barrière naturelle importante et efficace contre différents envahisseurs. Pour le traitement des maladies dermatologiques ainsi que dans l'industrie cosmétique, les applications topiques sur la peau sont largement utilisées. Ainsi beaucoup d'efforts ont été investis dans la recherche sur la peau visant à comprendre l'absorption moléculaire et les mécanismes rendant efficace la pénétration. Cependant, il reste difficile d'obtenir une visualisation 3D de haute résolution combinée à une information chimiquement spécifique et quantitative dans la recherche sur la peau. La spectroscopie et la microscopie non-linéaire, incluant la fluorescence excitée à 2-photon (TPEF), la diffusion Raman spontanée, la diffusion Raman cohérente anti-Stokes (CARS) et la diffusion Raman stimulée (SRS), sont introduits dans ce travail pour l'identification sans ambiguité de la morphologique de la peau et la détection de molécules appliquées de façon topique. Plusieurs méthodes quantitatives basées sur la spectroscopie et la microscopie non-linéaire sont proposées pour l'analyse chimique en 3D sur la peau artificialle, *ex vivo* et *in vivo* sur la peau humaine. De plus, afin de s'adapter aux applications cliniques à venir, un design endoscopique est étudié pour permettre l'imagerie non-linéaires dans les endoscopes flexibles.

Mots clefs : peau, pore sudoral, *in vivo*, spectroscopie et microscopie non-linéaire, endoscopie

Acknowledgement

I would like to express the deepest appreciation to my PhD jury members: the president of jury **Dr. Bernard SCHOOT**, the reviewers **Dr. Nicolas TRICAUD** and **Pr. Richard GUY**, the examiner **Dr. Sophie BRASSELET**, my supervisor **Dr. Hervé RIGNEAULT** and co-supervisor **Dr. Jean-Baptiste GALEY**. I am appreciate that they accepted to be my jury and evaluated my PhD work, thanks for all the discussions and advices.

Thanks to Chinese Education China Scholarship Council (CSC), Centre National de la Recherche Scientifique (CNRS), Ecole Centrale de Marseille and Institut Fresnel, they gave me an opportunity to start this nice work and supported me to finish my PhD study. Especially, I would like to thank MOSAIC group, it is a pleasure to work in such a great team.

This PhD work has been supervised by **Hervé RIGNEAULT**, I really appreciate his brilliance and guidance in my PhD study. I have enjoyed so much to work with him during these years, he was guiding me in doing research but also gave me the freedom to discover this field by my curiosity. Most importantly, I can never went so far without his trust and encouragement, in research and in my life.

I have to thank my co-supervisor **Jean-Baptiste GALEY** from LÓréal Recheche Avancée, for his guidance and patience in the experiments and my thesis writing, especially for answering my endless questions. I appreciate the contributions of **Florian FORMANEK** and **Sébastien GRÉGOIRE** to this project, thanks for their fully support for my PhD work.

I started my PhD work with **Alicja GASECKA**, who gave me the first guidance of the experiments. She was teaching me every details about the experiments and guiding me among all the labs, which makes me miss her so much after she moved to Canada. Besides, she is strict in research and works very hard, this attitude affected me a lot in my following work.

Then I continued to work with **Paulina GASECKA**, thanks for all the good time shared with her, especially for some funny in vivo experiment. I cannot forget the time when we were doing experiments on each other and trying to scare each other to active the "sweat event".

Pascal BERTO and me made a good team in working, I have enjoyed to work with him and have learnt most of the basic optics from him. I still remember how he encouraged me to try once more when i was so desperate with the experiments. Thank him also for the "french learning" time and "ping-pong" time!

At the last year of my PhD, I proposed myself to Herv'e that I would like to work more on optics instead of biological applications. I definitely appreciate that he accepted and gave me the chance to try, it was not easy especially for a person who doesn't have background on optics but I do enjoyed a lot. Since then I started the project on photonic fibers and I did not hesitate to bother **Esben ANDRESEN** to supervise me. He had helped me so much in the experiments

and in the thesis writing. It is such a nice experience to work with him, because he is so nice and patient that I cannot even find a way to make him angry.

Besides the people I have worked with, I would like to thank also: **Sophie BRASSELET**, who introduced me the first day to the lab. Her warm welcome relaxed me from my first arrival in France and makes me feel like a big family in MOSAIC group; **Patrick FERRAND**, who always responses to all my requests of the software; **Julien SAVATIER**, who helped me in the biological work. Thanks him also for the summer barbecue! **Jérôme WENGER**, who guided me in the spontaneous Raman setup. Thanks for his patient guidance when I was a freshman in a optical lab (he didn't kick me out even once I put oil on a water objective)!

Furthermore, I would like to go give a big hug to all my friends whom I met in Fresnel. Thanks for their company during this years, I do enjoyed the time with them: **Wang Xiao**, who brought me to the lab for the first time; **Zola**, who gave me a first tour in nonlinear setup; **Cesar**, who brought me to my first lunch in the University Restaurant; **Zhang Yi** and **Shu Da**, who celebrated my first birthday 10 days after my arrival in France; **Wiktor**, who is my big adversary in playing ping-pong; **Naveen**, who unfortunately sits behind me in the office, so that I had bothered him with optical and English questions during 3 month of writing. Especially, I would like the thank **Sarah**, **Deep**, **Haitham** and **Sherazade**, who graduated in the same year as me, I am so glad to share the writing time with them and to have their supports. And also the other friends that I didn't mention here, thank them all for their friendships.

Three years passed just in a wink, but I appreciate for all the beautiful memories I could have with them.

At the end, I have to say thanks to my family, for their love, understanding and support. Thank my parents for teaching me to be independent, to be responsible, and to have a thankful heart, which is a treasure of my life. Thank my sister who always support me no matter in any situation. I love them as always.

致谢

首先我想对我的博士答辩评委会致以最真挚的感谢：委员会主席**伯纳·SCHOOT博士**，论文评审**尼古拉斯·TRICAUD博士**和**理查德·GUY教授**，评委**索菲·BRASSELET博士**，导师**埃尔维·RIGNEAULT博士**以及合作导师**让-巴蒂斯特·GALEY 博士**。感谢他们愿意作为答辩评审来评估我的博士工作，以及在答辩过程中的讨论和建议，对我的未来工作有很大的帮助。

感谢中国国家留学基金委，法国国家科学院，法国马赛中央理工大学，菲涅尔光学研究所支持我完成博士工作。尤其要感谢我所在的实验室-“马赛克”，我很高兴自己能够在这样一个团结和愉快的团队中开展这几年的工作。

该博士论文以及相关工作由菲涅尔研究所的**埃尔维·RIGNEAULT**指导。我很高兴也很享受这些年和他一起的工作，他不但在学术研究中给我适时的引导，同时也给我一定的自由，让我可以独自探索和尝试。更重要的是他的信任和鼓励，让我可以在这个研究领域不断前行。

感谢我的合作导师，来自欧莱雅研发中心的**让-巴蒂斯特·GALEY**。感谢他这几年对我耐心的指导，尤其是耐心的回答我无止境的问题，无论在实验中还是在写论文的过程中。同时感谢同样来自欧莱雅研发中心的**弗洛里安·FORMANEK**和**塞巴斯蒂安·GRÉGOIRE**对这项工作的贡献，以及他们对我博士工作的支持。

爱丽丝·GASECKA是第一个在实验室带我工作的人。在工作中，她对我事无巨细的指导，教给我每个实验细节，向我讲解所有的实验设备。在跟随她工作的半年时间里，我看到了她的努力和对研究工作的谨慎，这种工作态度在后续工作中给了我很大的影响。

之后就开始了和**宝琳娜·GASECKA**的合作，感谢那些与她分享的美好的时间，特别是那些有趣地活体实验。我们在彼此身上做实验，并且想尽办法吓唬对方来刺激“流汗过程”的发生。

帕斯卡·BERTO和我是一个很好的合作团队，很喜欢和他一起工作，也从他身上学到了很多光学的基础知识，对我后来的工作有很大的帮助。还有这些年中他给我的鼓励，总是在我做实验到瓶颈的时候，他鼓励我在尝试一次，让我学会了从不放弃。另外还有感谢和他分享的法语时间和乒乓球时间。

在我博士研究的最后一年，我向导师埃尔维提议要从生物医用方向转到光学方向。我真的非常感激他能够同意并且给我这个尝试的机会。对于一个没有光学背景的人来说这并不是一件容易的事，但是我非常享受这个工作过程。于是从那时起，我便开始了在光纤方面的工作，**艾斯本·ANDRESEN**在这一部分工作上，以及在最后论文的写作上，给了我很大的帮助和指导。和他一起工作是一个很开心的过程。

除了曾经一同工作过的人以外，我还要感谢:**索菲·BRASSELET**，她除了关心我的工作以外，也十分关心我的日常生活，我还记得在我博士学习的第一天，她友好的欢迎，让我初来法国的紧张感一扫而光，也让我感觉到“ 马赛克”像一个大家庭；**帕特里克·FERRAND**，他总是帮助我解决软件方面的问题; **于连·SAVATIER**，感谢他在生物工作方面给我的帮助，也感

谢他的烧烤聚会；**杰罗姆·WENGER**；感谢在我博士初期时候他在光学实验室给我的耐心指导(尽管他的严格人尽皆知，但是有一次我在水浸物镜上加了油，他居然没有吃了我).

此外，我希望给我在菲涅尔遇见的朋友们一个大大的拥抱，非常感谢这些年里他们的陪伴:第一天把我带到实验室的师兄**王潇**；第一次带我参观非线性实验设备的**左拉**；带我去学校食堂吃了第一顿午饭的**凯撒**；在我到达法国10天后和我一起庆祝了第一个生日的**张益**和**舒达**；乒乓球上我的强劲对手**维克多**；教我练瑜伽的**苏丝米塔**；办公室里坐在我后面的**纳威恩**，在我写论文的三个月里不得不回答我的各种关于光学或英语的问题。另外, 还要特别感谢和我同一年毕业的**萨拉**，**蒂普**，**海什木**和**舍赫拉查德**，和高兴能和他们一起分享写论文以及毕业答辩的这段时光，互相的支持和鼓励。以及其他我没有提到名字的朋友们，感谢他们的友谊，这是我在法国生活的一个重要部分。

三年的时光就在一转眼间过去，但我很感激能有这些和你们一起的美好回忆。

最后，我要感谢我的家人，感谢他们的爱，理解和支持。感谢我的父母教会我独立，负责和有一颗感恩的心脏，这些都是我生命中的无价财富，感谢无论在任何情况下都会支持我的姐姐。我爱他们一如既往。

Contents

Introduction

In the long history of the development of human civilization, we have been continuously studying and understanding ourselves from all aspects, anatomically, physiologically, psychologically and sociologically. However, among all the research, the most basic, and one of the most important subject, is to study the structure and functions of the human body which still baffles doctors and researchers despite thousands of years of biological and medical research. The human body is an incredibly complex, intricate yet fascinating system where: bones and muscles are organized to build the physical structure, the heart and organs are small systems working together to maintain life body functions and the brain is the controlling and information processing center. All of those are connected by vessels and they communicate through neural networks systematically and dependently to maintain life activities [1]. However, at the same time, human body system is quite fragile and it cannot be exposed to the external environment, that is why the skin is needed to be an interface between human body and its environment as the "monumental facade of the human body" as described by Comel in 1953 [2].

Generally, skin is an organ which covers the largest surface of human body with many and varied topographic differences: hairless in some areas where it is thick, horny and taut; whereas downy or hairy in others where it is thin, translucent and lax. The difference in characteristic properties in skin does not only exist in different regions of the body or in different individuals, but even in the same individual with aging. Knowledge of normal skin involves a familiarity with these and many other varying factors, an understanding of the factors that brought them about, and an awareness of the basic similarities in all skin regardless of apparent differences [3]. In contrast to other epithelial tissues such as the lungs or the intestines, the skin is unique by its multi-layered architecture and the presence of a cornified epithelium that acts as a pivotal, efficient natural barrier towards various

invaders [4] and to prevent water loss from the body. Besides, for the other function of body processes such as sensation, insulation and temperature regulation, there are numerous appendages located in skin in relation to these functions (such as sweat glands, hair shafts, nails and nerves). For example, eccrine sweat glands that are located over almost the entire skin surface, is responsible for thermoregulation.

Ever since the 17th century, Italian physician and biologist Marcello Malpighi (1628 - 1694) first systematically introduced the microscope to anatomy research, facilitating the discovery of skin layers. He divided the epidermis (skin surface) into an inner layer of viable cells (stratum Malpighi: named after Marcello Malpighi) and an outer one of anucleated horny cells (stratum corneum) [5]. Later on, staining and histochemical procedures were used together with light microscope or electron microscope to visualize the micro-anatomy of the epidermis. The stratum Malpighi was then subdivided, from outer to inner, into a granular layer (stratum granulosum) which contains various-sized keratohyalin granules easily stainable with many basic dyes, a spinous layer (stratum spinosum) of variable thickness, and a basal layer (stratum basale) in contact with dermis [3,6].

Today, aided by the vast advances in technology, the extension and deepening of skin research is evident at all levels, from purely morphological observation to functional study. Firstly of all, more detailed information of skin can be described such as the lipid organization and behavior [7] as well as the melanin and hemoglobin content in skin [8]; Secondly, skin appendages are investigated comprehensively, for instance, the distribution of eccrine sweat pores and sweating events are studied by optical coherence tomography (OCT) [9], or the mechanical properties of hair of different ages and ethnic origins are observed by by a variety of techniques such as Scanning Electron Microscope (SEM) [10]. Furthermore, dermatological diseases were more noticed and the related research has remarkably increased such as melanoma and vitiligo investigations.

Apart from studying skin itself, another major aspect in skin research is to understand detailed molecular transfer mechanisms through skin since the topical application of pharmaceutical or cosmetics products is widely used. However, predicting the penetration of a given active formulation in/through the skin remains very difficult even for small molecules due to the highly complex nature of the structures and mechanisms that constitute the delivery pathways. Stratum corneum (SC), the outermost layer of the skin epidermis,

exhibits a low permeability that is related to highly organized intercellular lamellar lipids composed of ceramides, fatty acids and cholesterol [7]. An understanding of the underlying mechanisms of how active molecule penetrates into skin requires detailed anatomical information, quantitative 3D concentration mapping and time course experiments, ideally on the same sample and possibly applied *in vivo*. This is far from conventional skin bioavailability approaches used to quantify active compound penetration in skin following topical application. Classical approach uses *ex vivo* human skin mounted on Franz cell diffusion set-up [11] and many appropriate validated analytical methods to quantify chemicals (in SC, epidermis, dermis and subcutaneous receptor fluid) such as liquid scintillation counting with radio-labelled compounds [12] or liquid chromatography-tandem mass spectrometry (LC/MS/MS) [13], but these approaches are not compatible with *in vivo* applications. The other, which can be used *in vivo*, involves sequential adhesive tape stripping of SC and chromatographic analyses of compounds of interest after strip extraction to determine concentration profile across outermost layers of skin at specific time points [14] [15]. Although such analysis can provide active molecule concentration profile along the skin depth, it is destructive and does not reveal 3D penetration pathways. Overcoming the limitation of chemical methods, label free imaging techniques such as high-frequency ultrasound imaging [16], optical coherence tomography [17], nonlinear optical microscopy (two-photon excitation fluorescence, TPEF [18, 19], second harmonic generation, SHG [20] and third harmonic generation, THG [21]) have proved to reveal morphological skin information but they fail to provide the chemical specificity required to study molecular percutaneous penetration and absorption. On the contrary vibrational imaging, such as coherent anti-Stokes Raman scattering (CARS) [22] and stimulated Raman scattering (SRS) [23, 24], provide high molecular selectivity by granting access to the characteristic vibrational signature [25–27]. These techniques have been efficiently used together with TPEF/SHG/THG to distinguish specific molecules along with the morphological information of biological samples. Concerning skin research, SRS has been recently reported to image drug delivery into *ex vivo* mice skin [28] and porcine skin [29]. Unfortunately, the proposed approaches were not capable of providing unbiased concentration of active compounds for quantitative analysis. One of the reasons for this is that SRS signal is attenuated with increasing depth of skin samples that preclude its linear relationship with molecular concentration.

Furthermore, reviewing the experimental studies on skin, they are mostly limited by

the region of human body because of the flexibility of setup and by the observation depth under the surface, thus, this is still far from industrial or clinical applications where more flexible, stable, operable and compact equipment is required. For this purpose, optical fibers have been considered to transfer microscopic techniques in endoscopic research. Flexible endoscope can overcome the limitation of skin region accessibility and can penetrate deep into the human body. With respect to label free methods, advanced endoscopic contrast schemes have been reported for two-photon excited intrinsic fluorescence, second-harmonic generation [30], optical coherence tomography [31] and spontaneous Raman spectroscopy [32]. However, for vibrational imaging (CARS and SRS), there still remains a challenge for the invention of fiber-based probes. Xie *et al.* has designed one of such probe based on solid optical fiber for multimodal imaging with CARS, TPEF and SHG [33], but the strong four-wave mixing (FWM) contribution generated in the delivery fiber (silica) under typical vibrational imaging excitation conditions was then noticed. It forms a large background that is overwhelming the signal generated at the sample plane and severely complicates the interpretation of the result. Afterwards, this design has been improved by filtering the fiber-generated FWM radiation before the excitation lasers are delivered to the sample. However, the complex multiple nonlinear process is difficult to be totally removed, and this will limit the flexibility of laser wavelength tuning range. Additionally, the back reflected signal has to be collected with another separated fiber [34] in those solid-fiber based endoscope systems. As an alternative, hollow-core fiber design is interesting for nonlinear imaging endoscope development, it allows the propagation of multiple wavelengths without interaction with the fiber since the light propagates inside the air fiber core, thus, there is no nonlinear processes happening within the fiber. To date, Saar *et al.* have developed an optical-fiber-delivered coherent Raman scattering (CRS) imaging systems [35], where they delivered the excitation beams of CARS and SRS through the fiber, but the scattered signal was detected directly in the forward direction. On the other hand, the backward reflected CARS and SRS signals were collected by using double-clad hollow-core fiber [36] with an "endoscope-like" scheme, where the image scanning was achieved by using a scanning microscope. Although the signal was collected back to the input side of the fiber by the second cladding, this system failed to image biological tissues due to the narrow transmission range of hollow-core fibers.

In summary, skin research is comprehensively developed so far in the level that skin and skin appendages are mostly understood structurally and functionally. Nevertheless,

for studying topical percutaneous penetration and absorption, a technique that can provide high-resolution visualisation of molecular delivery in skin and chemically analysed quantification as well as an unambiguous skin morphological identification, possibly with a suitable fiber-delivered probe for *in vivo* and *in situ* application, is currently lacking. In this thesis, focusing on skin study, we investigated an effort to achieve this goal, proper techniques and quantification methods were designed and applied respectively on skin and eccrine sweat pore. Finally we adapted our optical system to investigate the excitation laser delivery and collection using a new type of hollow-core fibers, in the perspective of future endoscopic developments.

The manuscript is organized as follows:

Chapter 1 presents the physical part of this work, label-free nonlinear microscopy including two-photon excited fluorescence (TPEF) and coherent Raman scattering (CRS) is presented and the optical setup is introduced.

Chapter 2 focuses on the molecular cutaneous absorption of human skin and describes a framework for imaging and reconstructing molecular concentration. Quantitative 3D skin active compounds mapping together with detailed skin morphological identification are provided.

Chapter 3 involves *in vivo* applications on human hand for studying the distribution and mechanism of antiperspirant salts. Individual eccrine sweat pores and sweating process are studied, and statistical analysis of time sequence quantification is elucidated.

Chapter 4 describes the development of an "endoscope-like" system for nonlinear imaging and its application on biological tissue. Thus, it opens nonlinear imaging technique towards industrial and clinical applications.

Chapter 1

Nonlinear optical spectroscopy and microscopy

The constant evolution of optical microscopy over the past century has been driven by the desire of (i) improving the spatial resolution to image ever smaller entities and (ii) improving image contrast and enhancing physical and chemical specificity for a better characterization of specimens.

In conventional optical microscopy, the emission happens following a linear interaction when an excitation laser passes through the sample [37]. In order to increase optical resolution and contrast, a (spatial) pinhole is added on the confocal plane of the lens to eliminate out-of-focus light, it is called confocal microscopy [38]. It has been used in combination with spectroscopic techniques such as fluorescence, infrared or Raman spectroscopy, acting as contrast mechanism to achieve high physical or chemical specificity. This has been successfully applied to the study of wide range of materials with good spectral resolution. However, their spatial resolution is restricted by the diffraction limit that imposed by the wavelength of the probe light, which is insufficient to resolve sub-micron structures [39].

Nonlinear optical microscopy, which embraces any microscopy technique based on nonlinear optics [40], has opened a new door to the technical improvement and broadened the range of biological applications. It overcomes several important drawbacks of linear

microscopy: the nonlinear process takes place only at focus point when the photon density is sufficiently high, which eliminates out-of-focus excitation and generates better contrast without the need of a confocal pinhole, thereby, nonlinear microscopy enables 3D optical sectioning with high spatial resolution [41]. Second-order nonlinear processes such as second harmonic generation (SHG) or sum frequency generation (SFG) are intrinsically sensitive to symmetry breaks and can be used to characterize inhomogeneities, impurities, formation of domains on surfaces or buried interfaces, which are suited for *in situ* real-time investigations. On the other hand, third-order processes such as two-photon excited fluorescence (TPEF), coherent anti-Stokes Raman scattering (CARS) and stimulated Raman scattering (SRS) microscopies are of interest for the study of thick structures. The signal generated by third-order processes scales with the cube of the excitation intensity, the focal excitation volume is therefore greatly reduced, the depth resolution is enhanced and the out-of-focus background is reduced [39]. Thus, nonlinear optical microscopies are widely applied for imaging deep structures of biological tissue in real-time with three dimensional optical sectioning capability.

In this thesis, we take advantage of nonlinear optical microscopies - TPEF, CARS and SRS - in combination with a spectroscopic technique - spontaneous Raman spectroscopy - to achieve the goal of identifying specific molecules in thick tissue *in vivo*. TPEF microscopy is used to image the native morphology of biological samples whereas spontaneous Raman, CARS and SRS - all vibrationally sensitive techniques - are applied to identify specific chemical compounds. In this chapter, the fundamentals of nonlinear optical microscopies and the experimental optical system used in most of the work (except the endoscopic development, see Chapter 4) are introduced.

1.1 Two-photon excited fluorescence

1.1.1 One-photon and two-photon fluorescence

In one-photon fluorescence excitation, the electronic transition from ground to excited state is induced by absorbing a photon with energy equal to or higher than the transition energy. The energy of a photon is only determined by its frequency υ (or wavelength

λ) [42]:

$$E = h\upsilon = hc/\lambda \tag{1.1}$$

where h is Planck's constant ($\approx 6.63{\times}10^{-34}$ J $\cdot$ s) and c is the speed of light ($\approx\ 3 \times 10^{8}$ m/s).

Thus, in one-photon fluorescence process, one photon (ω) excites a fluorescent molecule from the electronic ground state to the electronic excited state. After the excitation, the molecule relaxes to the lower vibrational level of the electronic excited state, then emits one photon of fluorescence and returns to the electronic ground state (Fig. 1.1). In this process, due to the intramolecular vibrational relaxation, the energy of emission is less than excitation, thereby the frequency of emitted photon is less than the absorbed photon ω.

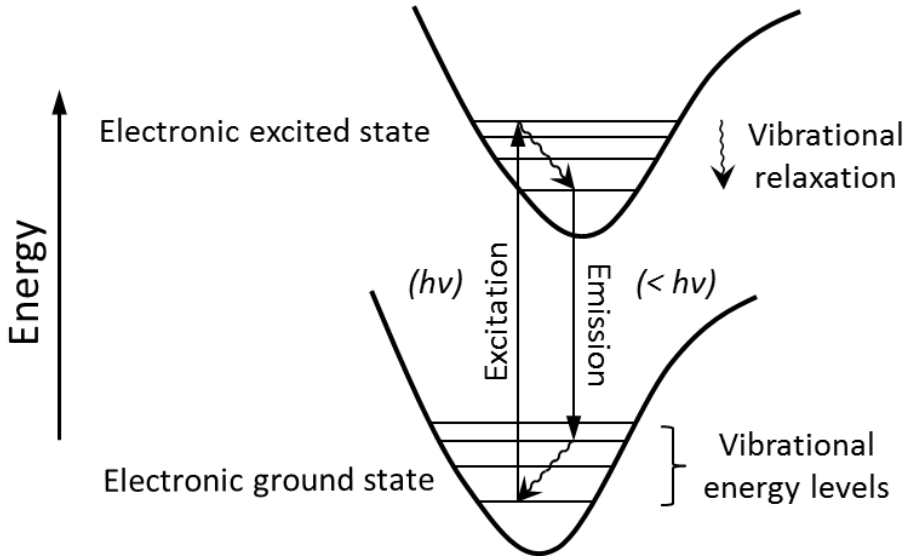

Figure 1.1: Energy transition of one-photon excited fluorescence process.

This is a linear process where the intensity of the emitted fluorescence depends linearly on the excitation intensity.

TPEF, on the other hand, has a different absorption process: two photons, each having roughly half the energy of the ground to excited state energy difference, excite a fluorescent molecule in one quantum event. This process depends on simultaneous absorption, where both photons have to interact with the fluorescent molecule at the same time. During

the absorption process, an electron of the molecule is transferred to the electronic excited state via a virtual state, after that the fluorescent emission occurs from the same excited level as one-photon fluorescence emission to the ground state (Fig. 1.2).

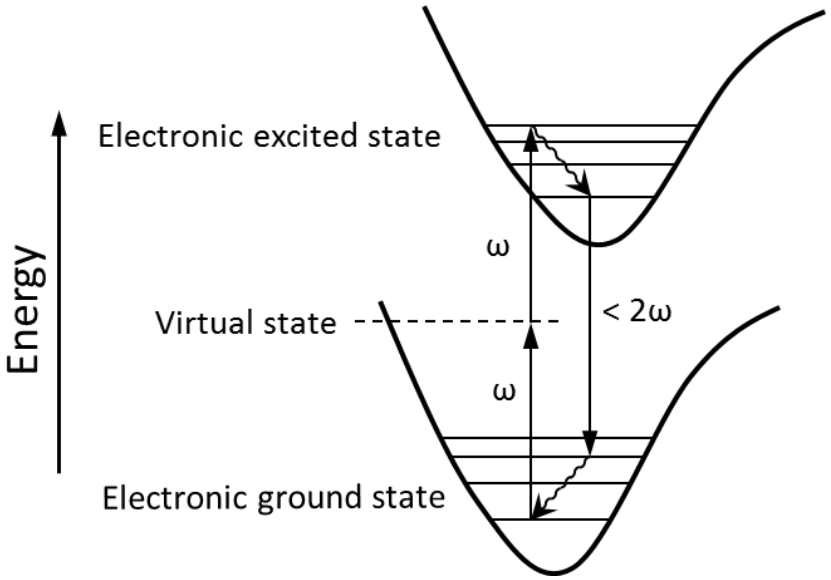

Figure 1.2: Two-photon excited fluorescence process.

TPEF requires on the order of one million times higher photon density than one-photon fluorescence in order to generate an equal number of absorption events. Because the virtual absorption (excited to a virtual state) of the first photon lasts only for a very short period ($10^{-15} - 10^{-12}$ s) [40], the second photon has to be absorbed during this short time to reach the excited state. Thus, extremely high laser intensity is required to generate significant two-photon-excited fluorescence. This intensity level can be easily achieved by focusing mode-locked (pulsed) lasers, in which the power during the peak of the pulse is high enough to generate significant two-photon excitation, while the average laser power remains fairly low. For instance, a Ti:Sapphire laser, the commonly used light source for TPEF microscopy, emits 1 W average power in pulses of 100 fs duration at a repetition rate of 80 MHz. This results in peak power of up to 125 kW at the peak of every pulse and peak intensity of up to 1.25×10^{10} kW/cm^2 when focused (depending on the size of focus spot). The frequency of the emitted photon is less than 2ω due to the intramolecular vibrational relaxation and the resulting fluorescence intensity goes as the square of the excitation intensity, this quadratic relationship between excitation and emission gives rise to many of the significant advantages associated with two-photon

excitation microscopy.

1.1.2 Two-photon fluorescence microscopy

The concept of two-photon excitation was described by Maria Goeppert-Mayer in her doctoral thesis on the theory of two-photon quantum transitions in atoms in 1931 [43], and was experimentally observed in caesium vapor after the development of laser sources [44]. TPEF microscopy exhibits several advantages over one-photon fluorescence microscopy. Firstly, this process takes place only at the focus point of microscope objective, because only at the focus the photon density is sufficiently high that two photons can be simultaneously absorbed by the fluorophore, which eliminates out-of-focus excitation of a fluorophore and thereby enable 3D optical sectioning with high spatial resolution [41]. Zipfel *et al.* shows an example of comparison between one-photon and two-photon fluorescence (Fig. 1.3), the one-photon process happens not only on the focal plane but also in the cone of the excitation beam [37] whereas the two-photon process happens only on the very high local intensity point provided by the tight focus, which results directly in the high resolution (sub-micrometer) imaging by TPEF microscopy [45].

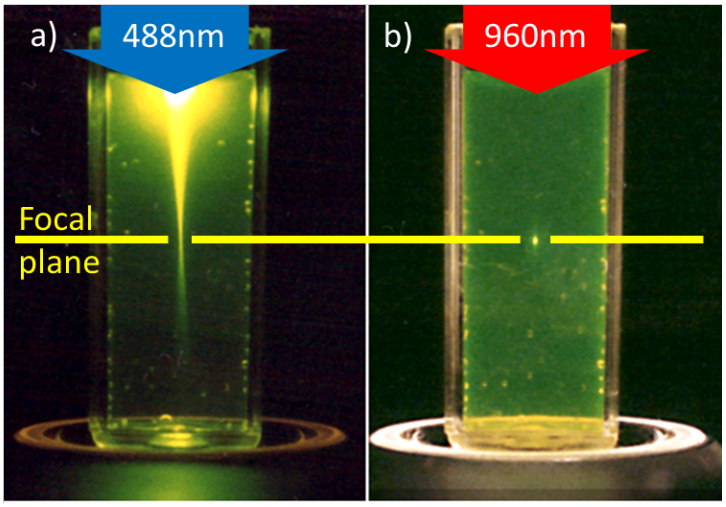

Figure 1.3: One-photon and two-photon excited fluorescence (image adapted from [37]).

Another advantage of TPEF process is the reduction of scattering which is a major contributor to image deterioration. Indeed, the elastic scattering of light is proportional

to the inverse power of the wavelength ($1/\lambda^4$), this process is less pronounced in TPEF because the excitation wavelength in TPEF is two times of that in one-photon fluorescence, this property allows TPEF imaging in three times deeper regions compared to one-photon fluorescence [41]. Thus, TPEF microscopy is ideal for deep-tissue imaging, it has been used to image mouse brain with fluorescent dyes [46] down to a depth of 1 millimeter.

1.1.3 Literature review

During long time, the microscopic application of TPEF was limited by its acquisition time (frame rates between 0.5 - 10s [47]), until the development of laser-scanning microscope in 1995. A line-scanning approach [48, 49], which reduces image acquisition time by covering the image plane with a line instead of a point, and a multifocal system [50, 51], which focuses the incident laser into multiple focus spots at the field aperture plane to obtain an image, have been taken to bring two-photon imaging speed to the video rate (approximately 30 frames/s). Later on, the point-scanning system, where a fast rotating polygonal mirror is used to scan the laser beam (focus point) in X-axis, and a galvanometric mirror is used to scan in Y-axis, is developed to rapidly raster scanned the laser beam across a sample plane [47]. In this case, the CCD camera can be replaced by a single-pixel detector such as a photomultiplier tube or an avalanche photodiode, that breaks the resolution and acquisition time limitation of CCD camera and can further improve the image resolution by removing the dependence on the emission point-spread function [47]. Point-scanning system has been improved (use two galvanometric mirrors [52]) and used until now such as our experimental setup (see Fig. 1.13), TPEF is finally available for high-speed, submicrometer resolution and 3D imaging that can be used for a broad area of biological applications [53].

The photodamage of living cells and tissues is another important limitation for live-cell imaging, the involve of high peak-power pulsed laser [45] with moderated mean power levels and the use of infrared or near-infrared illumination in TPEF microscopy minimized both photodamage and linear absorption to biological samples, which results in other important advantages, including greater sample penetration and increased cell and tissue viability [54]. These factors are extremely important for living cell and tissue imaging over extended periods of time. Together with the use of intrinsic autofluorescence of

tissue, TPEF microscopy has a large interest for bio-imaging applications especially for *in vivo* applications, for instance, skin morphology and dynamic process have been explored *in vivo* by this technique [55, 56]. Further developed TPEF microscope by endoscopic technique, can be even used to image freely moved biological objects with high resolution [57].

1.2 Spontaneous Raman spectroscopy

To identify a specific molecule in biological tissue, TPEF microscopy is not suitable if that molecule is not fluorescent. In some cases, the molecules can be labelled by a fluorescent marker but this approach can affect the complex molecular interaction in tissues and is hardly to be applied *in vivo*. An alternative label-free microscopy is required which exhibits molecular sensitivity and chemical specificity in order to produce biologically relevant images, and ideally can work at video rates to suit *in vivo* investigations.

Vibrational contrast is based on the intrinsic vibrational modes of molecules, to identify and visualize a specific molecule by meeting the molecular vibrational signature. The vibrational spectroscopies and microscopies stand out by their label-free chemical specificity.

1.2.1 Resonance phenomenon

To understand the fundamentals of vibrational contrast, we introduce first a simple mechanic model of the harmonic oscillator before explaining the molecular vibrational mode. On the molecular electronic ground state close to the minimum of potential energy surface (PES), the PES can be approximated by a parabola (consider only one-dimension), hence the harmonic solution is proposed.

A harmonic oscillator is an ideal oscillator whose evolution over time is described by a sine wave of constant amplitude and frequency of which depends only on the the system characteristics. In a forced regime, suppose the vibrational frequency of a spring oscillator is ω and that it is driven with a periodic force $F(t) = F_0 \cos(\omega t)$ where F_0 denotes the

amplitude of the force, at the frequency of ω. The response amplitude $x(\omega)$ with the dependence on the excitation force $F(t)$ is written as [58]:

$$x(\omega) = \frac{F(t)/m}{{\omega_0}^2 - \omega^2 - i2\gamma\omega} \tag{1.2}$$

where γ is the damping rate.

According to Eq. 1.2, when ω is approaching ω_0 (generally $\gamma \ll \omega_0$, i.e. the system is under-damped), the amplitude of response $x(\omega)$ is significantly increased to the highest level, this phenomenon is called resonance. Figure 1.4 shows the diagram of resonance phenomenon of a harmonic oscillator. The damping rate γ increases the speed of the oscillator dissipates energy to the surroundings and determines the width of $x(\omega)$.

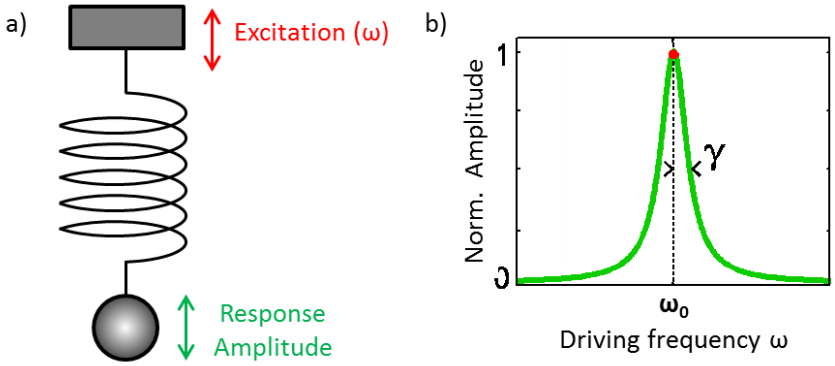

Figure 1.4: Resonance phenomenon of a harmonic oscillator. (a) Harmonic oscillator system where the periodical excitation force is at frequency ω. (b) The response amplitude according to the driving frequency, the maximum amplitude is observed when the driving frequency ω reaches the system vibrational frequency ω_0. Images adapted from [59].

1.2.2 Vibrational modes of molecules

From the simple mechanical model, we have described the fundamentals of resonance. In light-matter interaction, the driving force is the force exerted by the electric field on a molecule, ω is the frequency of the oscillating electric field, and ω_0 is the Eigen-frequency of a molecular vibrational mode. Thus the resonance phenomenon happens when the excitation frequency is close to the intrinsic vibrational frequency of the molecules.

Molecular diatomic vibration $(3N-5)$

Molecular diatomic vibration is a simple vibrational mode that can be considered very similar to the harmonic oscillator model. Considering two atoms as two material points, the van der Waals force induce the atomic attraction between them while the Pauli exclusion principle acts as a repulsive force that prevents interpenetration of the electron clouds [42]. These two forces compensate each other and act as a "spring" between the two atoms. Then the diatomic vibrational mode can be described by the simple harmonic oscillator with the intrinsic resonance frequency Ω_R. A molecule of linear geometry has $3N-5$ vibrational modes, where N is the number of constituting atoms, thus there is only 1 vibrational mode in this simple system of diatomic vibration with 2 atoms.

Molecular vibrational modes $(3N-6)$

However, most molecules do not have only two atoms but many atoms organized in space, thus, generally a molecule has vibrational and rotational modes of many different frequencies. For a molecule constituted by N atoms with nonlinear geometry, there are $3N-6$ vibrational modes, for example, the water molecule (H_2O) has 3 modes of vibration as described in Fig. 1.5, each of these vibrational modes has its own energy, quantified by quantum mechanics. The atomic mass, number of connections, the molecular substituent, the geometry and symmetry of the molecule all affect the vibrational force constants, and in turn define the vibration energy. These energies correspond to wavelengths that lie in the infrared range and can be probed by absorption spectroscopy. The rotational modes involve energies ranging from approximately 10 to 400 cm^{-1}, which corresponds to the far infrared region of the electromagnetic spectrum; while molecular vibrations have energies ranging from approximately 400 to 4000 cm^{-1}, which corresponds to the mid infrared region of the electromagnetic spectrum [40].

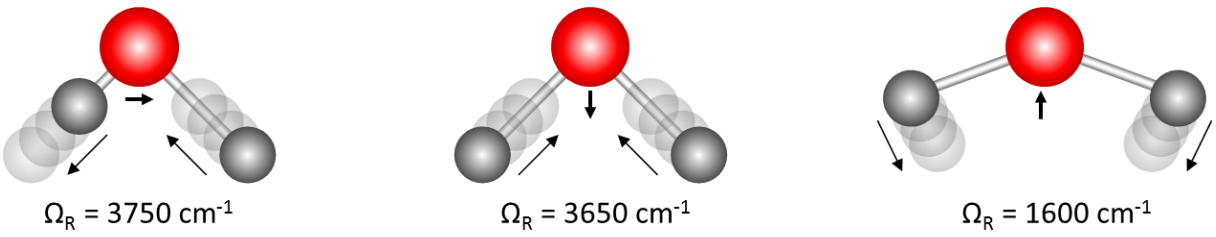

Figure 1.5: Vibration modes of H_2O molecule and their corresponding frequencies.

1.2.3 Linear and nonlinear susceptibilities

Nonlinear optics is the branch of optics that describes the behavior of light in nonlinear media, where the dielectric polarization responds nonlinearly to the electric field of the light. The linear and nonlinear susceptibilities are introduced in this subsection to give a fundamental macroscopic description of nonlinear process.

In any material, the elementary scatterer of light is an electron which is bound to a nucleus. The electric polarization vector P induced in a single electron-nucleus pair can be expanded as a power series in the incident electric field E [60]:

$$P = P(linear) + P(nonlinear) \tag{1.3}$$

with linear dipole moment

$$P(linear) = \epsilon_0 \chi^{(1)} E \tag{1.4}$$

and nonlinear dipole moment

$$P(nonlinear) = \epsilon_0 \chi^{(2)} EE + \epsilon_0 \chi^{(3)} EEE \tag{1.5}$$

where ϵ_0 is the permittivity of free space, $\chi^{(1)}$, $\chi^{(2)}$ and $\chi^{(3)}$ are first, second and third order susceptibilities respectively. Susceptibilities are related to atomic polarizabilities by a vectorial sum:

$$\chi^{(1)} = 1/\epsilon_0 \sum_{i=0}^{N} \alpha_i \tag{1.6}$$

$$\chi^{(2)} = 1/\epsilon_0 \sum_{i=0}^{N} \beta_i \tag{1.7}$$

$$\chi^{(3)} = 1/\epsilon_0 \sum_{i=0}^{N} \gamma_i \tag{1.8}$$

where N is the number density of dipoles in the scatterer, α, β and γ are first, second and third order polarizabilities of the electron-nucleus pair respectively.

1.2.4 Infrared (IR) absorption

As in the mechanical model illustrated in Fig. 1.4, the harmonic oscillator is analogous to the molecule which has certain natural vibrational frequencies; The driving force $F(t)$ is analogous to oscillating infrared radiation which exerts a force on the molecule. When the frequency of the driving force matches the frequency of the molecule, it absorbs energy and thereby increases its own vibrational energy by vibrating with increased amplitude, whereas at nonresonant frequencies the molecule is ineffective in absorbing energy. This is analogous to infrared absorption where the molecule absorbs radiation energy and goes to higher vibrational energy levels as showed in Fig. 1.6. In infrared spectroscopy, the molecule is irradiated with a whole range of infrared frequencies but is only capable of absorbing radiation energy at certain specific frequencies which match the natural vibrational frequencies of the molecule (see Fig. 1.6) [61].

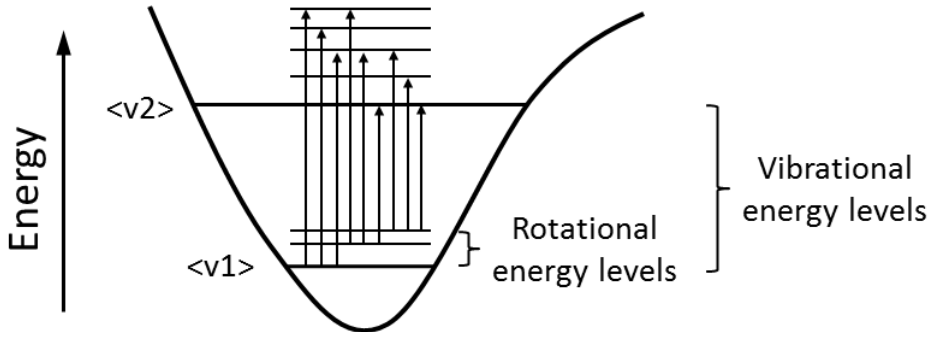

Figure 1.6: Infrared absorption.

While the absorption frequency depends on the molecular vibrational frequency, the absorption depends on how effectively the infrared photon energy can be transferred to the molecule. This depends on the change in the dipole moment between the levels involved in the transition which is the condition for the occurrence of infrared absorption [61]. Otherwise, the type of vibration is not infrared active, but it is active in Raman effect.

The infrared absorption intensity depends linearly on the first-order susceptibility [62]:

$$I_{\mathrm{IR}} \propto \mathrm{Im}\left[\chi^{(1)}\right] \tag{1.9}$$

which represents the linear optical process of infrared absorption.

1.2.5 Spontaneous Raman scattering

Different from infrared absorption, the Raman effect is a scattering process. When a molecule scatters light, most of the photons are scattered elastically, in other words, the energy of the scattered photons is the same as the incident photons (Rayleigh scattering). However, a small fraction of the light is inelastically scattered with a different optical frequency from the incident photons, this process of energy exchange between the molecule and the incident light is called "Raman effect". It was observed experimentally for the first time in 1928 by Raman and Krishnan [63] in India, and independently by Landsherg and Mandelstam [64] in the USSR. By focusing optically filtered sunlight in different liquids, they found that the scattered light has new wavelengths.

Consider our harmonic oscillator, instead of one driving force $F(t)$, we can drive the model with two forces $F1(t) = F_0 \cos(\omega 1 \cdot t)$ and $F2(t) = F_0 \cos(\omega 2 \cdot t)$, then the spring will be driven at the frequency of $(\omega 1 \pm \omega 2)$. In the Raman process, the excitation and the emission can be considered as the two driving forces with different frequencies ($\omega 1$ and $\omega 2$), the resonance happens when the frequency difference is equal to the natural vibrational frequency of the molecule. The energy level diagrams of the Raman scattering process is shown in Fig. 1.7. When a beam of light illuminates a material sample which can be solid, liquid or gas, the scattered light, which is observed spectroscopically, is found to contain new frequencies different from those of the excitation source (ω_P). Those new components shifted to lower frequencies $\omega_S = \omega_P - \Omega_R$ (red-shifted) are called Stokes Raman scattering (Fig. 1.7a), where the molecule moves from its ground state $|g\rangle$ to a new vibrational state $|v\rangle$ by taking the energy from the incident photon; whereas those shifted to higher frequencies $\omega_{AS} = \omega_P + \Omega_R$ (blue-shifted) are called anti-Stokes Raman scattering (Fig. 1.7b), the molecule changes from its vibrational state $|v\rangle$ to the ground state $|g\rangle$ by giving energy to a photon [40]. Experimentally, it appears that the amplitude of the anti-Stokes signal is lower than the amplitude of the Stokes signal (see Fig. 1.8). This is due to the fact that, in the thermal equilibrium, the ground level $|g\rangle$ is more populated than the vibrational level $|v\rangle$ according to Boltzmann distribution. Only modes with energy less than $k_B T$ where k_B is Boltzmann constant and T is temperature are significantly populated, in the general condition at room temperature ($\sim 25°C$), $k_B T \approx 200$ cm^{-1}. Thus, there is higher possibility for the occurrence of Stokes Raman scattering, which is also the reason that, in the spontaneous Raman spectroscopy, the Stokes scattering is

observed other than anti-Stokes scattering.

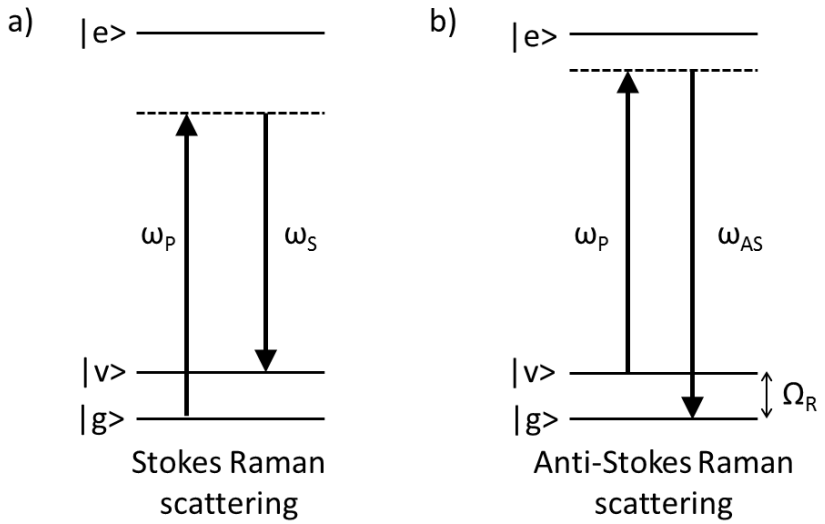

Figure 1.7: The mechanism of spontaneous Raman scattering. (a) Stokes Raman scattering. (b) Anti-Stokes Raman scattering. $|g\rangle$ is the vibrational ground state in the electronic ground state, $|v\rangle$ is a vibrationally excited state in the electronic ground state, $|e\rangle$ is the electronic excited state, the dashed line represents a virtual level.

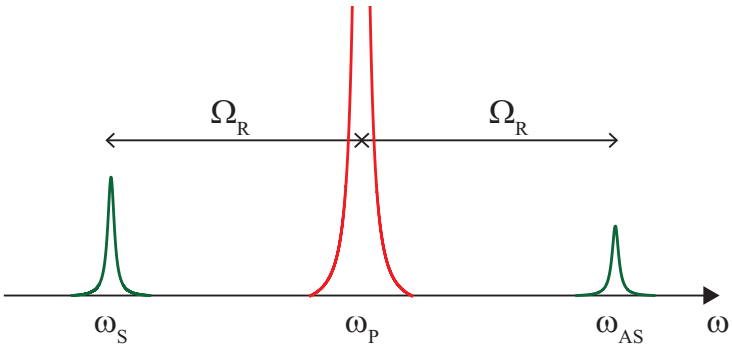

Figure 1.8: Illustration of a Raman spectrum for a molecule with only one mode of vibration frequency Ω_R. The anti-Stokes emission has lower intensity than the Stokes emission.

The dependence of spontaneous Raman signal intensity on the third-order nonlinear susceptibility is given by [62]:

$$I_{\text{Raman}} \propto \text{Im}\left[\chi_R^{(3)}\right] \tag{1.10}$$

where Raman scattering I_{Raman} relates only to the imaginary part of the third-order nonlinear susceptibility $\chi_R^{(3)}$ with a linear dependence, and it is only sensitive to the resonant part of the material response which results in the high signal-to-noise ratio in spontaneous Raman spectroscopy.

Therefore, in spontaneous Raman spectroscopy, most of the vibrational signatures can be explored in the spectra by exciting the molecules with visible light. It is powerful for its high chemical specificity and sensitivity, and plays an important role in biological applications. Spontaneous Raman spectroscopy has been used to identify the protein and lipid in various of organs such as liver, heart, kidney and skin [65]. The good spectral resolution supports the spontaneous Raman spectral mapping which was applied on brain cancer identification with further signal analysis [66]. Besides, Spontaneous Raman spectroscopy has been applied for various biological and chemical applications (including in our work) instead of IR spectroscopy, an important reason is that there is huge IR absorption in water, thus any water diluted molecules cannot be measured by IR spectroscopy but only spontaneous Raman spectroscopy. However, the distinction of Raman scattering is particularly dramatic for centrosymmetric structures (such as alkali halides), where all modes that change sign under inversion symmetry can be shown to be Raman-inactive [60].

Spontaneous Raman scattering is not usually suitable for imaging purposes because it is typically a rather weak process which requires detection times of the order of seconds to minutes per pixel [39, 67]. In the following sections, other two vibrational contrasts (CARS and SRS) are introduced to this work for fast and high-resolution imaging.

1.3 CARS microscopy

CARS is the nonlinear optical analogue of spontaneous Raman scattering but it addresses a single molecular vibration frequency by using a second laser. It was observed experimentally for the first time by Maker and Terhune in 1965 [68]. The most important difference between the Raman and the CARS processes is that: in CARS process, we target only one mode (or one frequency) at a time, so all the excitation energy will generate signal

pertaining only from that mode, whereas in Raman process, the excitation energy can generate signal from all the modes at the same time.

1.3.1 CARS process

CARS is a four-wave mixing process where a pump photon of frequency ω_P and a Stokes photon of frequency ω_S create a vibrational coherence in the molecule, it is then probed by another pump photon ω_P to induce the anti-Stokes signal ω_{AS} at the frequency of $\omega_{AS} = 2\omega_P - \omega_S$ (see Fig. 1.9a). The anti-Stokes field (CARS signal) is resonantly enhanced when the frequency difference $\omega_P - \omega_S$ coincides with the molecular vibrational resonance Ω_R. By acquiring the CARS signal as function of $\omega_P - \omega_S$ while tuning ω_P or ω_S, the unique vibrational spectrum of a molecule can be obtained. Or $\omega_P - \omega_S$ can be held fixed so as to generate CARS signal only from a specific vibrational resonance of the molecule of interest, in this case, the signal can be used for high-speed imaging.

However, in 1972, Levenson *et al.* [69] observed that when $\omega_P - \omega_S$ did not equal to a resonant vibrational frequencies ($\Omega \neq \Omega_R$), there was still anti-Stokes generation of a signal at ω_{AS} which is called CARS non-resonant process. This process happens through a different four-wave mixing process, which is not related with the vibrational mode, but generates signal at the same frequency as CARS resonant process (see Fig. 1.9b).

The resonant and non-resonant processes happen simultaneously during the CARS process, therefore, in CARS spectroscopy and microscopy, the intensity differences are not only based on chemical selectivity but also contain interferences between these two contributions.

1.3.2 Resonant CARS: resonant and non-resonant contributions

In CARS process, by tuning the frequency of pump or Stokes beam, different vibrational frequency can be achieved. When the frequency difference of the two beams is equal to the target molecular resonance ($\omega_P - \omega_S = \Omega_R$), it is called "resonant CARS" in this work. As it is discussed before, in resonant CARS, both resonant and non-resonant processes contribute to the total measured intensity at the anti-Stokes frequency. Thus

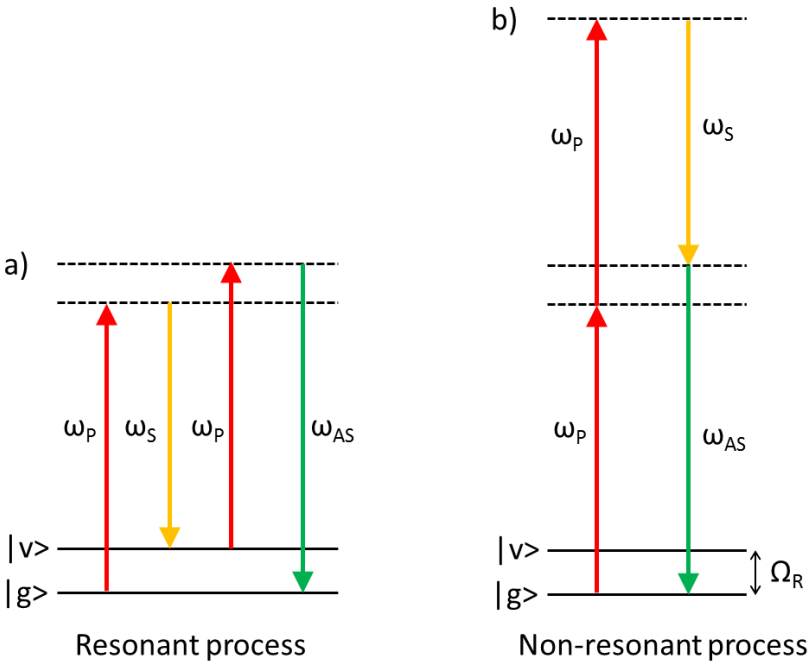

Figure 1.9: Diagrams of CARS resonant and non-resonant process. (a) CARS resonant process. (b) CARS non-resonant process. The dotted lines correspond to virtual states while the solid lines correspond to real states.

the susceptibility of resonant CARS can be written as:

$$\chi^{(3)} = \chi_R^{(3)} + \chi_{NR}^{(3)} \tag{1.11}$$

Since the total CARS signal is proportional to the square modulus of the nonlinear susceptibility [40], the intensity of the resonant CARS signal can be written as:

$$\begin{aligned} I_{\mathrm{R}} &\propto \left|\chi_R^{(3)} + \chi_{NR}^{(3)}\right|^2 \\ &\propto \left|\chi_R^{(3)}\right|^2 + \left|\chi_{NR}^{(3)}\right|^2 + 2\mathrm{Re}\left[\chi_R^{(3)}\right] \cdot \chi_{NR}^{(3)} \end{aligned} \tag{1.12}$$

The resonant CARS intensity I_{R} is presented by the sum of three terms described respectively in Eq. 1.12:

- $\left|\chi_R^{(3)}\right|^2$ is the "resonant" term which contains all the spectral information about the vibrational mode studied, it is the component of interest in spectroscopy and related with the Raman spectrum of Eq. 1.10;
- $\left|\chi_{NR}^{(3)}\right|^2$ is the "non-resonant" term which is spectrally constant because the non-resonant energy pathway goes through only virtual states. Virtual states exist as long as the fields that create them, they can be considered as impulsive responses, which can be thought as a model of harmonic oscillator with $\gamma = \infty$.
- $2\mathrm{Re}\left[\chi_R^{(3)}\right] \cdot \chi_{NR}^{(3)}$ is the "heterodyne" term which is proportional to the real part of $\chi_R^{(3)}$. It has a spectral dependency and it displays an asymmetric "dispersive" line shape at each vibrational frequency. It is the term responsible for the asymmetric appearance of peaks in CARS spectra [40].

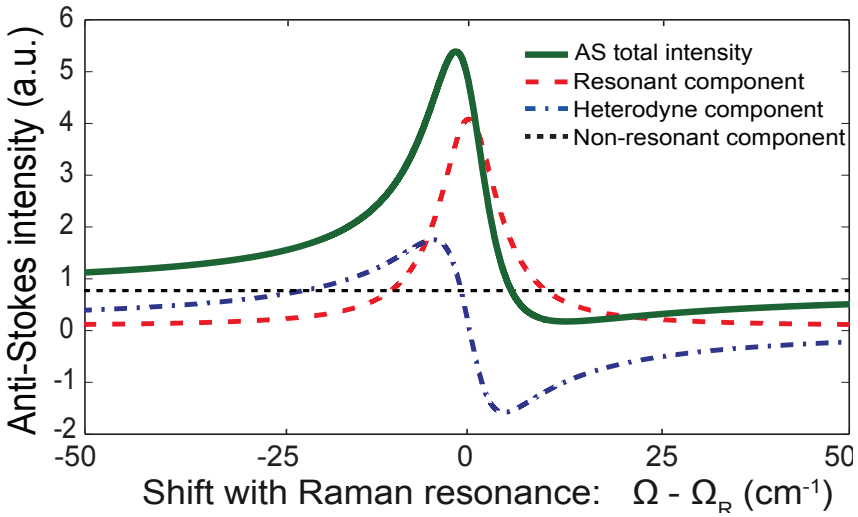

Figure 1.10: Theoretical total intensity of anti-Stokes (AS) signal spectrum and the intensity contributions of resonant, non-resonant and heterodyne.

The anti-Stokes spectrum can be considered as the interference between the "resonant" component and the other two components. We present in Fig. 1.10 the spectral behavior of these three components and the resulting anti-Stokes intensity. The resonant component represents the same vibrational signature as Raman spectrum (note that in CARS it is $\left|\chi_R^{(3)}\right|^2$ while in Raman it is $\mathrm{Im}\left[\chi_R^{(3)}\right]$); The non-resonant component is not affected by the vibrational mode and stay constantly as a function of frequency, which causes

the intensity shift and reduce signal-to-noise ratio; More complicatedly, the spectrum is distorted compared to the Raman spectrum by the heterodyne term, the maximum intensity of anti-Stokes signal is spectrally shifted towards blue and a trough appears on the right side of the peak. The final interfered CARS spectrum (AS total intensity) is not symmetric, and the resonance peak Ω is not exactly the same as Raman vibrational signature Ω_R.

Despite the presence of the non-resonant signal, the CARS process is still a powerful spectroscopic tool. Indeed, most of the time, this technique provides the same information as Raman spectroscopy (unless the non-resonant contribution is overwhelming). Besides, its cubic dependence with input intensity generates a relatively stronger process than Raman scattering, which makes the possibility of microscopic application, the detecting time can be significantly shorter to few milliseconds per pixel. Additionally, the good spatial resolution of CARS process also allows three dimensional optical sectioning. The CARS microscopy has an important position for chemical and medical applications [70], it has been combined with TPEF microscopy to observe the drug delivery in biological tissue in 3D in real-time [29].

1.3.3 Non-resonant CARS: quantitative study

In contrary to "resonant CARS", when it is off resonance ($\omega_P - \omega_S \neq \Omega_R$), only non-resonant component contributes to the total anti-Stokes signal. In CARS process, the non-resonant component is considered as a background in most of the studies when one is interested only in the spectroscopic information. There are various techniques available to reduce the non-resonance background including phase based, amplitude base, time based and polarization based methods [71].

However, the complex biological tissue is generally not a homogeneous environment. The background, which interferes with the vibrational contrast stems, is not only from CARS non-resonant contribution but can also be from the CARS signal of the other molecules or even from intrinsic fluorescence. In addition, when imaging thick biological tissue in depth, the signal-to-noise ratio is severely decreased by scattering of the excitation laser and the emitted signal, which is difficult to be quantified

Conversely, the non-resonant contribution can be harnessed for quantitative studies since it has constant spectral intensity [72]. We have discussed the resonant and non-resonant contributions in resonant CARS (see Eq. 1.12), while moving to non-resonance CARS, $\chi_R^{(3)}$ is negligible in the equation but only $\chi_{NR}^{(3)}$ contributes to the total CARS intensity:

$$I_{\mathrm{NR}} \propto |\chi_{NR}^{(3)}|^2 \tag{1.13}$$

where I_{NR} is neither affected by the density of target molecules nor the wavelength tuning of input lasers.

Therefore, non-resonant CARS can be used to estimate the total background in the vibrational contrast when studying a specific molecule, which is suitable for the biological tissue with complex background. More importantly, non-resonant CARS can also be used to take into account the loss of intensity of the excitation beams (pump and Stokes) upon penetration in absorptive and scattering tissue. If scattering and absorption was absent, the CARS non-resonant signal should be constant with increasing depth, but this is not the case in practice. We will show in this work that non-resonant CARS are used to correct for this loss of CARS efficiency upon penetration in tissue (detailed discussion in Chapter 2).

1.4 SRS microscopy

Stimulated Raman scattering (SRS) addresses the same vibrational signature as spontaneous Raman and CARS. Besides, it is superior for its background-free nature and linear dependence on molecular density. SRS was discovered accidently in 1962 by Woodbury and Ng [73], while they introduced a nitrobenzene Kerr cell inside a ruby laser cavity, an intense infrared radiation from the Kerr cell was detected. The source of this radiation was not determined immediately, until it was experimentally observed and confirmed as stimulated Raman process months later by Eckhardt *et al.* [74].

1.4.1 SRS process

SRS is another coherent Raman scattering process to achieve a vibrational signature. The excitation process is similar to resonant CARS [75]: 2 excitation frequencies, pump (ω_P) and Stokes (ω_S) are required and coincide on the target molecule, when the frequency difference between the 2 excitation beams ($\omega_P - \omega_S$) matches the molecular vibrational resonance Ω_R, the molecular transition rate is enhanced due to the stimulated excitation: the population is transferred from the ground state to the vibrational state through a virtual state (Fig. 1.11). This energy transfer process is very similar to Stokes Raman scattering, but in SRS process, instead of spontaneous transfer, the molecule is stimulated transfer to the vibrational state, which leads to much stronger scattering [76]. Besides, unlike CARS, the SRS process overcomes the non-resonant background, which brings higher sensitivity and gets rid of the vibrational peak shift.

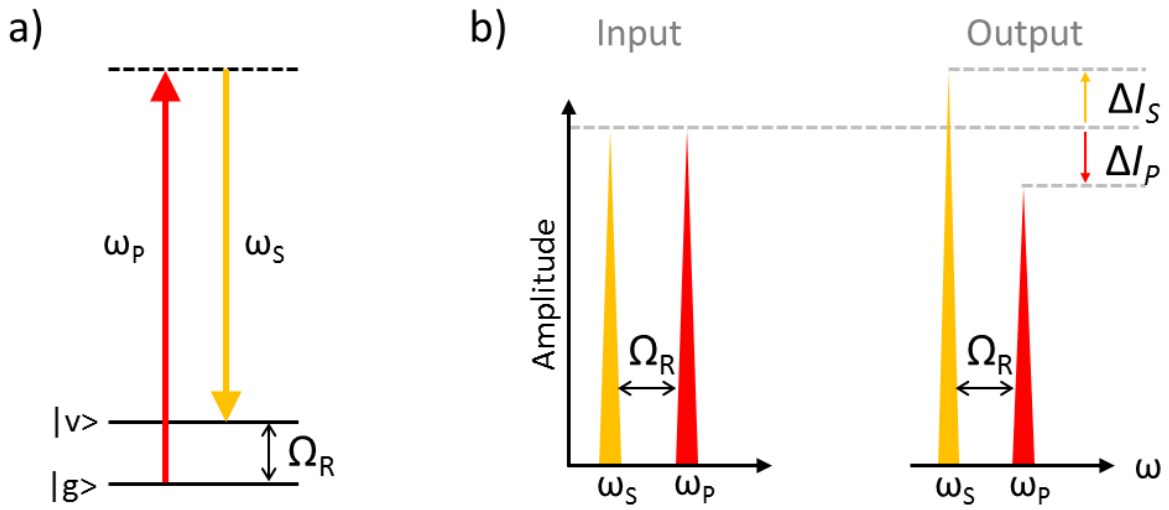

Figure 1.11: Stimulated Raman scattering process, the frequency difference between pump (ω_P) and Stokes (ω_S) is equal to the vibrational resonance of target molecule Ω_R. (a) Molecular energy transfer. (b) The amplitude of pump beam is reduced while the amplitude of the Stokes beam is increased.

As a result of the coherent excitation of molecular vibration, the pump photons are absorbed by the molecule and the Stokes photons are generated, which results in stimulated Raman loss (SRL, ΔI_P) or stimulated Raman gain (SRG, ΔI_S), of the intensity of the transmitted pump (I_P) or Stokes (I_S) beams respectively (Fig. 1.11b). This intensity

shift (ΔI_P or ΔI_S) is determined by [75, 76]:

$$\Delta I_p \propto -N \cdot \sigma_{Raman} \cdot I_P \cdot I_S \tag{1.14}$$

$$\Delta I_S \propto N \cdot \sigma_{Raman} \cdot I_P \cdot I_S \tag{1.15}$$

where N is the number of molecules in the probe volume, σ_{Raman} is the molecular Raman scattering cross-section.

Therefore, there is a nonlinear dependence of SRS signal on the excitation intensities (overall quadratic), it allows for intrinsic optical sectioning similar to TPEF and CARS microscopy, and is useful for three dimensional imaging of thick biological tissue. Besides, unlike CARS, the SRS intensity is proportional to the number of molecules in the probe volume (molecular concentration), which is an advantage for quantitative studies in chemical and biological applications.

1.4.2 SRS spectroscopy and microscopy

This technique was then applied to spectroscopy and microscopy applications. SRS spectroscopy was first developed with a femtosecond laser. Comparing with spontaneous Raman spectroscopy, SRS spectroscopy is more sensible, avoiding parasite fluorescence and giving better spectral and temporal resolution [77]. Furthermore, Freudiger *et al.* [23], Nandakumar *et al.* [24] and Ozeki *et al.* [78] have proposed the SRS microsocpy based on the use of a picosecond pulsed laser system at high repetition rate (80 MHz), which is adapted for biological imaging by its low average energy of pulsed laser and for fast scanning technique by high repetition rate.

SRS microscopy is the same as CARS microscopy in what concerns the excitation conditions, but different in detection system. For CARS microscopy, the useful signal (anti-Stokes) is generated at a different frequency from the excitation beams, which can be separated by bandpass filters and detected by highly sensitive detectors, such as avalanche photodiodes (APD) or photomultiplier tubes (PMT). However, for SRS microscopy, the detection is different since the useful signal is generated at the same frequencies as the exciting beams, the useful signal ought to be detected is the energy loss of the pump

beam ΔI_P or the energy gain of the Stokes beam ΔI_S. In practice, the energy loss or gain (ΔI_P, ΔI_S) is $\sim 10^5 - 10^8$ times weaker compared to the pump or the Stokes beams (I_P,I_S), which causes difficulties for the detection. To retrieve these components, it has been proposed to modulate one of the beams at a frequency f, and then to extract the SRL or SRG signal at this frequency by synchronizing the detection at frequency of f as well (SRG is showed as an example of detection in Fig. 1.12). To reduce electronic noise and laser noise, it is essential to choose a modulation frequency higher than 1 MHz [23, 78].

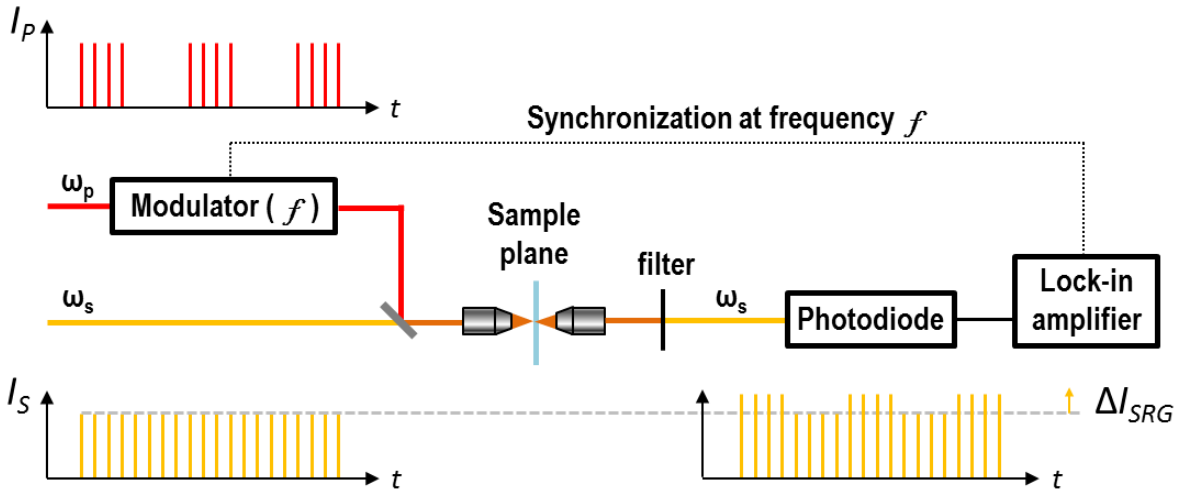

Figure 1.12: Experimental implementation of SRS detection (for the case of SRG). The pump beam is modulated at a high frequency ($f > 1$ MHz). At Raman resonance ($\omega_P - \omega_S = \Omega_R$), the Stokes intensity is enhanced only when the pump laser is on. The small energy gain of the Stokes beam is measured by a synchronized detection at the same frequency f.

In conclusion, stimulated Raman spectroscopy and microscopy is powerful for its chemical sensitivity, background-free ability and linear dependence on molecular concentration. These properties are helpful in solving various chemical and biological problems [28, 79], especially in quantitative studies [80]. Moreover, recent advances in SRS microscopy effort to apply SRS imaging technique for *in vivo* applications [81, 82].

1.5 Experimental condition

Experimental conditions, including the environment, the excitation lasers, the detectors and even the assistant equipments (such as the sample holder), all influence the final results of experiments. In this work, experiments were performed on a custom-built setup, which can be used for TPEF/CARS/SRS spectroscopy and microscopy, as well as the hyperspectral imaging. Both *ex vivo* and *in vivo* experiments can be performed on this system by slight modification.

Figure 1.13 shows a schematic of the custom-built setup. It comprises as light source two optical parametric oscillators (OPO1 and OPO2, Emerald, APE) synchronously pumped by a mode-lock frequency doubled Nd:YVO Laser (PicoTrain, HighQLaser) operating at 532 nm. The two beams from OPO1 (pump) and OPO2 (Stokes) (pulse duration 5 ps, repetion rate 76 MHz) are overlapped in time and space and sent into a customized scanning microscope [36]. Excitation and Epi collection is provided by an NA=1.15 objective lens (Nikon APO LWD water 40 $\times$) whereas FWD collection uses an NA=0.6 lens (Olympus UCPlan FL 40 $\times$). TPEF and CARS signals are detected both in the forward and backward directions by means of two PMTs (Hamamatsu, H10682) working in the photon-counting regime. For SRS, the pump beam is modulated at 1.5 MHz by an acousto-optic modulator (AA Optoelectronic MT200-AO) and the SRG signal is detected in the forward direction (FWD) with a high speed photo-diode (ThorLabs PDA10CS) and a fast lock-in amplifier (Zurich Instruments, HF2LI).

Incident powers available in this work, at the sample plane, were $<$ 30 mW for the pump beam and $<$ 40 mW for the Stokes beam depending on the samples (for skin sample, less power can be applied for *in vivo* than *in vitro*). TPEF and CARS/SRS imaging are performed at the same time. Typical CARS/TPEF images acquired throughout this work are 250 $\times$ 250 pixels, dwell time: 40 μs/pixel, total time for scanning an image is 2.5 s.

Figure 1.14 shows the wavelength ranges of excitation lasers and emission signals. The vibrational imaging is based on the frequency difference between pump and Stokes beams, in principle the absolute wavelengths can be chosen independently. In practice, the excitation wavelengths are chosen approximate within the "optical window" of biology tissue (near IR - IR), where both absorption and scattering are minimized and optical penetration depth is therefore maximized [76]. The pump laser OPO1 operates at the

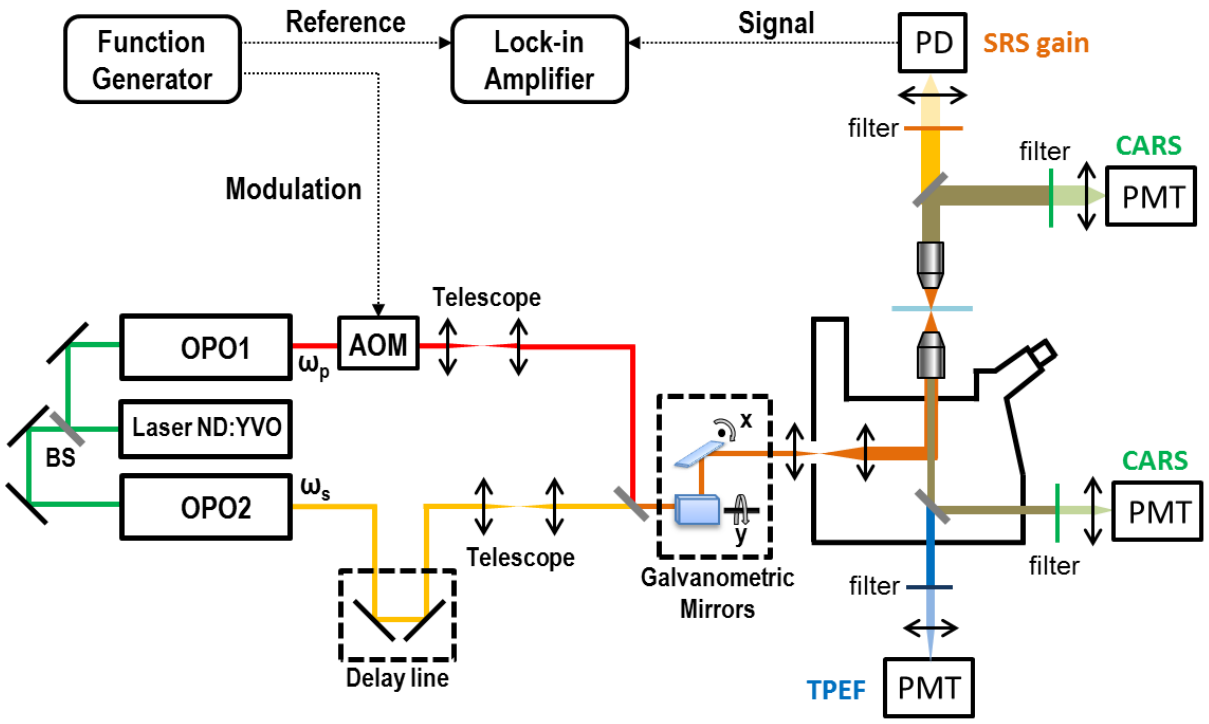

Figure 1.13: Nonlinear microscope setup and frequency chart for pump, Stokes and CARS signal. OPO: optical parametric oscillator, AOM: acousto optics modulator, PMT: photomultiplier tube, PD: photodiode, BS: beamsplitter.

fixed wavelength of 735 nm and modulated at 1.5 MHz whereas Stokes laser OPO2 can be tuned between 760 nm and 950 nm to cover a wavenumber range of [500 cm^{-1} - 3000 cm^{-1}], the anti-Stokes signal is generated in a range of [600 nm - 710 nm]. In the mean time, two-photon fluorescence is mostly excited by the pump laser and it is emitted within a broad range from 400 nm to 600 nm. SRS gain signal is obtained at the same wavelength as Stokes beam.

Notice that the FWD detections (FWD-CARS/SRS) in Fig. 1.13 are only available for *in vitro* experiments while the emitted signal can pass through biological sample. When it moves to *in vivo* imaging, the setup is then slightly modified (see Fig. 1.15): The back reflected TPEF and CARS signals are obtained, special home-designed holders for arm and hand are necessary to fix the sample during experiment (detailed imaging process *in vivo* see Chapter 3).

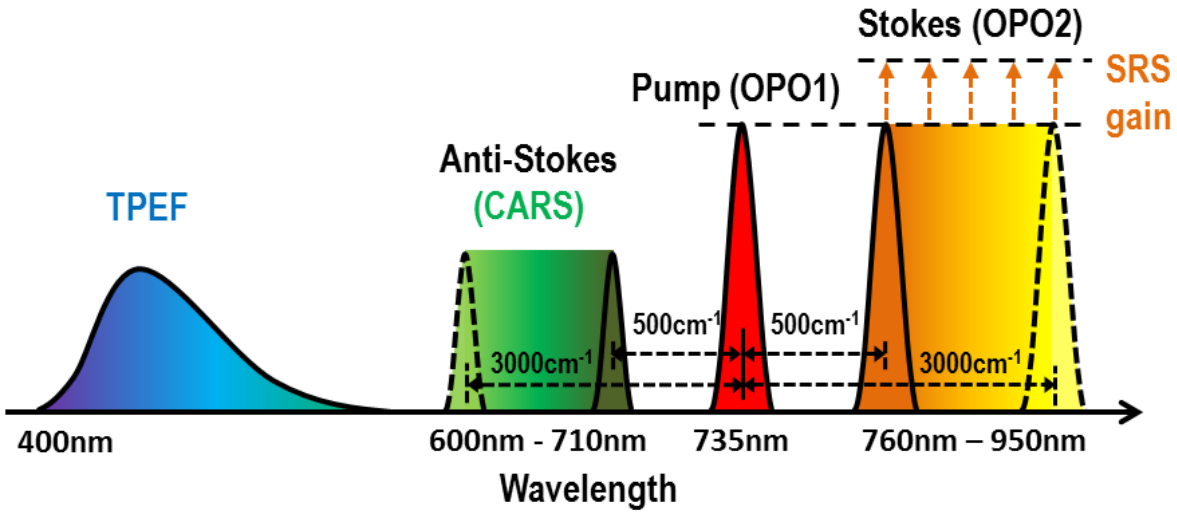

Figure 1.14: Spectra of excitation lasers and emission signals. Pump (OPO1), fixed at 735 nm, and Stokes (OPO2), tuned between 760nm - 950 nm, are excitation lasers; TPEF, CARS and SRS signals are generated at different wavelengths.

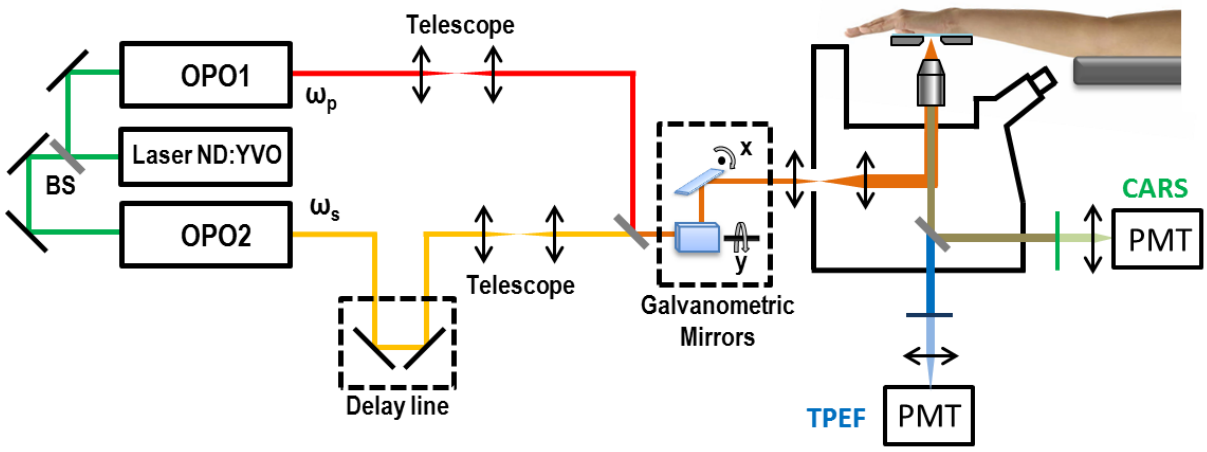

Figure 1.15: Nonlinear microscope setup adapted for *in vivo* imaging.

Chapter 2

Absorption of molecules in human skin in 3D

Skin envelops the entire body, acts as a pivotal, efficient natural barrier towards various invaders. For the treatment of major dermatological diseases and in the cosmetic industry, topical applications on skin are widely used. Therefore, many efforts in skin research have been aimed at understanding detailed molecular absorption mechanisms occurring from topical application of pharmaceutical or cosmetics products. To date, most of the technique available for percutaneous penetration and absorption fail to provide a quantitative 3D map of molecular distribution of compounds in tissue. To approach this goal, we designed a framework for imaging and reconstructing molecular concentration within the depth of artificial and human skin samples. Pivotal to our results was the use of deuterated molecular compounds together with coherent anti-Stokes Raman scattering spectroscopy and microscopy that permits unambiguous discrimination of targeted molecules within skin layers. We demonstrated both intercellular and transcellular pathways for different active compounds, together with in-depth concentration that reflects the detailed skin barrier architecture. This method provides an enabling platform for establishing functional activity of topically applied products.

This chapter is organized as follows: the fundamentals of human skin is provided firstly; Secondly we describe an original method combining coherent anti-Stokes Raman scattering (CARS) microscopy and spectroscopy together with two-photon excited native

fluorescence (TPEF) imaging, to provide 3D quantitative skin active compounds mapping together with detailed skin morphological identification; Thirdly we analyse the penetration of three active compounds in both reconstructed and human skin; And finally, the quantification results are compared with another chemical where a great accordance are presented.

2.1 An introduction to skin

As an interface between human body and external environment, skin protects the organism and maintains body temperature from outside, and at the same time communicates with the environment. The remarkable ability of our skin to adapt to its surroundings is not only due to its surface topography but also due to its in depth organisation [3]. Fig. 2.1 shows a simple diagram of human skin and indicates the major structures that are normally found in each compartment.

In contrast to other epithelial tissues, skin is unique by its multi-layered architecture and the presence of a cornified epithelium. Predicting the penetration of a given active formulation in or through the skin remains very difficult due to this highly complex natures of the structures and mechanisms that constitute the delivery pathways. As shown in Fig. 2.1, three layers of skin can be recognized: epidermis, dermis and subcutaneous tissue. The epidermis is a superficial, stratified, rapidly replicating epithelium that can be readily repaired from any damage it may suffer from external contacts. The dermis is a thicker layer between the epidermis and subcutaneous tissue, that contains plenty of skin appendages, including hair follicles, eccrine sweat glands, sebaceous glands, apocrine glands, lymphatic vessels, blood vessels and nerves. Under the dermis, subcutaneous tissue is found to store fatty tissue and attach the skin to underlying muscle [84]. Interaction among these layers is important during skin development and for maintenance of homeostasis which is a regulation process that remains the stability of human body internal environment; but each can also be considered respectively in function, for instance, the waterproof ability of epidermis. Skin layers as well as their related functions are explored in detail in the following sections.

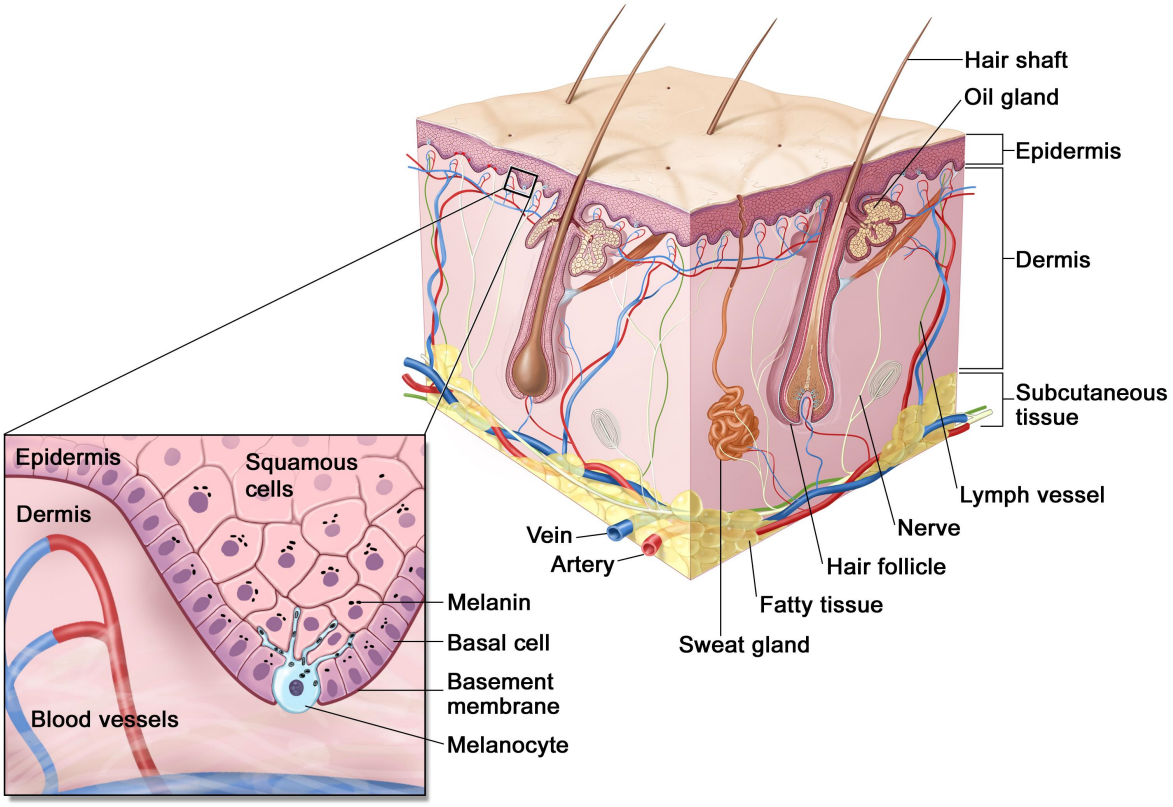

Figure 2.1: Diagram of human skin [83]. The thin superficial layer of skin is the epidermis whereas a thick layer deeper below is the dermis, subcutaneous tissue is attached on the dermis to connect skin with underlying muscles. The epidermal-dermal junction is shown in the magnified view where the basement membrane acts as an interface between them.

2.1.1 Epidermis

The epidermis is a stratified, continually renewing epithelium that exhibits progressive differentiation of keratinocytes (known as keratinization) from basal to superficial direction. Maintenance of cell number in the epidermis and the regulation of epidermal homeostasis depend upon a fine balance between cell birth (proliferation) and cell death (differentiation) of keratinocytes. During the lifetime of an individual keratinocyte, correlated with its position within the epidermis and its state of differentiation, the morphology and function can be extremely different. According to this genetically programmed and precisely regulated metabolic process, the epidermis can be basically organized as 4 layers (from

proliferation to differentiation): the basal layer (stratum basale), the spinous layer (stratum spinosum), the granular layer (stratum granulosum) and the cornified layer (stratum corneum) (see Fig. 2.2).

At first, a keratinocyte is an epidermal stem cell which resides in the lower part of the epidermis (stratum basale) and is attached to the basement membrane. Then with [84]:

- the loss of the ability to proliferate;
- an increase in cell size and cell flattening;
- the formation of new organelles together with structural reorganization of existing organelles, and eventual loss of organelles;
- the synthesis of new protein and lipids;
- the interaction with the immigrant cells (melanocytes, Langerhans cells, Merkel cells);
- the adhesion of keratinocytes to each other;
- the changes in plasma membrane properties, cell surface antigens and receptors;
- dehydration;

at the end-point of keratinization process, the keratinocyte is terminally differentiated to dead cell (the corneocyte), which contains keratin filaments and matrix protein, and a protein reinforced plasma membrane with surface-associated lipids. It is estimated in human that once a keratinocyte leaves the basal cell layer, its normal transit time to the stratum corneum is at least 14 days, and the total time of keratinocytes turnover from stem cells to desquamation is every $40 \sim 56$ days, this process continues through out all the life [85].

Figure 2.2 shows the general epidermal layers that are formed during the keratinization process as well as the major epidermal cell types contained in each layer.

The cornified layer (stratum corneum: SC), the outermost layer of the skin epidermis, consists of corneocytes embedded in a lipid-enriched extracellular matrix. The average

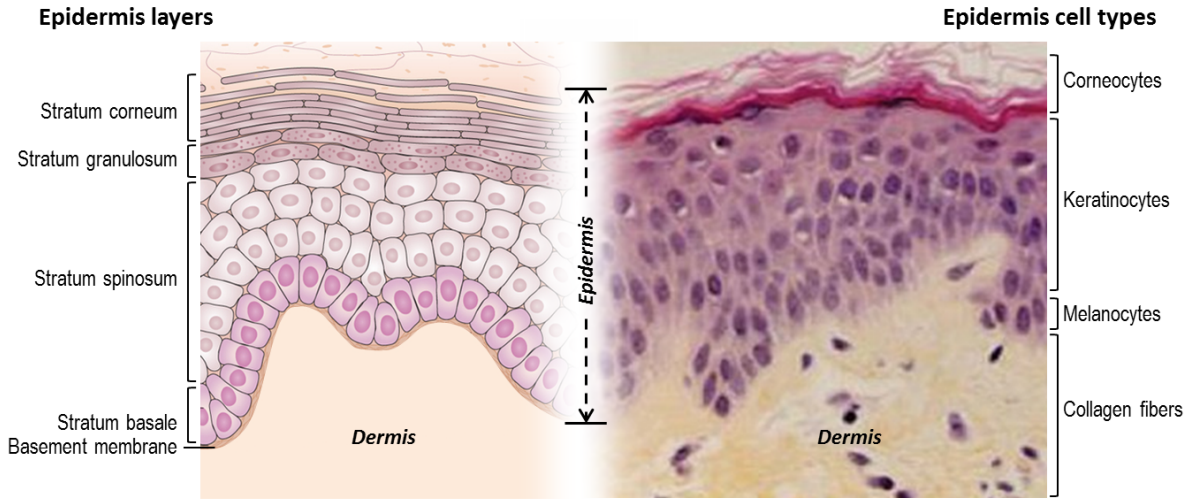

Figure 2.2: Normal human epidermis model and histological section stained with Hematoxylin-Eosin-saffron, where the epidermis layers as well as the major epidermal cell types contained in each layer are both indicated (images adapted from [86, 87]). The skin model (left) that is generally considered in skin research is established based on the real normal skin structure (right).

thickness of stratum corneum is $\sim 15\ \mu$m, but the local thickness and corneocyte cell layers are very different corresponding to the anatomical location, age, sex and physical parameters [88]. Although the corneocyte is non-viable it is still considered to be full functional, particularly in terms of the important barrier properties of the stratum corneum [84]. The SC is relatively waterproof and, when undamaged, prevents most bacteria, viruses, and other foreign substances from entering the body. It exhibits a low permeability that is related to highly organize intercellular lamellar lipids composed of ceramides, fatty acids and cholesterol. These properties of SC makes the topical molecular delivery through the SC barrier a challenge even for small molecules [4]; either drugs used for the treatment of dermatological disease or molecules used in cosmetic formulations to protect epidermis against environmental stress or degradation process involved in aging.

The granular layer (stratum granulosum: SG) consists of two or three layers of granular cells that can be recognized by their characteristic cytoplasmic basophilic keratohyalin granules, they are composed primarily of an electro-dense protein, profilaggrin and keratin intermediate filaments.

The spinous layer (stratum spinosum: SS) is so named because of the histological appearance of the resident keratinocytes. The abundance of focal junctions (desmosomes) between adjacent keratinocytes results in the formation of 'spines' due to shrinkage artifact during the process of keratinization.

The basal layer (stratum basale: SB) consists primarily of mitotically active keratinocytes and immigrant cells such as melanocytes, they are organized in a thin layer with corrugated shape. The stem cells located in the basal layer sustain the epidermal renewing process and the production of committed progenitors, they generate progeny that will undergo terminal differentiation leading to the development of a protective epidermal barrier. At the bottom of the basale layer, a thin basement membrane (BM) is tightly attached as a epidermal-dermal junction as shown in Fig. 2.1 [84].

2.1.2 Dermis and subcutaneous tissue

Under the epidermis, there is a 1 mm thick dermis, which is elastic and naturally contracted. The dermis is the major mechanical component in skin. Like all connective tissues, it is constituted of collagen fibers immersed in a viscous fluid, rich in glycoproteins. The two main functions of dermis are to maintain the spatial organization of underlying tissues and to resist to external mechanical stresses. Anatomically and histologically, two layers should be considered in dermis: the superficial or subpapillary dermis (about 50 - 200 μm thick) and the chorion or reticular dermis (about 1 mm thick).

The superficial or subpapillary dermis is a loose tissue that contains glycoproteins, thin elastic fiber and collagen bundles. Also, it is rich in blood, lymph vessels and nerves, the physiological variations, such as the volume of water or vascular content in the superficial dermis, can directly alter the mechanical behavior of the skin as a whole.

The chorion or reticular dermis, that remains below superficial dermis, is formed by thicker bundles of collagen (2 - 20 μm) close to one another and connected by large elastic fibers (0.1 - 0.4 μm), also fewer vessels and nerves can be found in this layer but they are bigger than in the superficial dermis [89]. These all make the chorion dermis a tight but flexible tissue.

The interface between dermis and the subcutaneous tissue is irregular and poorly defined. The mechanical properties of the subcutaneous tissue is a loose conjunctive tissue often loaded with fat. Functionally, it allows the skin to move as a whole on the underlying structures (muscles and tendons) and plays a major part in the absorption of external forces. In scars, where the subcutaneous tissue disappeared, the skin loses its mobility and sustains considerably higher stretching and friction constraints [56].

In Section 2.2.1, the epidermis and dermis are imaged by the two-photon excited fluorescence microscopy, where the epidermal and dermal layers can be distinguished and the specific cell types contained in each compartment can be observed.

2.1.3 Skin aging

Skin aging involves a complete and systemic change in the entire body. The effects of age are manifested in the appearance, structure and mechanics of skin (excessive dryness and flaccidness, deepening wrinkles and dyspigmentation) as well as age-related functions (decreased protection, increased predisposition and fragility, difficulty to heal injuries, alteration in skin permeability to drugs, and tumor incidence). Fig. 2.3 shows the detailed differences between young and aged skin focusing on epidermal alteration, notice that, over the years, although skin primary functions may gradually alter, the physiological wear from skin aging is a consequence of damage that accumulates throughout the whole life [90].

Skin aging is caused both by intrinsic and extrinsic factors. Intrinsic skin aging describes the irreversible genetic and physiological process that starts as soon as physical maturation is accomplished. It is characterized by the loss of cell number, substance and function. Extrinsic skin aging is mainly a consequence of cumulative UV exposure of the skin and also can be accelerated by tobacco abuse [92]. Extrinsic leads to basically similar changes than intrinsic skin aging, but also to specific alterations such as inducing elastosis cutis and pigment shifts. Moreover, extrinsic factors act to aggravate the course of intrinsic skin aging.

Numerous investigations aim at understanding the detailed process of skin aging, and most of them concern dermis. Multiphoton microscopy (TPEF and SHG) has been used

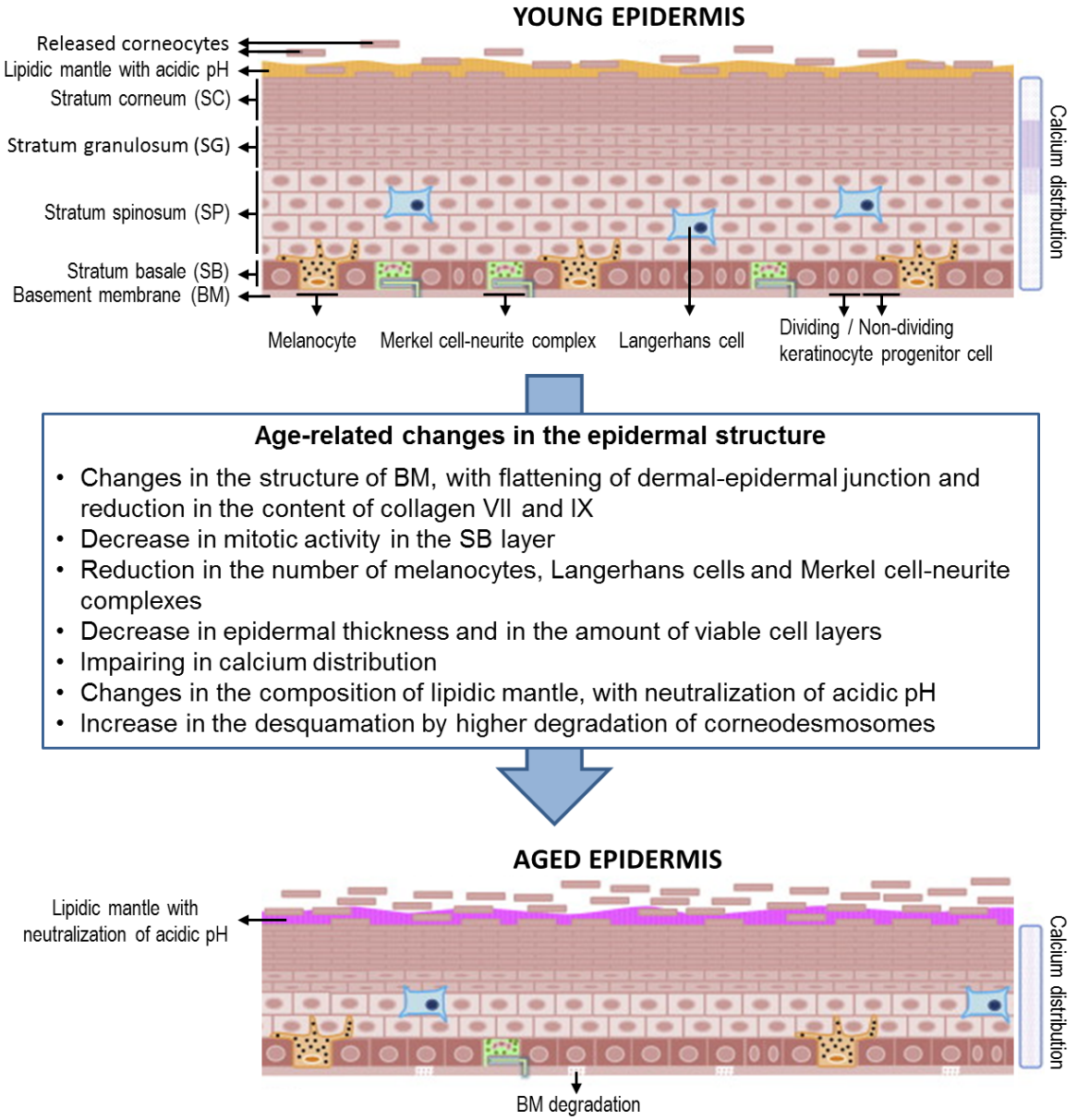

Figure 2.3: Structural and functional changes associated with epidermal aging (images adapted from [91]). As the epidermis ages, it undergoes a series of structural modifications that directly impact its physiological functions as described in this figure.

for *in vivo* studies of human skin aging at the dermal level, where an aging index has been proposed based on the content of collagen and elastin [93]. Nevertheless, to forward an additional step which is skin aging treatment and prevention, other studies have targeted

epidermal aging. Besides of health-related implications on skin, epidermal alterations can lead to obvious changes in skin appearance [94] which is always an interesting topic for cosmetic research and industry. So far, a great number of active ingredients are proposed and can be found in the market for different efficacy related with anti-aging, including maintenance of water-ion balance (i.e. glycerol, vitamin A and B3, jasmonic acid derivative LR2412) and protection from solar radiation (i.e. UV filters, cocoa powder, vitamin C and E) [91].

In the following subsection, the skin samples and cosmetic molecules used in this work are introduced. The differences between young and aged skin are observed by TPEF microscopy in Section 2.2.1, and the penetration in skin of cosmetic molecules are investigated, especially the anti-aging compound LR2412.

2.1.4 Skin samples preparation

In this work, to study and compare different active molecules penetration into skin from topical application, two types of skin samples have been considered: reconstructed skin model (D13 Episkin® by SkinEthic®) and excised human skin (Biopredic International). Moreover, three molecules: (1) a synthetic derivative of jasmonic acid LR2412, (2) glycerol and (3) water were dissolved in their vehicles solution with proper concentration and applied on the sample surface.

Skin samples

(1) Reconstructed skin (Episkin® by SkinEthic)

Episkin, an *in vitro* reconstructed human epidermis, is manufactured by L'Oreal. It is obtained by culturing adult human keratinocytes on a collagen substrate (collagen type I and III coated with a think layer of collagen IV) in conditions which permit their terminal differentiation and the reconstruction of an epidermis (see Fig. 2.4) [95]. The sample grows in a humidified incubator at 37°C with 5% CO_2 supplementation.

The Episkin is developed to replace animal and human test. This reconstructed skin model is histologically similar to the *in vivo* human epidermis. Therefore it has been used to study the delivery and effect of cosmetics or dermatology related molecules, especially

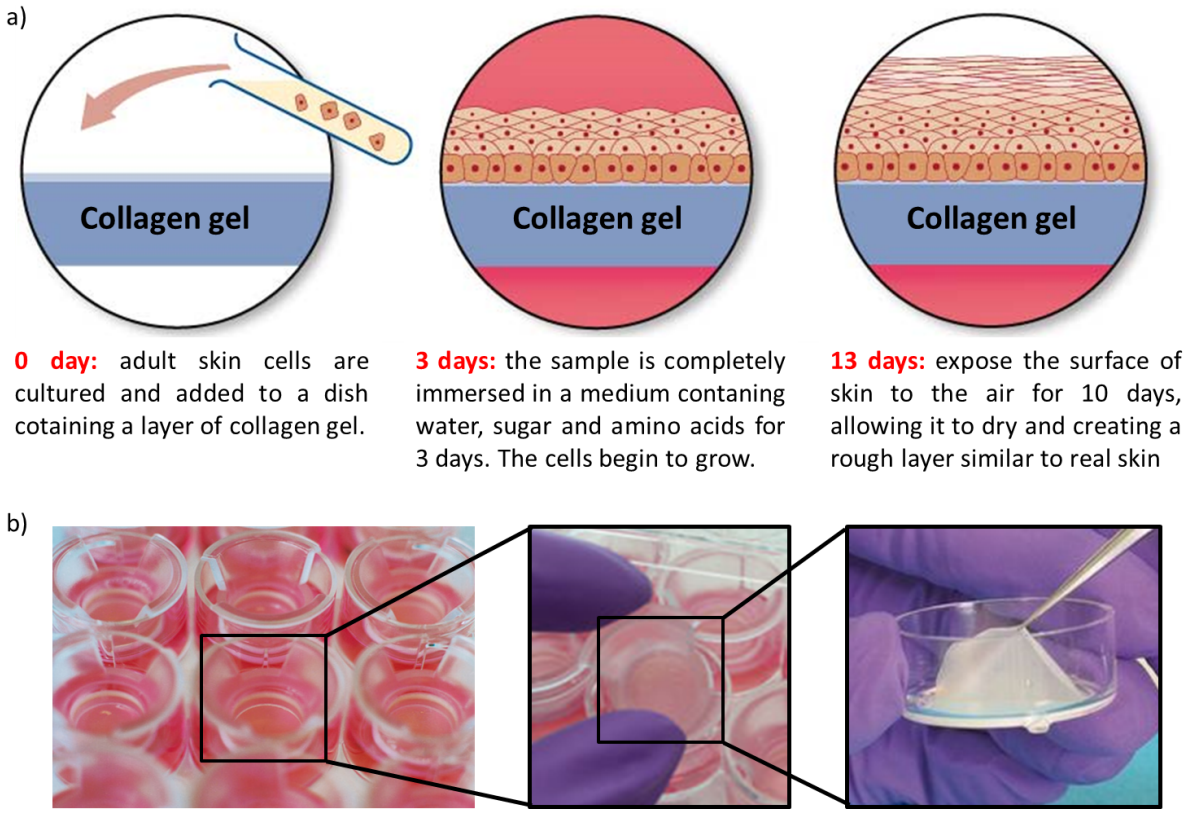

Figure 2.4: Episkin (images adapted from [95] and L'ORÉAL Research & Innovation). (a) The culturing process of Episkin (b) Views of Episkin samples (after 13 days) used in the experiment.

with topical application [87,96].

Currently the Episkin kit is marketed in the form of 12 well plates (disk diameter $\sim$ 1.2 cm) and used in laboratories and industry. We have considered in this work Episkin samples after 13 days of culture that exhibit a multi-stratified epidermis and a horny layer similar than human skin. Samples were kept in an incubator containing maintenance medium below the collagen gel layer and used at day fourteen (D14) and fifteen (D15) for the experiments. In the experiment, the target molecules are applied on the Episkin surface for 1h incubation time, before placing the sample on the microscope, the collagen layer has to be removed and the skin sample has to be flatten between two cover slides.

(2) Excised human skin (Biopredic International)

Excised human skin from abdominal plastic surgery were purchased from Biopredic International. The skin samples selected are free of moles and hairs and decontaminated before surgery with betadine or chlorhexidine alcohol, then subcutaneous fat has been removed after the surgery. Three batches of samples were used for this study, No.1 and No.2 (see Table 2.1) were stored at - 20°C right after the surgery and defrost just before the experiments. No.3 was fresh human skin sample which was readily available for experiments 6h after the surgery and was stored at 4°C meanwhile. Detailed information of excised skin samples used in this study are presented in Table 2.1. Excised human skin is one of the best sample that is extremely similar to human skin *in vivo*, however, depending on the situation of the patients, the skin samples can be different in color, thickness, cell organization or pigmentation distribution, moreover, the quantity of samples is quite limited due to the situation of donor, which does not allow all the experiments and comparisons done on the same sample.

Table 2.1: Excised human skin samples (Biopredic International)

Sample No.	No.1	No.2	No.3
Batch number	TRA002790-OC06	TRA002864-OC02-04	EXP004300B001
Sex	Female	Female	Female
Origin	Caucasian	Caucasian	Caucasian
Age	60yr	56yr	56yr
Surgery date	May 03, 2012	Dec 12, 2012	Apr 15, 2014
Production date	May 03, 2012	Dec 13, 2012	Apr 15, 2014
Diameter	30mm	40mm	30mm
Mean thickness	533μm	450μm	430μm
Storage temperature	-20°C	-20°C	4°C

Figure 2.5 presents a detailed view of excised human skin sample preparation (in the dedicated holder) prior and during nonlinear imaging. The skin sample is stretched and fixed on a piece of cork featuring a ∼4 cm opening (Fig. 2.5 b, top). The dermal part of the sample is always kept wet using a dedicated metal reservoir containing a PBS solution and sealed with a cover glass (Fig. 2.5 b, bottom). The sample is defrost just before the experiments, active molecules (LR2412, Glycerol, water) are applied on the skin surface for 4h and 24h prior nonlinear imaging and are kept sealed using a 25 mm diameter, 1 mm thick polymer spacer and a 25 mm diameter cover glass (Fig. 2.5 a). During incubation the sample preparation is kept in a close wet chamber (Fig. 2.5 a). For Nonlinear imaging

the polymer spacer is removed and replaced by a cover glass directly in contact with the skin surface. Note that a ∼50 μm active molecule liquid layer always remains between the skin surface and the cover glass (infinite dose scheme). The sample preparation is then flipped upside down and mounted on an inverted microscope. Refer to the techniques introduced in Chapter 1, native TPEF and CARS signal are collected in the backward direction whereas SRS (only for reconstructed skin samples) is collected in the forward direction (Fig. 2.5c, detailed information of optical system see Chapter 1).

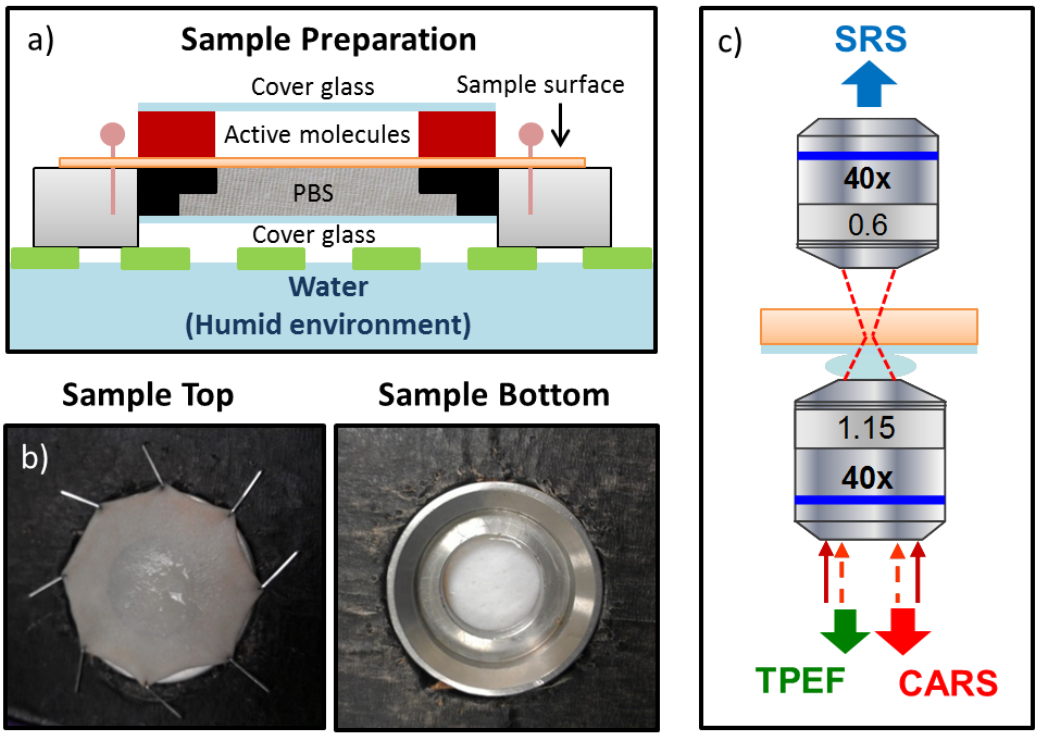

Figure 2.5: Skin sample preparation. (a) Sample preparation, (b) top view of an excised human skin sample with the spacer and cover glass removed; bottom view of the same sample, a cover glass is sealing the PBS reservoir, (c) sample preparation mounted in the nonlinear microscope for TPEF, CARS and SRS imaging.

Active molecules

As mentioned before, three active compounds were used in this work to study molecular penetration into skin from topical application, the molecules were all deuterated (the structural formula is presented in Fig. 2.6). Deuteration is a key point in our work because it provides a vibrational resonance around 2100 cm^{-1} (C-D case) in the clear

vibrational spectral window of skin. The choice of these active compounds has been motivated regarding their interest in cosmetics and for their different hydrophobicity.

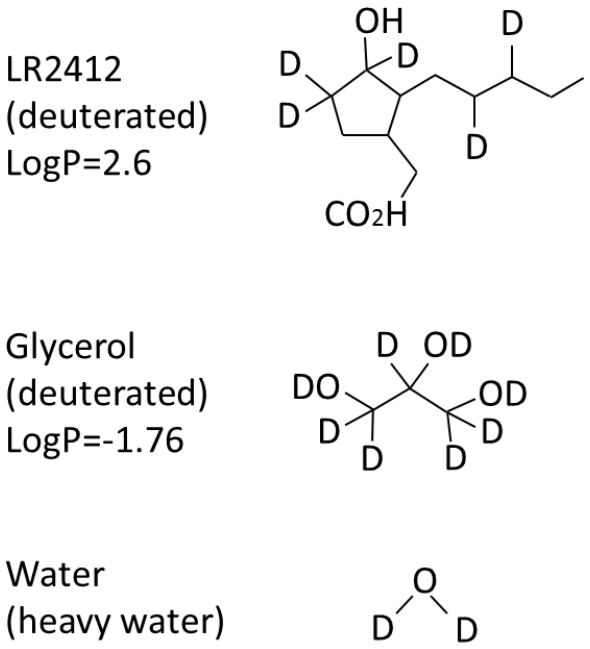

Figure 2.6: Deuterated compounds considered in this work and respective partition coefficient LogP.

(1) LR2412

Jasmonic acid (JA), a plant hormone acts as a naturally occurring growth regulator, was first found and isolated from the jasmine plant. Several distinct physiological effects have been noticed for this compound and related compounds in plant metabolism and defense responses [97, 98]. Afterwards, more biotic roles of JA were reported in different species of the plant kingdom: In soybean plants, many of the JA-responsive genes were found being in high level related with young organs and tissues including hypocotyl hooks, plumules, flowers, young leaves and developing fruits [99]; in tomato leaves, the role JA is the intra-cellular signaling response to injury, it accumulates for wound repairing and tissue regeneration during plant development [100]; additionally, the jasmonate family acts as signal transduction intermediate when plants are subjected to environmental stresses such as UV radiation, osmotic shock, cytotoxic drugs and heat [101].

JA properties in plant development stimulated research on cosmetic applications of JA derivatives. LR2412 is a synthetic derivative of jasmonic acid, developed and launched to correct signs of skin aging [102]. Clinical studies have demonstrated the effect of LR2412 [15] on several signs of aging. Nevertheless, an understanding of detailed penetration behavior of LR2412 and molecular cutaneous absorption in human skin is further required.

In this work, deuterated LR2412 (synthesized by l'Oréal laboratories according to standard preparation procedures) was dissolved in propylene glycol (PG) with a concentration of 50% (mass), the partition coefficient for LR2412 is LogP = 2.6 (relatively hydrophobic) [103]. The final dilution was applied on both Episkin and excited human skin sample to understand the detailed molecular absorption and the result was compared with glycerol and water to study the anti-aging potential of LR2412.

(2) Glycerol

Glycerol is a major component of all animal and vegetable fats and oils. It is a well-known cosmetic ingredient that can be obtained from natural sources or easily synthesized, it can be generally found in soaps, toothpaste, shaving cream or any skin and hair care products.

In skin care, glycerol is known as a moisturizer to promote a significant increase of AQP3 and AQP10 gene expression in human keratinocyte culture in vitro, which is related with the water and protein transportation across cell membranes [91, 104].

In this work, deuterated glycerol (Sigma-Aldrich) was diluted in water with a dilution of 50% (mass), the partition coefficient for glycerol is logP = -1.76 (relatively hydrophilic).

(3) Water

Water content in skin is an important sign related with skin age. Water is contained in two ways in skin, bound to proteins (bound water) or bound to each other (bulk water). In young skin, most of the water is bound to proteins, this is important for the structure and mechanical properties of many proteins and their mutual interactions [92].

Therefore, to study molecular penetration and absorption of cosmetic components in skin, water is an important reference. Deuterated water (deuterium oxide) has been purchased from Sigma-Aldrich and used in the following work without further preparation.

In the following chapter, to compare molecular absorption of the three active compounds introduced here (LR2412, glycerol and water), experiments are done individually on reconstructed and excised skin samples with all three molecules.

2.2 Methods

To follow the penetration and the distribution of target molecules in skin, an efficient label free imaging technique, is required. Coherent Raman scattering (CRS) is well known for its chemical sensitivity by granting access to the characteristic vibrational signature [105], CARS microscopy has been used to image topical drug delivery identification [28, 29] and SRS was used for quantitative analysis due to its linear relationship with molecular concentration [23]. Unfortunately, these approaches were not capable of providing unbiased concentration of active compounds for quantitative analysis in thick tissue. Indeed, with increasing depth, the back scattered signal arising from topically applied active molecule in thick skin sample will ultimately become very weak. This signal drop with depth not solely comes from the decreasing concentration profile of active molecule, but also from the optical excitation and collection efficiencies that are affected by absorption and scattering [106].

We designed here a framework for imaging and reconstructing molecular concentration within the depth of artificial and human skin samples (see Fig. 2.7): (1) To reconstruct the concentration map in 3D, we identify the target molecules with CARS microscopy and correct the signal loss caused by optical absorption and scattering with proper normalization, afterwards, the normalized CARS signal is converted to concentration by an "in vitro" calibration using CARS spectroscopy, (Fig. 2.7 red arrow); (2) Samples morphology (reconstructed or excised skin) is imaged by TPEF microscopy (Fig. 2.7 green arrow), to compare the native skin structure with the localization of active molecules; (3) We finally verify the presence of target molecules by comparing the CARS spectrum "in vitro" and "in situ" thanks to CARS hyper-spectral imaging (Fig. 2.7 yellow arrow). With this simple and pragmatic approach, the molecular concentration distribution together with sample morphology could be quantitatively measured in 3D, the results were furthermore compared with SRS microscopy and validated with an established technique using tape stripping followed by liquid chromatography-tandem mass spectrometry anal-

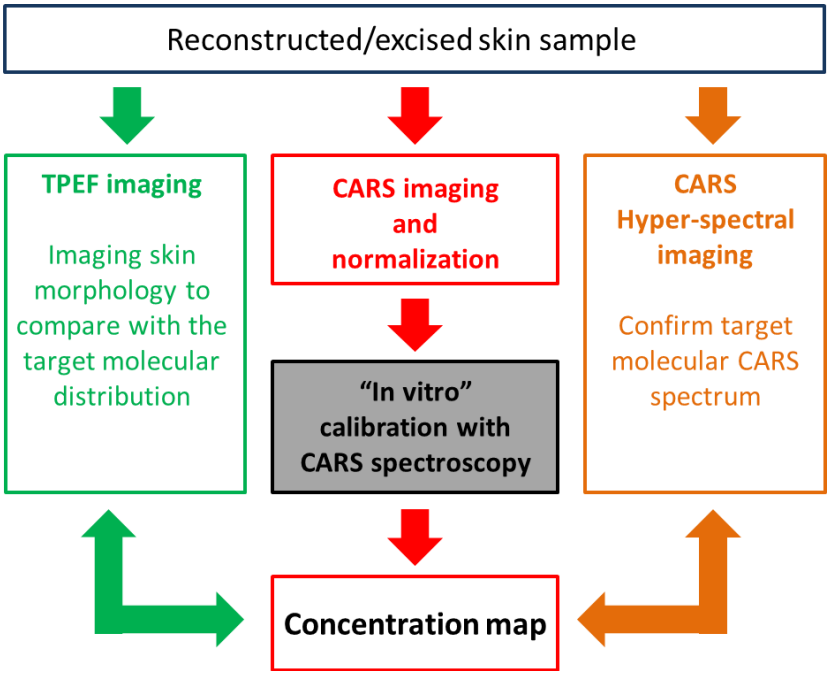

Figure 2.7: Framework of 3D molecular cutaneous absorption quantitative method.

yses (LC-MS/MS) quantification.

The experiments was performed on a custom-built setup incorporating a picosecond stimulated Raman optical source as introduced in Chapter 1 (Fig. 1.13). The two excitation beams from OPO1 (pump) and OPO2 (Stokes) are overlapped in time and space and sent into a custom made scanning microscope. Fig. 2.8 presents the excitation and emission wavelength for C-D bond imaging: OPO1 operates at the fix wavelength of 735nm whereas OPO2 can is tunable to address different vibrational frequency; OPO2 is working at 869 nm to achieve the resonance at 2100 cm^{-1} and tuned to 881nm to excite the non-resonance at 2250 cm^{-1} (for O-D bond: Stokes (OPO2) wavelength is 869nm for resonance at 2350 cm^{-1} and 881 nm for non-resonance at 2500 cm^{-1}). The anti-stokes signal is detected both in the forward and backward directions by means of two PMT (Hamamatsu, H10682) working in photon-counting regime with proper filters. Two-photon excited fluorescence (TPEF) is excited at the same time but mostly by OPO1, the emission range is broad from 400 nm to 600 nm. Excitation and Epi collection is provided by an NA = 1.15 objective lens (Nikon APO LWD water 40 ×) whereas forward collection uses an NA = 0.6 lens (Olympus UCPlan FL 40 ×) (see Fig. 2.5). Incident

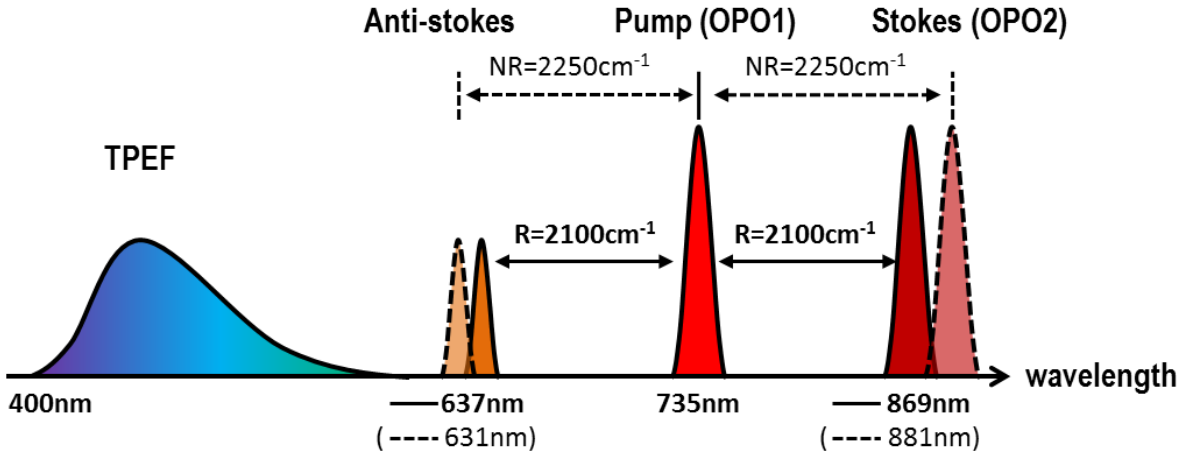

Figure 2.8: Excitation/emission wavelength for C-D bond imaging. Excitation: pump laser from OPO1 is fixed at 735 nm, by tuning Stokes laser (OPO2) from 869 nm to 881 nm we can achieve resonant (solid line) and non-resonant (dashed line) wavenumber. Emission: anti-stokes signal is emitted at 631 nm or 637 nm depending upon the excitation beams; whereas 2-photon fluorescence is emitted in the range of 400 nm - 600 nm.

powers at the sample plane were 30 - 40 mW for the pump beam and 40 - 50 mW for the Stokes beam depending on the samples. TPEF and CARS imaging are performed at the same time. Typical CARS/TPEF images acquired throughout this work are 250 $\times$ 250 pixels, dwell time: 40 μs/pixel, total time for one image 2.5 s.

2.2.1 Imaging skin morphology with TPEF microscopy

First of all, to understand skin and skin samples used in this work, two-photon excited fluorescence (TPEF) microscopy is performed in this section for imaging the structure of skin in the depth of epidermal and dermal layers. TPEF microscopy allows high-resolution imaging of *in vivo* intact tissues, the intrinsic fluorophores in skin are excited and auto-fluorescence is collected to identify skin morphology. Therefore skin layers can be identified by distinguishing the cell types with depth. A 3D skin model can be built subsequently as well.

Skin intrinsic fluorophores

Intrinsic fluorophores in skin allow measurement of native structure without introducing artificial compounds. Tissue native fluorophores are primarily derived from the aromatic amino acids (in the range of UV emission) or from vitamin derivatives which emit at longer wavelengths (400-600 nm) (see Fig. 2.9). Compare with conventional fluorophores or fluorescent proteins such as the GFPs, the intrinsic fluorescence emission are orders of magnitude weaker, therefore the native fluorescence imaging generally requires higher illumination intensities. However, protein binding or association with membranes or lipid droplets may enhance the *in vivo* fluorescence quantum yield, and many autofluorophores are found at extremely high concentrations. In these conditions TPEF can be still quite efficient even within thick tissues.

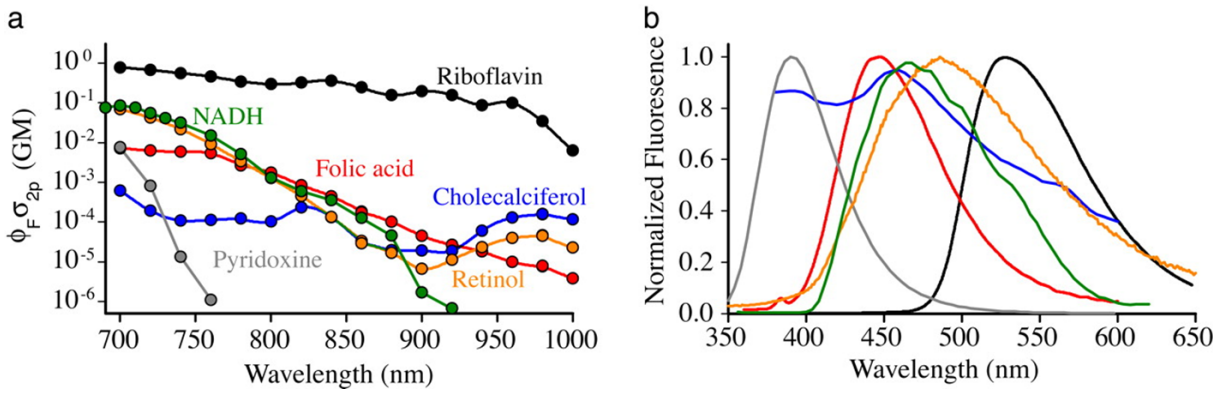

Figure 2.9: Two-photon action cross sections and emission spectra from a basis set of biological molecules. (a) Action cross sections (absorption cross section multiplied by the fluorescence quantum yield) of six molecules that contribute much of the intracellular TPEF intrinsic fluorescence. (b) Emission spectra of these compounds [19].

Figure 2.9a shows TPEF cross sections of several fluorescent vitamin derivatives. The intrinsic imaging is usually carried out in the range of 700 to 750 nm where the 2-photon excitation cross sections are maximal. Fig. 2.9b presents the emission spectra of the same molecules. They cover a wide range of wavelength with overlaps between different compounds, which makes them difficult to be separated, nevertheless, in this work, we take advantage of this spectral overlapping to enhance the TPEF signal by collecting a broad range emitted (400 nm - 600 nm) fluorescence.

Episkin and excised human skin structures

The target molecules cannot be localized without knowing the native structure of the

biological samples. The benefit of using TPEF microscopy is that most of the internal fluorophores in skin are sensitive to near-infrared light, which is just the case of pump lasers used for CARS microscopy, so TPEF images can be obtained at the same time as CARS.

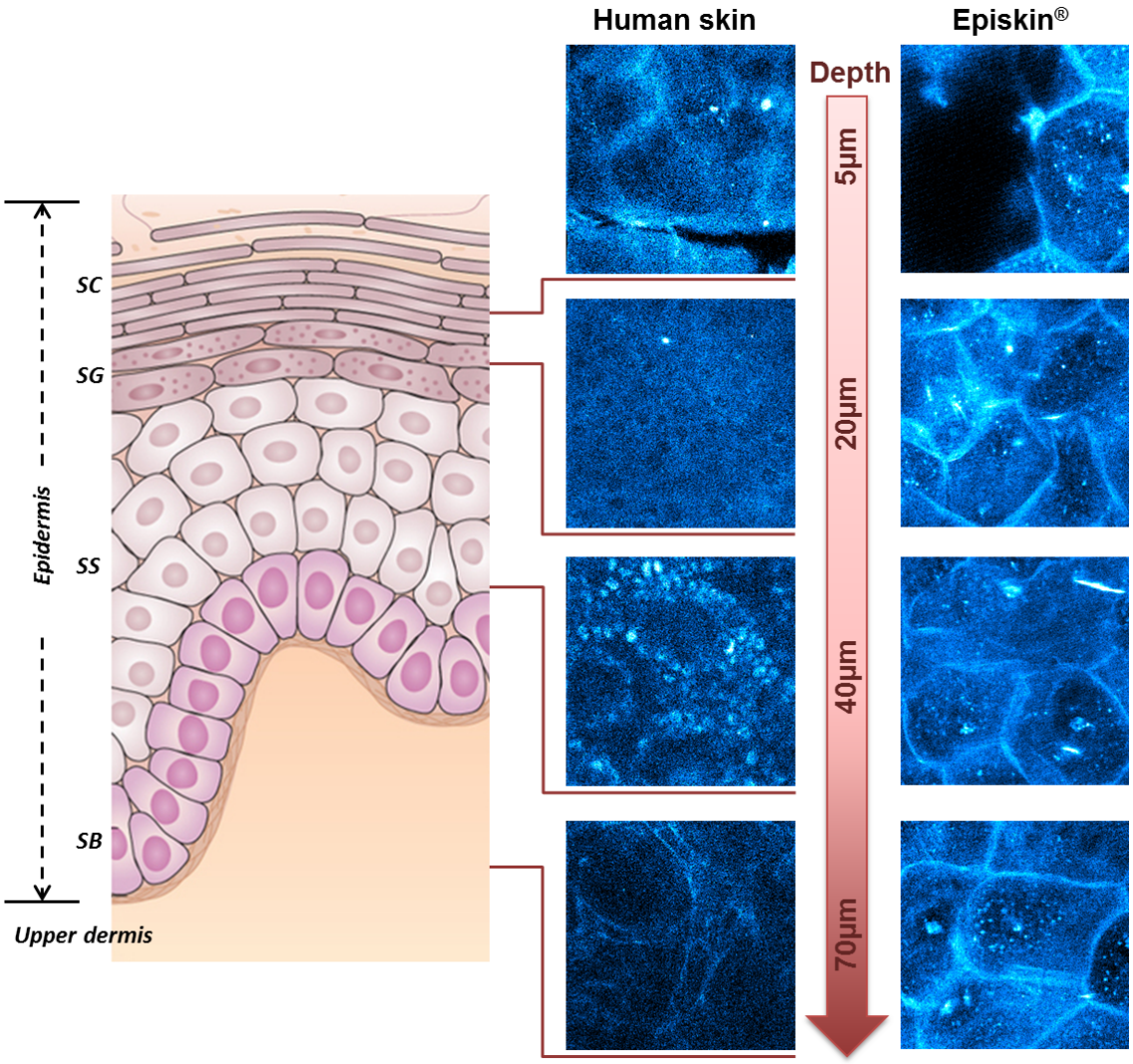

Figure 2.10: Comparison of excised human skin (sample No.1, see Table 2.1) and Episkin morphology by TPEF images (80 μm $\times$ 80 μm) with increasing depth. In human skin, the structure of different layers are visible (compare with skin structure model [86]) until upper dermis. In Episkin, similar cellular formation and organization are observed until the imaging limit due to the thick horny layer.

The reconstructed skin and excited human skin samples were both imaged by TPEF (see Fig. 2.10). The images of excised human skin sample reveal nicely the skin compartment structure: wrinkles and flat corneocyte are visible on the surface (5 μm) in SC; the granular layer can be distinguished by the porous images (20 μm); at the depth of 40 μm, a combination of SS and SB is imaged due to the uneven structure of stratum basal layer; finally the upper dermis is reached when collagen fibers appear (70 μm). A 3D view of human skin is then reconstructed from the image stacks of excised human skin (see Fig. 2.11), where the skin layers can be roughly recognized by their specific cell types. Nevertheless, notice that no sharp interface can be distinguished between layers in human skin. However, in the images of Episkin samples at similar depths (0 - 80 μm), only similar cellular formation and organization can be observed, even until the imaging depth limit. This is due to the thick horny layer present in Episkin samples..

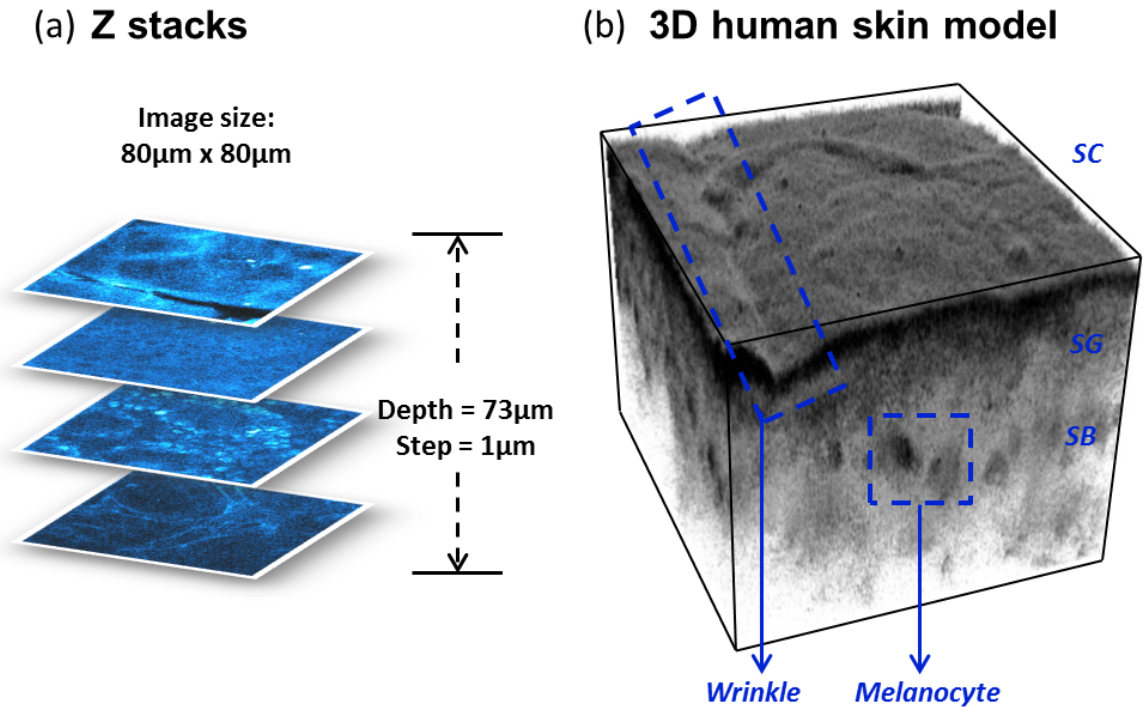

Figure 2.11: 3D model of human skin (sample No.1, see Table 2.1).

According to the morphology difference between this two types of samples, molecular penetration has to be considered with different models: (1) human skin: each of the skin layer interfaces is considered as a barrier with their specific diffusion properties; (2)

Episkin: since only the stratum corneum layer is imaged within the reachable optical limit in this work ($\sim$ 100 μm), this sample type is considered using the 'bricks and mortar' model [107] that describes SC as embedded corneocyte 'bricks' cemented by a lipid 'mortar'.

2.2.2 Identification of target molecules with CARS microscopy

Although CARS is known for its chemical sensitivity compatible with imaging [70], this four wave mixing nonlinear process is associated with a non-resonant contribution that leads to potential spectral and spatial artifacts [108] together with a nonlinear dependence with concentration. Several physical [109, 110] and numerical [111, 112] methods have been described previously to retrieve a linear concentration dependence in CARS imaging, but they come with a number of constrains that make them difficult to implement in heterogeneous and non-transparent media. Furthermore, any attempt to follow vibrational bands that are specific to the targeted active compounds will most likely fall into the skin endogenous CARS signal that extends over the full fingerprint [0 cm^{-1}, 1750 cm^{-1}] and lipid [2800 cm^{-1}, 3000 cm^{-1}] ranges [65].

We follow here a simple and pragmatic approach based on CARS microscopy that aims at (1) by taking advantage of the CARS non-resonant contribution to account for the loss of excitation and collection efficiency along the sample depth; (2) maximizing the signal to noise ratio using deuterated active compounds featuring a carbon deuterium C-D resonance at 2100 cm^{-1} or an oxygen deuterium O-D resonance at 2350 cm^{-1}, both falling within the [1800 cm^{-1}, 2700 cm^{-1}] clear window of biological samples (see Fig. 2.12).

First, two resonant and non-resonant CARS image stacks are acquired successively at 2100 cm^{-1}, $I_R(x,y,z)$, 2250 cm^{-1}, $I_{NR}(x,y,z)$ (C-D bond case) respectively. Following the CARS signal description given in Chapter 1, the spatial resonant and non-resonant CARS signal read:

$$I_R(x,y,z) = |N(x,y,z)\chi_R^{(3)} + \chi_{NR}^{(3)}|^2 MDE(x,y,z) \tag{2.1}$$

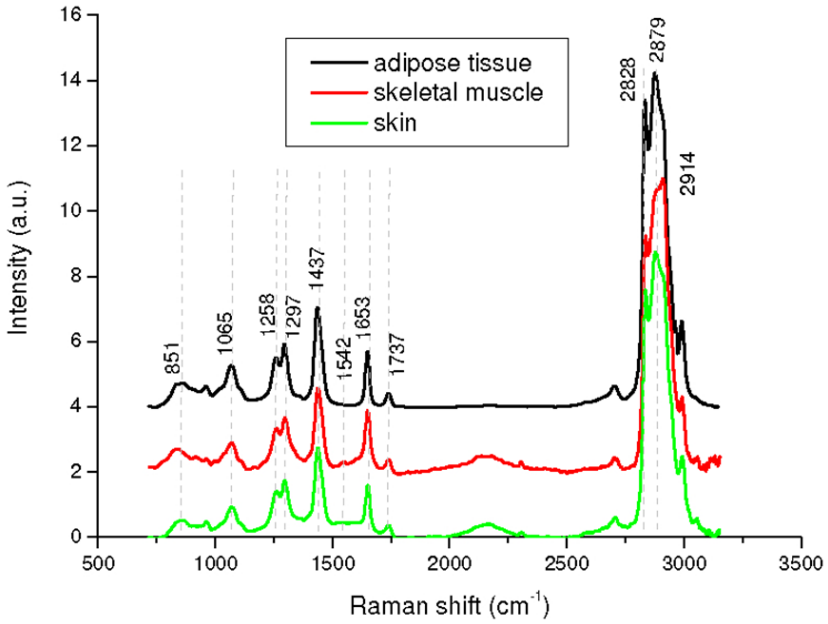

Figure 2.12: Spontaneous Raman spectra of adipose tissue, skeletal muscles and skin [65].

$$I_{NR}(x,y,z) = |\chi^{(3)}_{NR}|^2 MDE(x,y,z) \tag{2.2}$$

where $N(x,y,z)$ is the spatially dependent targeted molecular concentration, $\chi^{(3)}_R$ and $\chi^{(3)}_{NR}$ the resonant and non-resonant nonlinear susceptibilities, and $MDE(x,y,z)$ the molecular detection efficiency accounting essentially for the CARS signal attenuation with increasing depth due to absorption and scattering of both the excitation (pump and Stokes) and CARS fields.

We then defined a normalized CARS signal as:

$$\begin{aligned} I_{Norm}(x,y,z) &= \frac{I_R(x,y,z) - I_{NR}(x,y,z)}{I_{NR}(x,y,z)} \\ &= N^2(x,y,z)\frac{|\chi^{(3)}_R|^2}{|\chi^{(3)}_{NR}|^2} + 2N(x,y,z)\frac{Re(\chi^{(3)}_R)}{\chi^{(3)}_{NR}} \end{aligned} \tag{2.3}$$

that shows to be independent of molecular detection efficiency (MDE). However, Eq. 2.3

describes a nonlinear dependency of I_{Norm} with concentration N. To obtain $N(x, y, z)$ from $I_{Norm}(x, y, z)$, we use an *in vitro* calibration.

2.2.3 *In vitro* CARS signal calibration with concentration

Although the normalized CARS signal I_{Norm} is constructed to be free of any absorption or scattering within the sample depth, it nevertheless shows a quadratic dependency with the targeted active compound concentration $N(x, y, z)$ (see Eq. 2.3). In order to retrieve the concentration from CARS signal, we performed CARS spectra in calibrated compound solutions with different concentrations. From these CARS spectra we can (1) retrieve the quadratic dependence of the normalized CARS signal $I_{Norm}(x, y, z)$ (see Eq. 2.3) with concentration $N(x, y, z)$ and (2) appreciate the maximum dilution level where the CARS signal coming from the targeted molecule is still visible. For dilutions above this upper limit, the CARS spectra are dominated by the non-resonant vehicle solution background. Fig. 2.13 shows the *in vitro* calibrations of LR2412 dissolved at various concentration in propylene glycol (PG).

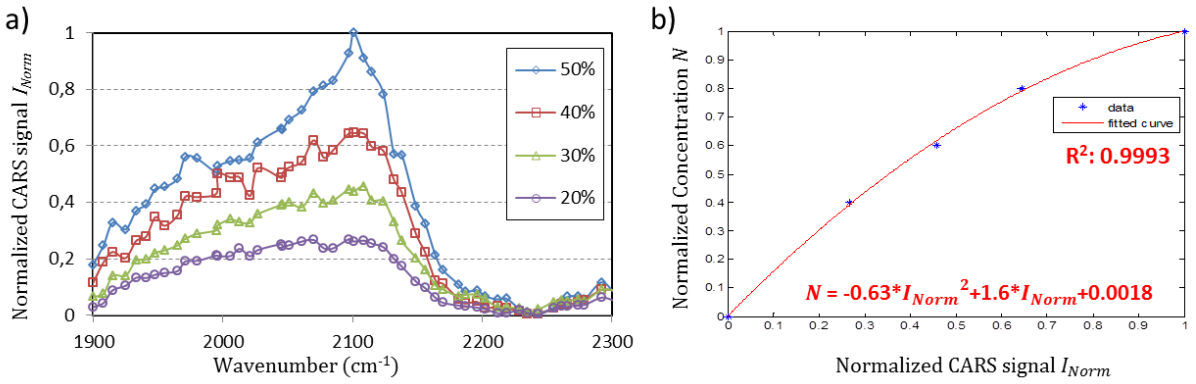

Figure 2.13: CARS signal calibration with concentration. (a) Normalized CARS (I_{Norm}) spectra for different dilution (mass) of active compound LR2412 in buffer vehicle propylene glycol (PG), (b) retrieved concentration from I_{Norm}. The concentration is always normalized 1 that represents the concentration of bulk solution (50% dilution LR2412/PG in this example). R^2: fit parameter.

This *in vitro* calibration scheme for retrieving the active 3D molecular concentration in complex skin samples is valid with the assumption that the non-resonant nonlinear

susceptibilities $\chi^{(3)}_{NR}$ found in skin and in *in vitro* calibrated solution are similar. We will verify this assumption in the next section.

2.2.4 *In situ* molecular characterization by CARS hyper-spectral imaging

In vitro calibration can be performed in this work thanks to the deuterated compounds which have their vibrational frequency in the quiet region of skin samples, otherwise the signal from actiive compounds couldn't been retrieved. Even with this, artifacts are still possible at low active molecule concentrations or large depth. Therefore, in order to avoid misinterpretations, it is safe to confirm the presence of active compounds with CARS hyperspectral imaging.

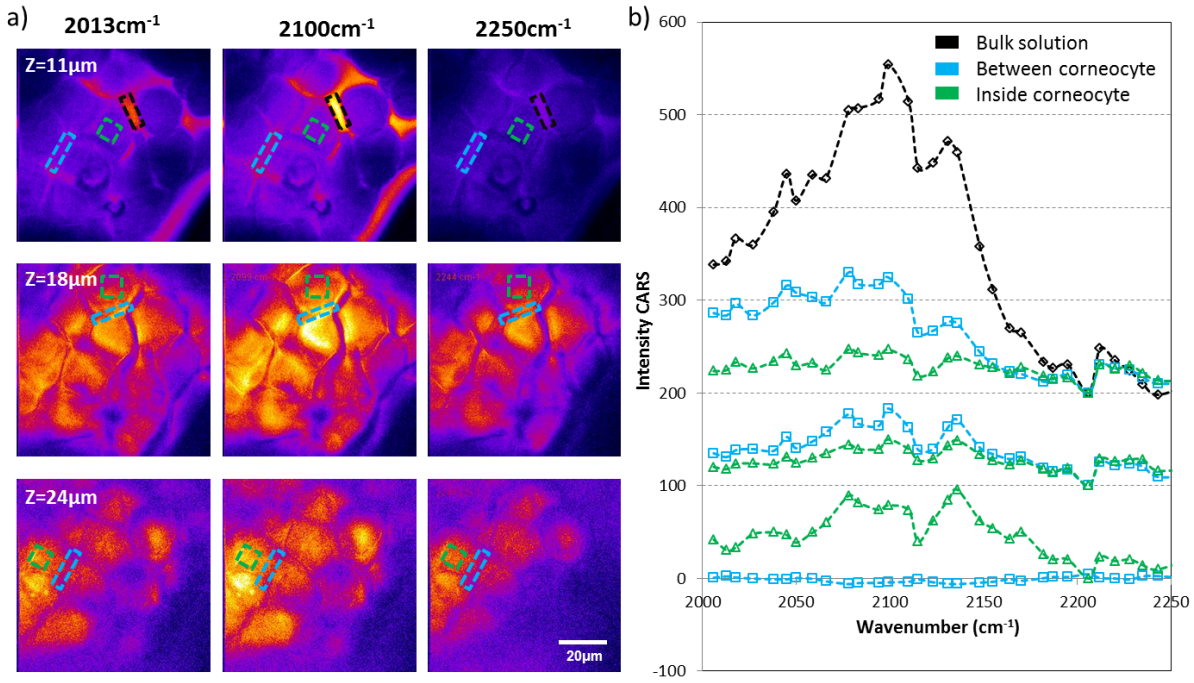

Figure 2.14: (a) CARS hyperspectral images of LR2412 50% on excised skin sample after 24h treatment obtained at three different depths (11 μm, 18 μm and 24 μm). (b)CARS spectra at locations marked in (a), spectral range [2000 cm^{-1}, 2250 cm^{-1}] (C-D bond).

Figure 2.14a shows CARS hyperspectral images of 50% LR2412/PG in excised skin

sample after 24h treatment at the depth of 11 μm, 18 μm and 24μm (within SC). For each depth, three images are presented respectively at 2013 cm^{-1}, 2100 cm^{-1} and 2250 cm^{-1} , the vibrational resonance of C-D bond is obviously achieved at 2100 cm^{-1} (2350 cm^{-1} for O-D bond). The *in situ* CARS spectra over the C-D band region [1900 cm^{-1}, 2300 cm^{-1}] ([2200 cm^{-1}, 2500 cm^{-1}] for O-D bond) are presented in Fig. 2.14b depending on the locations marked in Fig. 2.14a. We focus here primarily on the areas between corneocytes (red) and inside corneocyte (blue) in comparison with the bulk solution (magenta).

Clearly the presence of LR2412 can be ascertained or refuted from the vibrational spectra. The assumption, made in the previous section, stating that the non-resonant background should be similar for in vitro calibrated solutions and real skin proves to be qualitatively the case when looking at the CARS spectra. Indeed, the CARS spectra profiles in skin (Fig. 2.14b) and in the calibrated solutions (Fig. 2.13) show similar dispersive shapes, a feature very dependent of the $\chi_R^{(3)}/\chi_{NR}^{(3)}$ ratio [113]. Such verification is necessary when dealing with weak signals to avoid misinterpretation.

2.2.5 Quantitative active compound concentration with depth

Since we work in conditions where the skin surface is covered with a $\sim$ 50 μm thick liquid layer at known bulk concentration (infinite dose scheme) that is considered to be a reference, it is possible to rescale the 3D concentration $N(x, y, z)$ from the skin surface down to the depth until the sensitivity limit is reached by using *in vitro* calibration.

Figure 2.15 shows an example of concentration mapping (LR2412 on excised skin sample after 24h treatment) from skin surface down to the depth of 40 μm. TPEF images show the morphology of excised skin sample where the stratum corneum is quite thick until $\sim$ 30 μm depth and then stratum granulosum appears, I_{Norm} images are calculated directly from CARS images ($I_{Norm} = \frac{I_R(x,y,z)-I_{NR}(x,y,z)}{I_{NR}(x,y,z)}$) and then converted to N (concentration) by using *in vitro* calibration of LR2412. Compare with I_{Norm} images, the contrast of N (concentration) images is completely different especially when it's going deeper. From skin surface down to 10 μm, they show similar localization of LR2412 surrounding cells, however, I_{Norm} lost its contrast very fast with depth which is due to the decrease of MDE. This is efficiently corrected by *in vitro* calibration to represent the local concentration (N (concentration) images), the fire scale of N is from 0 to 1, which

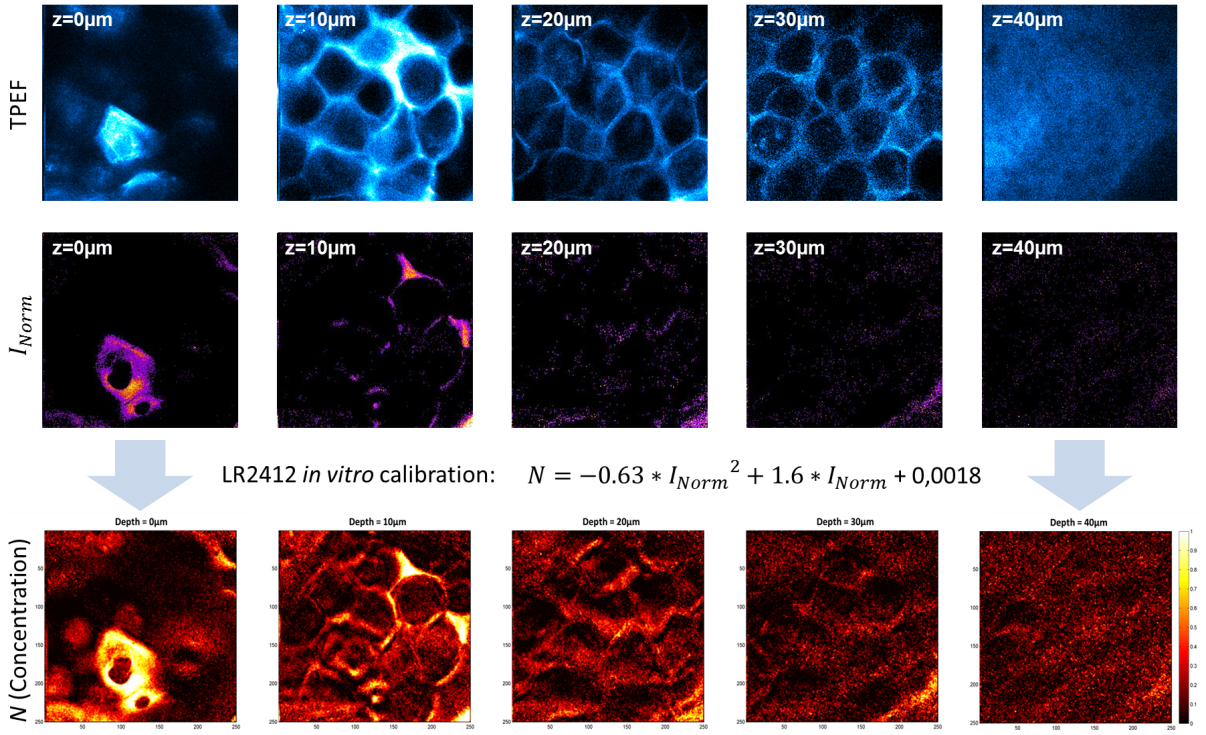

Figure 2.15: An example of concentration mapping in 3D from *in vitro* calibration (LR2412 on excised skin sample after 24h treatment). TPEF images show the morphology of excised skin sample, I_{Norm} images are presented at the same depth and converted to N (concentration) by using its *in vitro* calibration. The fire scale of N is from 0 to 1, which represents 0% concentration to the bulk solution (50% mass in this example).

represents 0% concentration to the bulk solution which is 50% (mass, LR1212/PG) in this example.

2.2.6 Method summary

We have designed a framework [114] for imaging and reconstructing molecular concentration while penetrating within human skin, although valid for any molecule we concentrate in this work on cosmetic active molecules. Pivotal to our approach is the use of deuterated cosmetic molecules in a so-called infinite dose scheme measurement that allows concentration scaling from the surface down to the skin depth. A reliable correction to account

for the loss of excitation power is performed by monitoring the in depth dependency of the CARS non-resonant signal.

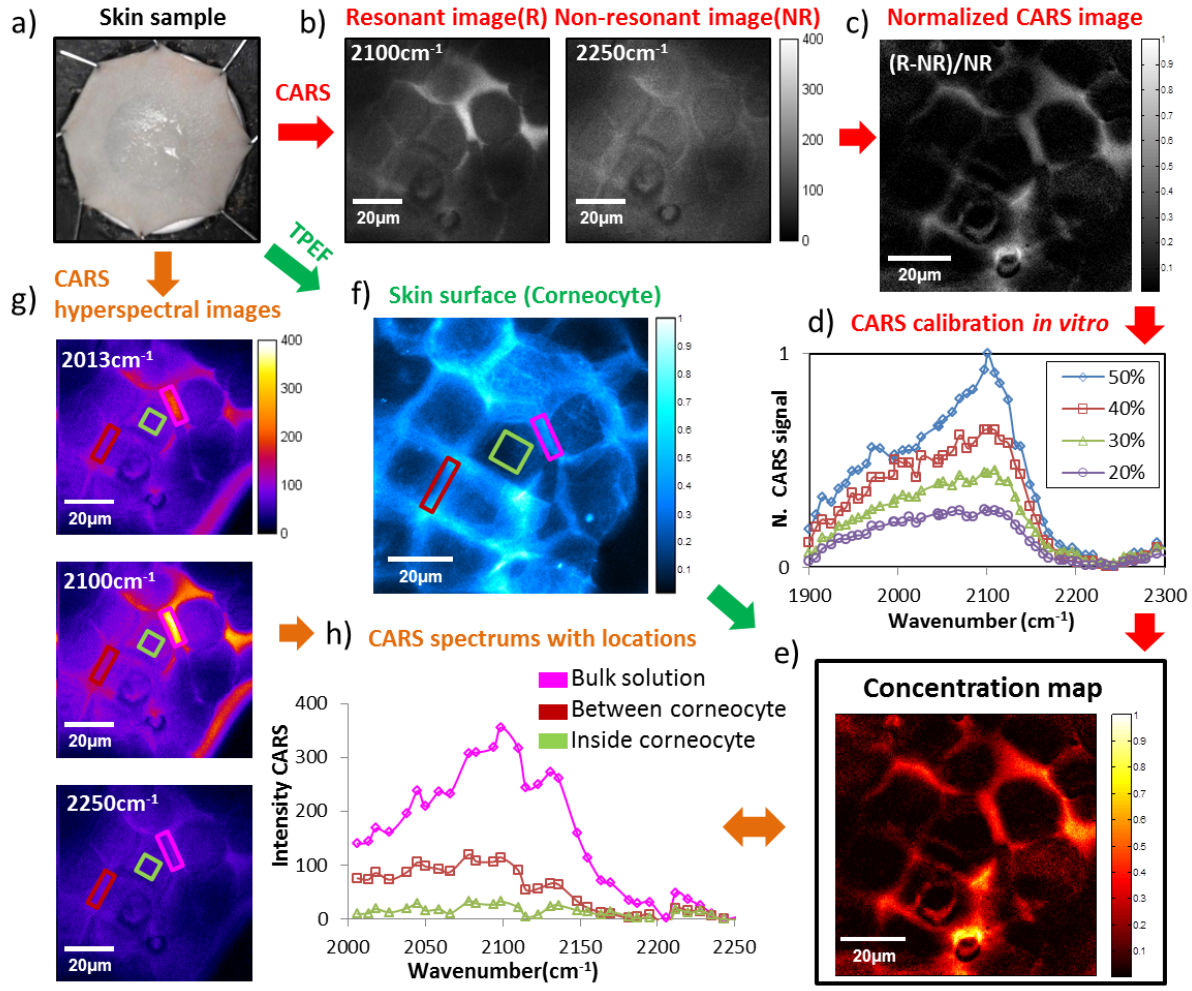

Figure 2.16: Method designed to provide quantitative CARS imaging in skin. Artificial or excised human skin samples (a), are incubated with deuterated active compounds dissolved in their vehicle solutions. 3D-CARS image stacks are recorded at the resonant 2100 cm^{-1} and non-resonant 2250 cm^{-1} (C-D bond case) (b), to construct the normalized CARS signal (c), the latter is connected to local active compound concentration (e), using an in vitro calibration (d). Native TPEF image is acquired simultaneously to provide 3D skin morphology (f), from which hyperspectral CARS images over the C-D band confirm the presence of the active compound (g and h).

According to the process explained in this section, we summarize here on an example of

our methodology (see Fig. 2.16). A sample of excised human skin (Fig. 2.16a) is incubated with deuterated active compounds dissolved in its vehicle solution, two resonant and non-resonant CARS image stacks are acquired (Fig. 2.16b) to construct the normalized CARS image (Fig. 2.16c). The concentration map stacks $N(x, y, z)$ (Fig. 2.16e) are obtained through *in vitro* calibration (Fig. 2.16d), an in-depth native TPEF image stack is acquired at the same time to provide 3D morphological information (Fig. 2.16f), which permit to locate the active molecule in the sample. To confirm that the above procedure always reveals the presence of the target active compound, we perform hyperspectral CARS images (Fig. 2.16g) where CARS spectra coming from various locations (Fig. 2.16h) reveal the heterogeneity of the local active molecule concentration.

Most importantly, for thick biological sample such as skin, most of optical technique (for instance SRS, which is known to scale linearly with concentration [23, 24]) cannot be used to retrieve the active 3D molecular concentration because the signal drop with depth is dominated by the molecular detection efficiency MDE, therefore, the use of the normalized CARS signal for quantitative study is mandatory.

In the following chapter, this framework is performed individually on reconstructed and excised skin samples with three active compounds (LR2412, glycerol and water) introduced in Section 2.1.4 to compare their different penetration pathways. Additionally the results are compared with the other techniques (SRS and LC-MS/MS) to validate our method.

2.3 Results

The experimental results are organized into two parts according to the two types of samples (reconstructed skin and excised human skin). We start first with the reconstructed skin because it is a relatively simple SC skin model. CARS quantitative imaging is performed following topical application or LR2412, glycerol and water. Because forward detection is possible with reconstructed skin, CARS and SRS imaging are easily compared. Excised human skin are more complex and organized in compartments featuring diffusion barriers at their interfaces. We use CARS here again to follow the penetration of LR2412, glycerol and water in these human samples. We also compare the retrieved in

depth concentration evolution with tape stripping method and liquid chromatography - mass spectroscopy quantification (LC-MS/MS).

To understand molecular diffusion with depth and time in skin, we first introduce the molecular diffusion model we use to quantify the results. This diffusion model is valid in a skin without compartment and is therefore well adapted to describe molecular diffusion in SC.

2.3.1 Molecular diffusion model

Molecular diffusion in a homogeneous medium is well described by Fick's diffusion law [115]. Generally, in skin research, transport through the stratum corneum is considered to follow Fickian diffusion through a simple homogeneous membrane [116, 117]. Under the boundary conditions [118]:

- $0 < z < L, C = 0, t = 0$ (the target molecules cannot be found in the SC without topical application; L is the SC thickness and C the target molecule concentration)
- $z = 0, C = C_{z=0} = KC_v, t \geq 0$ (the molecules equilibrate rapidly between the vehicle solution and the SC at the skin surface)
- $z = L, C = 0, t \geq 0$ (the underlying viable epidermis acts as a perfect sink for the molecules)

During the time of penetration, the concentration $C(z,t)$, as a function of depth z and time t , is given by the solution to Fick's second law [119], according to:

$$C(z,t) = KC_v\{1 - \frac{z}{L} - \frac{2}{\pi}\sum_{n=1}^{\infty}\frac{1}{n}\sin(\frac{n\pi z}{L})\exp(-\frac{Dn^2\pi^2 t}{L^2})\} \tag{2.4}$$

where C_v is the active compound concentration in its bulk vehicle solution that is applied during time t, L is the SC thickness, D is the molecular diffusion coefficient and K the partition coefficient (a thermodynamic parameter reflecting the affinity of the active compound for the SC relative to the vehicle solution). This simple model can be applied

to SC with the assumption that (1) all transportation of chemical across the SC is by passive diffusion and (2) the vehicle solution in which the active molecule is presented to the SC does not modify the membrane and act as a carrier for the compound.

However, in the case of excised human skin, the active compound concentration does not drop to zero at L. Therefore, we slightly modified Eq. 2.4 by adding a constant value A to the right-hand side to break the "sink" assumption (at $z = L, t \geq 0; C(z,t) = A$):

$$C(z,t) = KC_v\{1 - \frac{z}{L} - \frac{2}{\pi}\sum_{n=1}^{\infty}\frac{1}{n}\sin(\frac{n\pi z}{L})\exp(-\frac{Dn^2\pi^2 t}{L^2})\} + A \tag{2.5}$$

In steady state condition (t $\rightarrow$ infinity) equation 2.5 reduces to

$$C(z,t) = -KC_v\frac{z}{L} + KC_v + A \tag{2.6}$$

which is a simple linear concentration $C(z,t)$ decreases with depth z in accordance with Fick's first law of molecular diffusion in one dimension [115].

In the following results, Eq 2.5 and Eq. 2.6 are used to estimate the concentration distribution versus depth in non steady state and steady state regimes..

2.3.2 Reconstructed skin: molecular cutaneous absorption

Reconstructed skin samples (Episkin) were incubated with three topically applied active compounds dissolved in their vehicle solutions (LR2412/PG 50%, glycerol/water 50% and water 100%). Incubation time is 1h for LR2412, 1h for glycerol and 20 min for water. As we mentioned before, Episkin is a simple skin model without skin appendages, where cells keratinized at different state are organized into layers and embedded in a lipid matrix (bricks and mortar model). This relatively simple structure allows for fast molecular penetration and steady state regime to be reached in short time.

Figure 2.17 presents the concentration of LR2412, glycerol and water in reconstructed skin samples with depth (fire scale) together with the sample morphology (blue scale). As mentioned previously the concentration (fire scale) is normalized to its maximum level

reached above the skin sample in the bulk solution (infinite dose scheme). In all morphology images (blue scale), the corneocytes can be identified up to a depth of 50 μm revealing a thick stratum corneum, a feature characteristic of this type of reconstructed skin samples. The three active compounds reveal different penetration depths and penetration pathways. For LR2412 (Fig. 2.17a) the concentration images are contrasted and present significant correlations with morphology. Clearly, LR2412 is present both inside and between corneocytes. At lowest depths ($< 30\mu$m) LR2412 concentrates in membranes in agreement with its hydrophobic character, which can be expressed as partition coefficient LogP = 2.6. The penetration pathway of glycerol (Fig. 2.17b) is quite different, at lowest depths ($< 30\mu$m), the concentration is quite uniform whereas weak correlations with morphology appear at larger depth ($> 30\mu$m). This suggest that glycerol penetrates essentially through corneocyte in agreement with its hydrophilicity (LogP = -1.76). Ultimate hydrophilic character can be appreciated when looking at water concentration images (Fig. 2.17c) that show excellent correlation with cell body morphology. Water concentrates principally within cell and shows no affinity for corneocyte membranes.

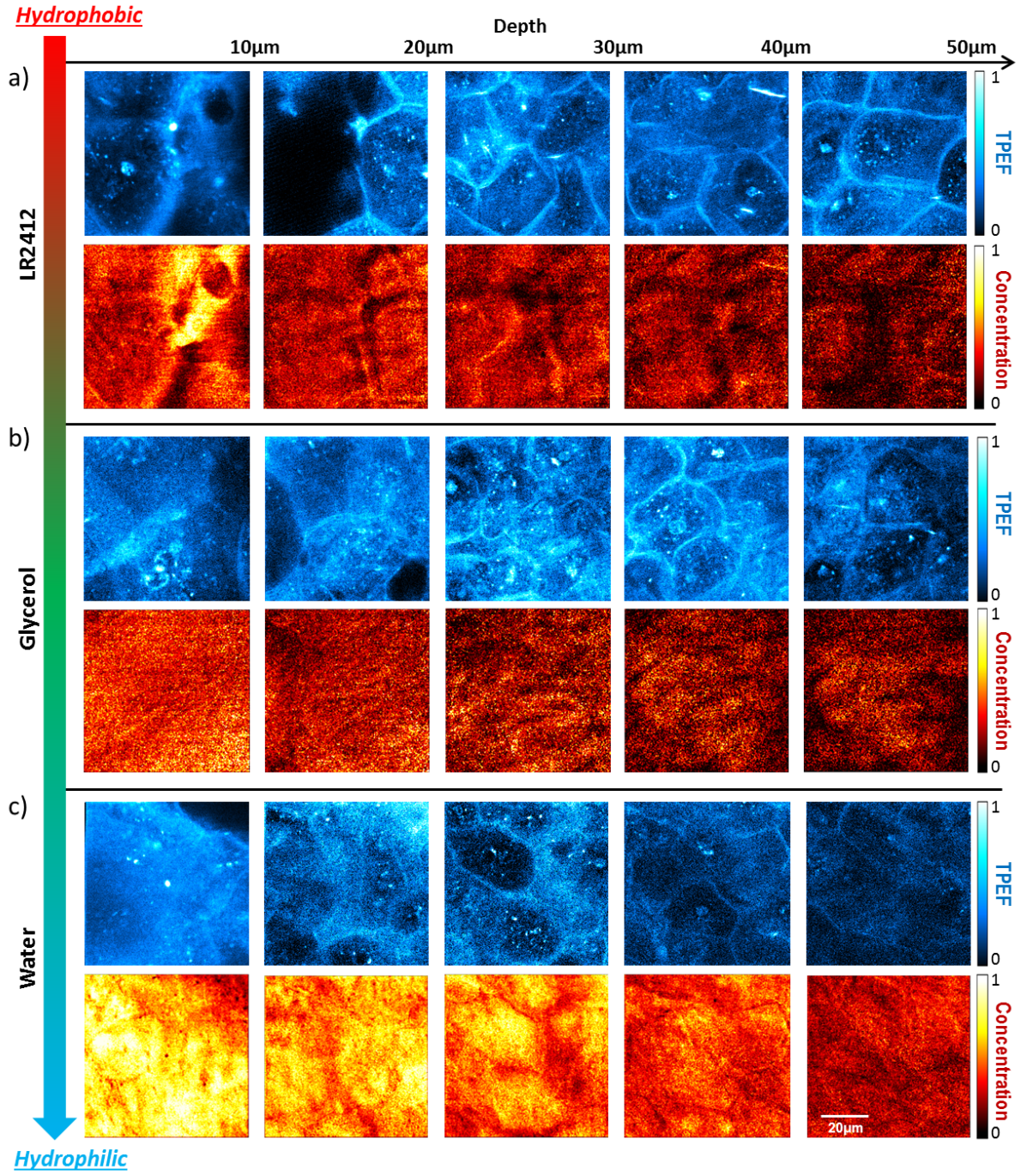

Figure 2.17: 3D molecular cutaneous absorption in reconstructed skin. Concentration of LR2412, glycerol and water in reconstructed skin samples with depth (fire scale) together with the sample morphology (TPEF, blue scale). Morphology (blue scale) is in arbitrary unit, active compound concentration (fire scale) equals 1 in the bulk solution located above the skin sample.

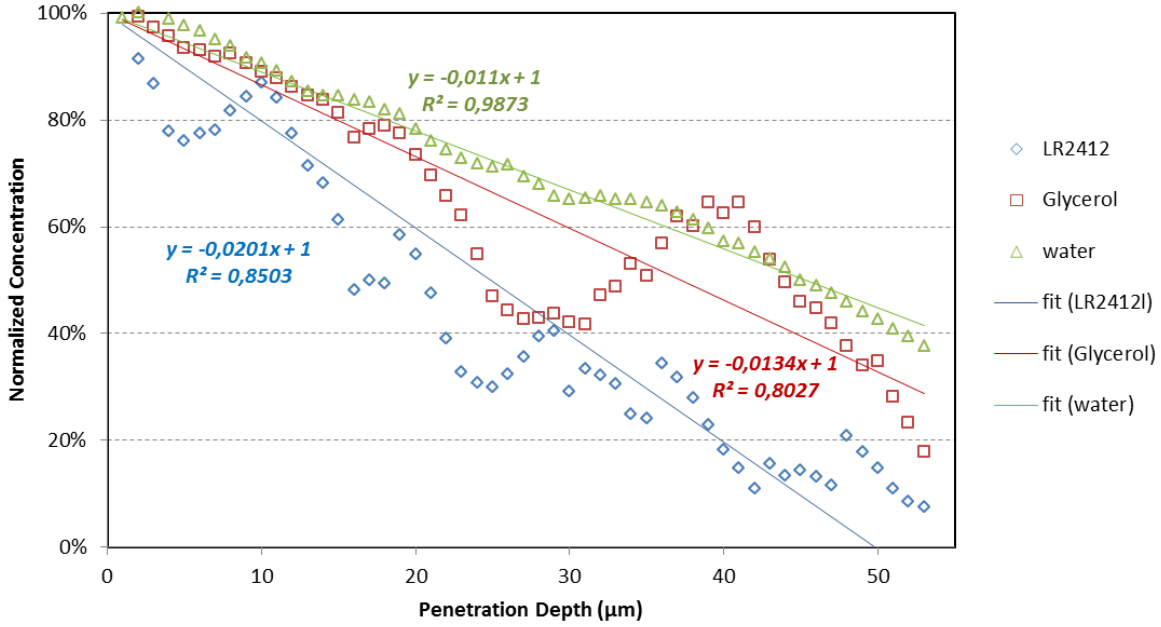

Figure 2.18: Concentration profile of LR2412, glycerol and water with increasing depth and their superimposed linear fits, 100% corresponds to the maximum concentration in the upper SC.

The LR2412, glycerol and water concentration profiles along the skin depth can be better visualized in Fig. 2.18 where in-plane concentrations have been integrated. As before, a concentration of 100% corresponds to the maximum concentration in the upper SC. Some general trends already seen in Fig. 2.17 can be readily confirmed such as the stronger concentration decays with depth for LR2412 and glycerol as compared to water and the non-uniformity of these decay profiles, especially for LR2412 and glycerol that exhibit complex penetration pathways. Quantitatively LR2412 shows a concentration decrease with depth of $2\%/\mu$m whereas glycerol and water concentration drops are $1.3\%/\mu$m and $1.1\%/\mu$m, respectively. These observations have been confirmed on several reconstructed skin samples. We tentatively attribute the oscillations in the LR2412 and glycerol concentration profiles with increasing depth in Fig. 2.18 to the interception between the CARS active detection volume and molecule concentration inhomogeneity due to epithelium irregularities in reconstructed skin samples.

2.3.3 Reconstructed skin: comparison with SRS

As we mentioned previously, SRS signal has been used for quantitative analysis because it is free of non resonant background and shows a linear relationship with concentration. Nevertheless, this technique is not capable to retrieve the molecular concentration in thick tissue because the SRS signal is an intricate combination of concentration distribution and laser beam attenuation upon deep penetration in tissues.

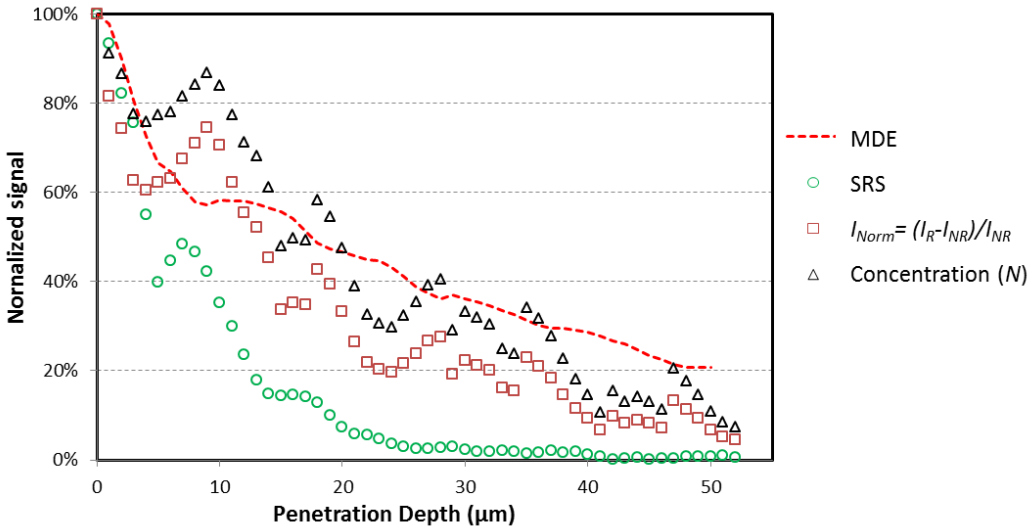

Figure 2.19: Molecular detection efficiency (MDE), SRS, normalized CARS and LR2412 concentration decrease versus depth. The sample is a reconstructed skin treated with active compound LR2412 diluted at 50% (m/m) in PG.

In the case of reconstructed skin that is thinner and more transparent than excised human skin, the MDE should decrease slowly with depth and be more visible, so it is possible to compare the proposed CARS quantitative imaging with SRS imaging in the optimal forward detection scheme. Indeed the absence of skin compartment in reconstructed skin samples and their relative small thicknesses ($\sim$ 100 μm) lead to viable absorption and scattering for CARS and SRS transmission studies. Figure 2.19 shows the molecular detection efficiency (MDE-obtained from the CARS non resonant signal I_{NR}) evolution with depth (dashed line). The MDE drops significantly even for this thin tissue ($\sim$ 1.6% decrease per μm). Figure 2.19 shows also the SRS signal, the normalized CARS signal (I_{Norm}) and the reconstructed active compound concentration (LR2412 diluted 50% in

PG) with depth. Clearly SRS is dominated by the MDE drop with increasing depth and cannot retrieve the active molecular concentration. On the opposite the proposed scheme using I_{Norm} proves to be superior to take into account the signal attenuation with depth (see Fig. 2.19).

2.3.4 Excised human skin: molecular cutaneous absorption

Excised human skins from abdominal plastic surgery (frozen or fresh samples) were incubated with three topically applied deuterated active compounds dissolved in their vehicle solutions (LR2412/PG 50%, glycerol/water 50% and water 100%, the same as for Episkin). Incubation has been performed for 4h and 24h prior to nonlinear imaging. Penetration of active molecules is longer in human skin than in Episkin [120], mostly because of the complex organization of human skin. For some molecules, it takes more than 4h to reach the steady state.

Figure 2.20 shows the results obtained after 24h incubation time, when steady state is reached, for LR2412 (Fig. 2.20a, b), glycerol (Fig. 2.20c, d) and water (Fig. 2.20e, f). Skin morphology (blue scale, TPEF) and molecular concentration (fire scale) are displayed in Fig. 2.20a, c, e, where morphology is in arbitrary unit (blue scale) and active compound concentration (fire scale) is normalized to its maximum level reached above the skin sample in the bulk solution. The molecular concentration profile along the skin depths is plotted in Fig. 2.20b, d, f, a concentration of 100% corresponds to the maximum concentration in the upper SC. For relevancy, we have also highlighted in Fig. 2.20b, d, f the skin layer compartments (backgroud colorbar) that can be roughly identified from TPEF morphology images. No sharp interfaces can be defined because of the natural fuzzy structure of human skin. In each barrier compartment, a linear fit (according to Eq. 2.6) is superimposed with the concentration decay together with its regression parameters p1 and p2. The linear concentration decay found experimentally in each skin compartment is consistent with our assumption that the molecular diffusion process can be modeled by the Fick's law in each skin compartment.

The studies of LR2412, glycerol and water were performed on samples coming from different donors due to availability constrains, this caused slight differences in sample morphologies and barrier thicknesses. Depending on the excised human skin samples

and the applied treatment, one can basically identify stratum corneum (SC), stratum granulosum (SG), stratum basal (SB) possibly in combination with stratum spinosum (SS) and upper dermis. The deepest morphology image (TPEF), down to to upper dermis, can be obtained with samples (No.2, coincidently thin) treated with glycerol that is known to act as clearing agent in skin (Fig. 2.20 c) [121].

Penetration pathways show a marked diversity when considering the three studied active compounds. LR2412 concentrates into the corneocyte and keratinocyte membranes up to the detectable limit in SG (Fig. 2.20a). Quite remarkably, LR2412 concentration profiles with depth show a first derivative discontinuity at the SC/SG interface (Fig. 2.20b) highlighting a clear diffusion barrier. Note that the skin barriers, at the SC/SG and SG/SB interfaces, are seen independently from skin morphology (TPEF images) and are clearly highlighted from concentration slop changes. The penetration pathway of glycerol appears to be quite different than LR2412 and concentrates both in cell bodies and cell membranes down to the upper-dermis where the signal is lost (Fig. 2.20c). When displayed along the skin depth, glycerol concentration first derivative shows clear discontinuities at the SC/SG and SG/SB interfaces (Fig. 2.20d). Water penetration is quite homogeneous except at larger depth (40 μm) where exclusion zones are revealed when reaching the epidermis-dermis junction (Fig. 2.20e) (note that in the case of water, images are 50 μm x 50 μm). Similar to LR2412 and glycerol, water concentration profile first derivative show marked discontinuities at the SC/SG and SG/ SB interfaces exemplifying here again the importance of skin layer barriers in percutaneous diffusion processes. On Fig. 2.20b, d, f are superimposed linear fits performed independently in SC, SG and SB. Quite interestingly, although the penetration pathways are very different for LR2412, glycerol and water (see Fig. 2.20 a, c, e), the concentration profiles with depth look roughly the same for these three compounds with a $\sim 50\%$ concentration drop in SC, a constant concentration in SG and a uniform drop with the same slop in SB ($\sim 1.5\%$ μm).

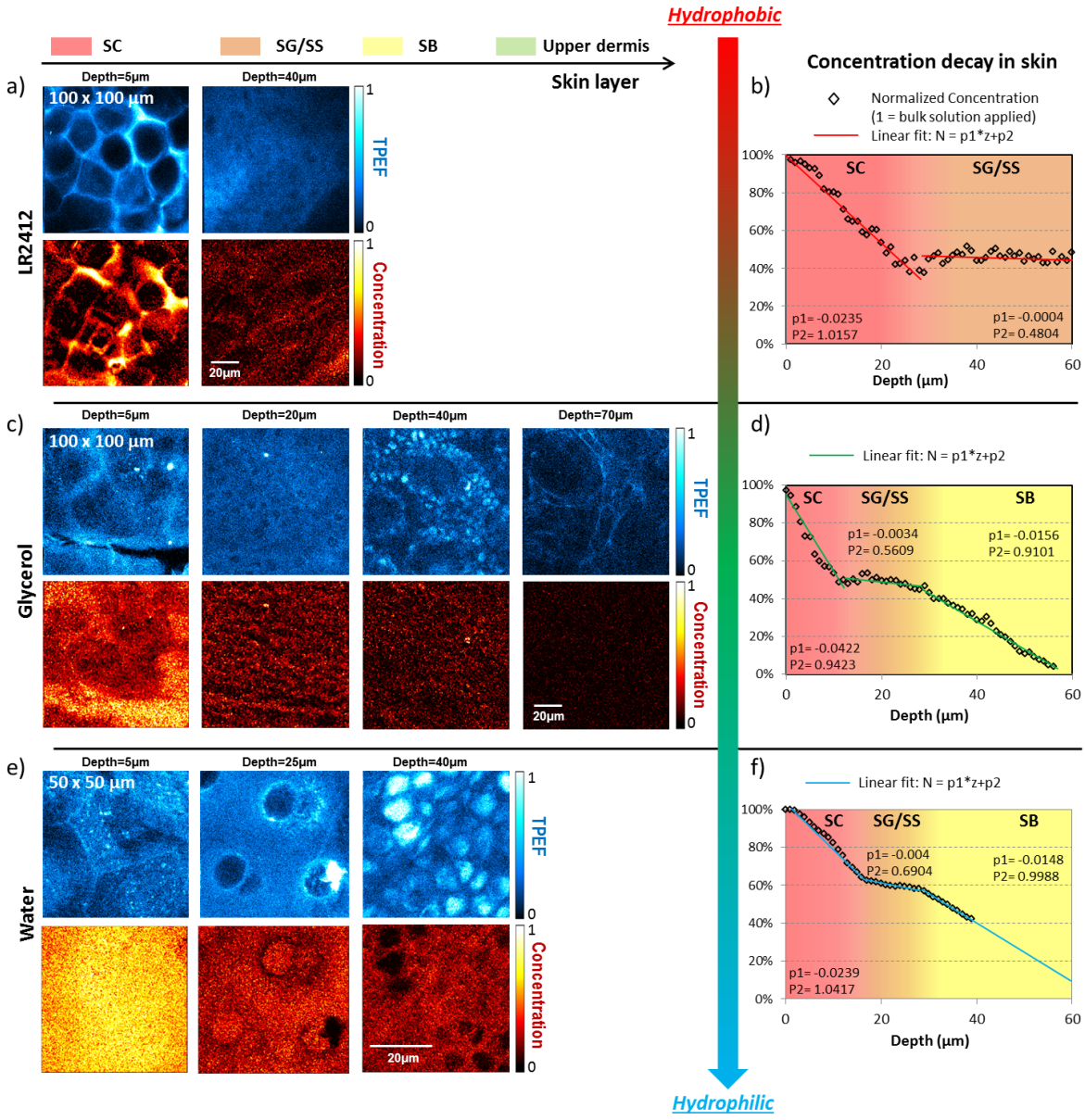

Figure 2.20: 3D molecular cutaneous absorption in excised human skins after 24h incubation time for LR2412, glycerol and water. (a) Sample No.2 morphology and LR2412 concentration, (b) LR2412 concentration profile with depth and its linear fit in each barrier, (c) sample No.1 morphology and glycerol concentration, (d) glycerol concentration profile with depth and its linear fit in each barrier, (e) sample No.1 morphology and water concentration, (f) water concentration profile with depth and its linear fit in each barrier. SC: stratum corneum, SG: stratum granulosum, SB: stratum basal.

Non steady state regime observed after 4h incubation

Non steady state regime is interesting because it reveals the dynamic of diffusion. LR2412 is a viscous and hydrophobic product that penetrates slowly into skin, with which we could have opportunity to observe non steady state regime after 4h incubation time (steady state is obtained after 24h).

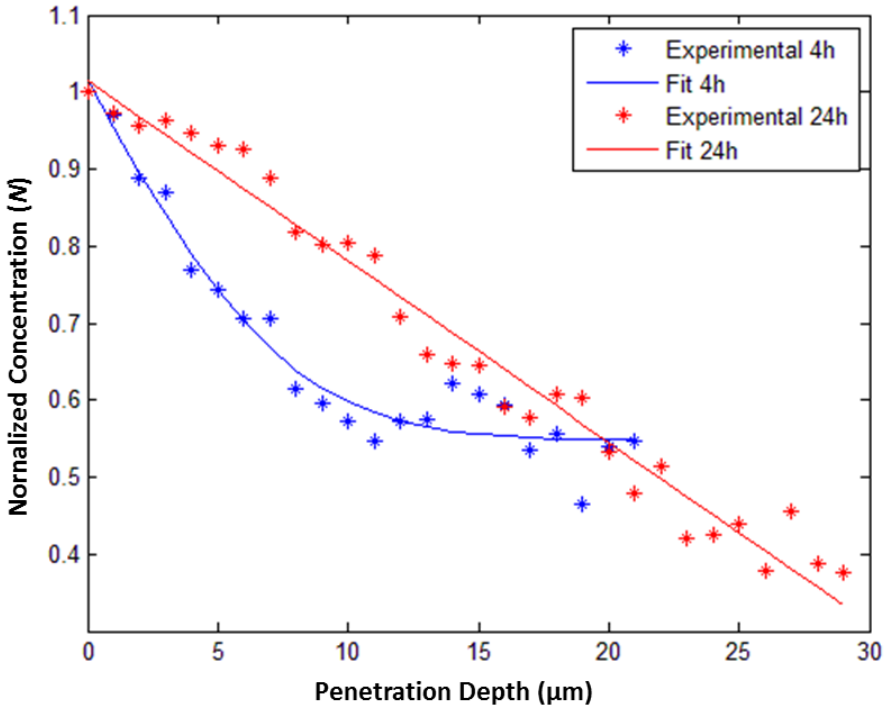

Figure 2.21: Non steady state in comparison with steady state. LR2412 concentration versus depth in SC for 4h incubation time (non steady state) with its best fit according to Eq. 2.5 and 24h incubation time (steady state) with its best fit according to Eq. 2.6.

Fig. 2.21 shows the LR2412 concentration versus increasing depth in SC for 4h and 24h incubation time, together with the their best fitting curves according to Eq. 2.5 and Eq. 2.6. According to the diffusion model described in Section 2.3.1 (Eq. 2.5), in the process of molecular diffusion, the diffusion time t is only in an exponential function with concentration $C(z,t)$. Thus, at the beginning of the diffusion process (non steady state), the function of $C(z,t)$ versus penetration depth z has an curve profile with an exponential shape (Fig. 2.21, blue), which represents that the steady state is not reached at t = 4h; With the increased diffusion time, the exponential part in the equation is closing to 0,

which represents that the concentration in this case is not related with diffusion time (Fig. 2.21, red), thereby the the steady state is reached at 24h and the molecular diffusion profile shows an linear decay.

From non steady state regime, we find D = 4.7 ± 1.8 μm^2/h for LR2412 diffusion coefficient in SC of this excised human abdominal skin sample and the kinetic parameter D/L^2 is $\sim$ 0.011 h^{-1}. Those values reflect the molecular permeability in skin, which does not only depend on the properties of active molecules but also is significantly influenced by their vehicle solutions (for the same sample). For instance, ibuprofen, which is a component for the common anti-inflammatory drug, is dissolved in different solutions (Artofen, Brufen, Iprogel and Optifen) and applied on skin surface, the kinetic parameter D/L^2 was found completely different ($\sim$0.072 - $\sim$0.211 h^{-1}) [117]. Thus, the diffusion coefficient D represents only the situation when LR2412 is diluted in PG of 50% mass.

Commonly that the topical applied solution can increase slightly the thickness of the skin, this phenomenon is especially obvious when LR2412 was applied due to its active effect [15, 102]. In Fig. 2.21, from 4 to 24 hours, the thickness of SC is extended, thus the 2 concentration curves are fitted until different depth, and finally at $\sim$ 20 microns, 4h and 24h are ended at the same concentration. Nevertheless, there is a "cross" between the 2 curves at the end of initial SC thickness, which does not represent that the concentration at 4h will "catch up" 24h, but due to the points that can not be precisely selected for the fitting model. Because there is no strictly defined interface between SC and SG layers (it is defined in this work by the morphology corresponding to two-photon fluorescence images).

Time sequence comparison for functional study

Besides studying steady state, we can also compare molecular diffusion with time and sample alteration with topical applied treatment, especially for cosmetic functional studies. Figure 2.22 shows the LR2412 and glycerol concentration profiles for 4h and 24h incubation time. For each active compound, the experiments were performed on the same excised human skin sample. In the case of LR2412, the sample under test (No.2, see Table 2.1) presents a thick ($\sim$ 20 μm) SC that shows a 30% inflation ($\sim$ 30 μm) from 4h to 24h incubation, and the same happened for SG layer with a 20% thickness increase. This is likely the result of tissue swelling due to prolonged hyper-hydrated conditions [15, 102].

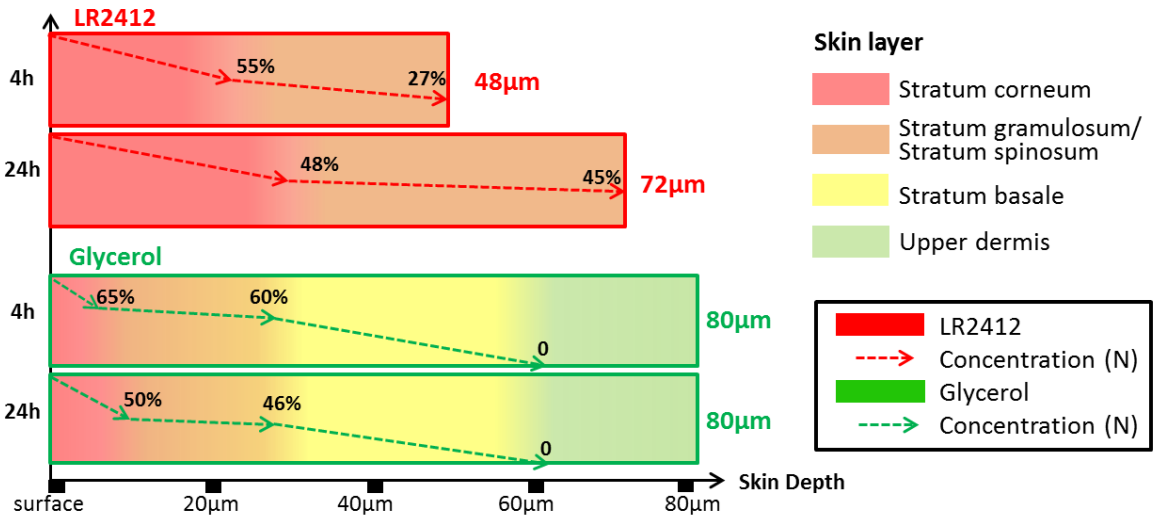

Figure 2.22: LR2412 and glycerol in-depth concentration profile for 4h and 24h incubation time. For each active compound, the experiments were performed on the same excised human skin sample (No.2 for LR2412 and No.1, for glycerol, see Table 2.1).

When comparing the LR2412 concentration profile with increasing depth in SG between 4h and 24h incubation, the non-zero (4h) to zero (24h) concentration gradient (first derivative), clearly indicates that after 4h steady state is not reached. The situation is different for glycerol which shows a very similar in-depth concentration profile after 4h and 24h incubation reaching in both cases 60 μm in SB, which shows that steady state is reached after 4h incubation with this sample (No.1, see Table 2.1).

2.3.5 Excised human skin: comparison with LC-MS/MS

In order to evaluate the validity of our CARS quantitative molecular concentration approach we performed on the same skin sample CARS quantitative imaging and sequential adhesive tape stripping followed by liquid chromatography-tandem mass spectrometry analyses (LC-MS/MS).

As it is showed in Fig. 2.23, the chromatographic analyses were performed using HP1200 series system (Waldbronn, Germany) interfaced with a API3200^{TM} LC-MS/MS system (Applied Biosystems, Foster City, USA) by a Turbo V^{TM} interface equipped with

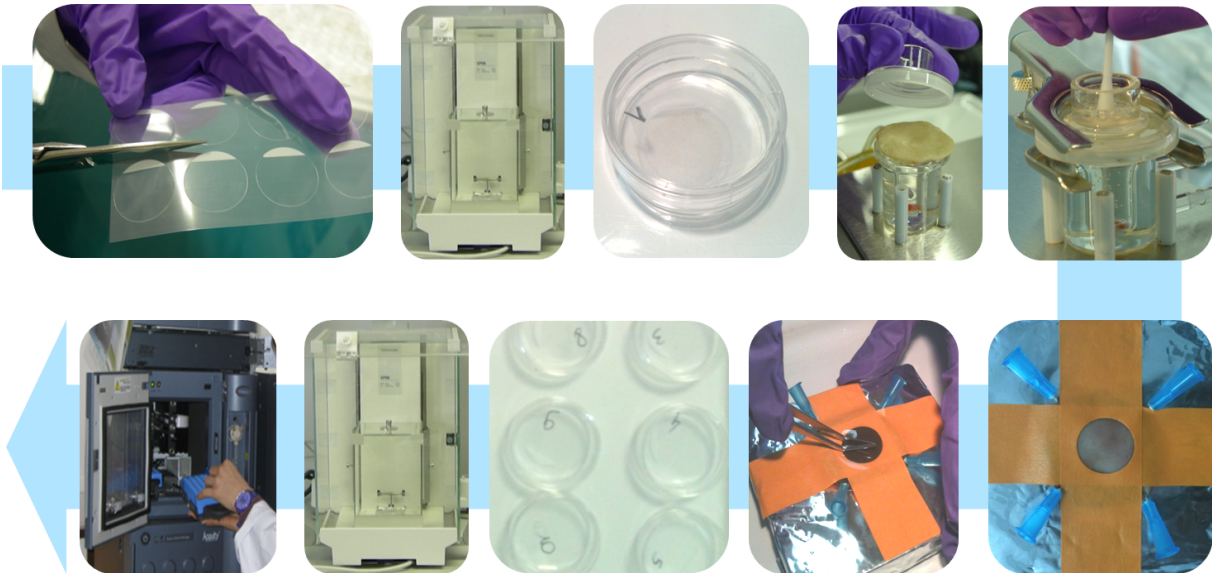

Figure 2.23: Tape strapping method and liquid chromatography-mass spectrometry measurement on fresh excised human skin sample.

an ESI probe. Separation was performed with Ascentis Express C18 (4.6 mm × 100 mm, 2.7 μm, Supelco, Bellefonte, PA, USA). The column was eluted with a gradient over 6 min at a flow rate of 0.4 mL.min^{-1}. Mobile phase used for separation consisted of 0.1% (v/v) aqueous formic acid as solvent A and MeOH as solvent B. The injection volume was 50 μL and the temperature of the column oven was kept at 45 °C. The detection was made with electrospray ionization operating at negative ion mode and the tandem spectrometer was operated in the multiple reactions monitoring (MRM) mode. The mass spectrometric conditions were optimized for LR2412 detection. The optimized parameters were as follows: turbo ion spray temperature: 550 °C; ion spray voltage: - 4500 V; de-clustering potential: - 60 V; entrance potential: - 4 V; collision energy: - 28 V; collision cell exit potential: - 2 V. The ion transition chosen for MRM were m/z 213.1 → 167.1 for LR2412 and 211.3 → 58.9 for its internal standard.

We concentrate on LR2412 penetration in a fresh excised human skin sample (No.3, see Table 2.1). LR2412 incubation has been performed for 24h prior to CARS imaging. The skin was then washed to remove non-absorbed LR2412 and tape stripped. For each strip, the removed skin thickness was determined by pre and post-weighting (assuming a skin density of 1) whereas LR2412 quantification was determined using LC-MS/MS. Fig-

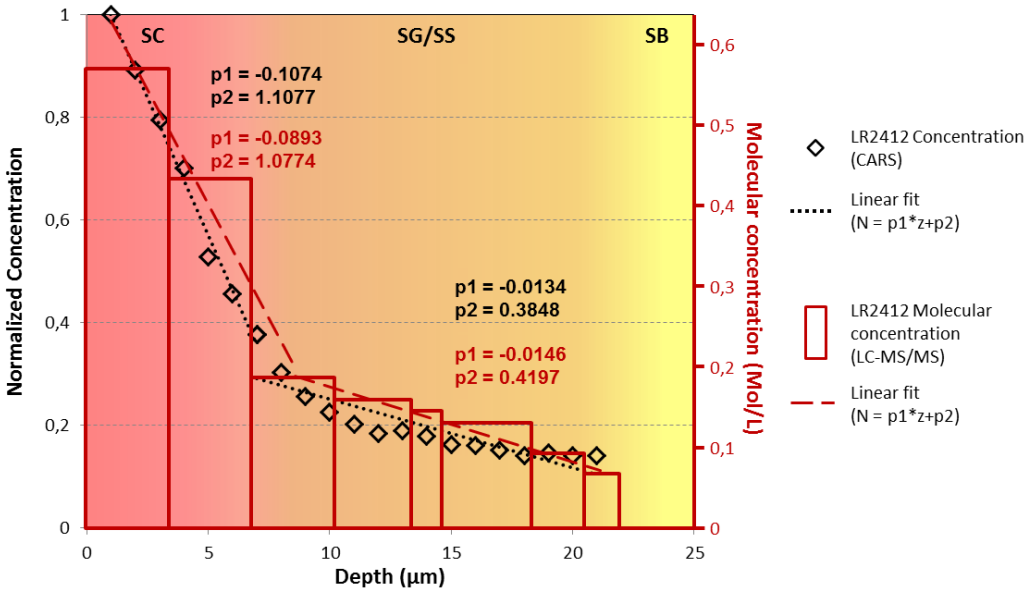

Figure 2.24: LR2412 concentration in a fresh excised human skin sample: comparison between CARS quantitative imaging (open marker) and LC-MS/MS measurements (bars). Fits are superimposed together with their quantitative parameters (CARS: black and dotted line; LC-MS/MS: red and dashed line).

ure 2.24 presents the LR2412 concentration with increasing depth obtained from CARS imaging (open markers) superimposed with the concentration obtained from tape stripping and LC-MS/MS measurements (bars). The quantitative agreement between the two approaches is quite noticeable. Both approaches confirm (1) the existence of a clear diffusion barrier at the SC/SG interface, (2) a significant concentration drop in SC and (3) a slowly decreasing concentration profile in SG.

2.4 Discussion and Conclusion

Our methodology to retrieve the molecular concentration of active compounds in skin samples requires CARS resonant ($2100cm^{-1}$ C-D or $2350cm^{-1}$ O-D) and non-resonant ($2250cm^{-1}$) image stacks together with TPEF imaging to access 3D skin morphology. Furthermore, hyperspectral image is useful to confirm the presence of the targeted deuterated molecular active compound. Indeed, working only with the resonant and non-resonant

signal is not always reliable as a non-zero difference between the two signals is sometime due to noise only. We found that a clear view of the C-D (O-D) spectrum (using CARS spectroscopy) around $2100cm^{-1}$ (or O-D spectrum around $2350cm^{-1}$) and its localization avoid many misinterpretations. It takes 2.5 s to acquire a 250 $\times$ 250 pixels CARS images (pixel dwell time 40μs) and 5$\sim$10s to change the OPO wavelength between two wavenumbers. In total a full sample is analyzed within 30 minutes. There are clearly room for improvement here using faster hyper-spectral CARS/SRS imaging modalities [122].

Reconstructed skin samples are interesting, despite default in their barrier function [120, 123], because they provide a relatively simple approximation of the human skin SC as confirmed by TPEF images. In these samples we observed a quasi-linear concentration decrease with increasing depth. This is in agreement with molecular diffusion model in steady state that postulates that the flux goes from regions of high concentration to regions of low concentration, with a magnitude that is proportional to the concentration gradient. Describing the diffusion process with Fick's law is simplistic and hides the complex diffusion pathways for the different considered active molecules. Clearly SC shows at least two different pathways through (1) the corneocyte bodies and (2) their intercellular lipids. This is consistent with the 'bricks and mortar' model [107] that describes SC as embedded corneocytes 'bricks' cemented by lipids 'mortar'. LR2412 shows stronger affinity for the lipid mortar whereas water penetrates more homogeneous and through the cell bricks. In between, glycerol reveals to penetrate both through cell bricks and lipid mortar. Although such results are in agreement with the relative hydrophobicity of LR2412 and glycerol, the diffusion process is spatially and temporally governed by a 3D inhomogeneous structure consisting in first approximation of a 3D lipid mortar mesh with embedded confinement zones (cell bricks). Quite interestingly, a detailed inspection of Fig. 2.17 shows that LR2412 is more visible in the lipid mortar at low depth ($< 30\mu$m) and in the cell bricks at larger depth ($> 30\mu$m), the same situation can be also observed in SC of excised human skin in Fig. 2.14. This gives strength to the statement that the lipid mortar and cell bricks pathways are different.

Excised human skin samples present a higher complexity than reconstructed skin because they show not only complex diffusion pathways, but also morphological barriers at the SC/SG and SG/SB interfaces that correlate nicely with diffusive barriers for the considered active compounds. This is clearly seen independently on TPEF (Fig. 2.20) and gradient (first derivative) discontinuities in the retrieved in-depth concentration profiles

(Fig. 2.20). The affinity of LR2412 for SC lipid mortar is confirmed but shows to be stronger than in reconstructed skin, this trend also partially extends in SG. This constant concentration profile in SG confirms that steady state has been reached after 24h incubation time. The gradient discontinuity at the SC/SG interface is also found for glycerol and water. This is consistent with recent developed model for estimating bioavailability of chemicals through the SC, viable epidermis and dermis [124]. Glycerol shows penetration pathway partially through corneocyte bodies in agreement with the reconstructed skin observation. Interestingly, TPEF and CARS images are extended down to 70 μm when using glycerol (due to optical clearing [121]) that permit to follow glycerol concentration decay down to its zero limit in upper dermis. Water concentration is found very homogeneous except in exclusion zones found at the epidermis-dermis junction. The similarity between concentration profile decay with depth for LR2412, glycerol and water confirms that (1) the steady state is attained after 24h and (2) that the SC/SG, SG/SB barriers are of similar strength for the three studied active compounds.

The excellent agreement between CARS quantitative imaging and tape stripping/LC-MS/MS quantification (Fig. 2.24) demonstrates the validity of our approach to retrieve active compound concentration profiles with increasing depth based on vibrational imaging only. Because we used a fresh excised human skin sample for this comparative experiment (tape stripping is hardly possible on frozen sample), it also demonstrates that the main features observed on frozen samples treated with LR2412 (Fig. 2.20a b) remain true on fresh samples. Indeed, in Fig. 2.24, a clear diffusion barrier is seen at the SC/SG interface, a rapid concentration drop with depth in SC, and a smooth concentration decrease in SG are confirmed.

In conclusion, we have designed a framework for imaging and reconstructing molecular concentration within the depth of artificial and human skin samples using CARS and native TPEF. 3D concentration mapping of deuterated active molecular compounds in complex sample such as reconstructed skin and excised human abdominal skin samples have been studied. The reported methodology gives unprecedented information such as the 3D penetration pathway that is not accessible using standard approaches to quantify active compound penetration in skin. Studying reconstructed skin samples, we have highlighted the complex interplay between the diffusion through corneocyte 'bricks' and the lipid 'mortar' that dictates the penetration of active compound depending on their hydrophobicity. Excised human skin samples bring higher the degree of complexity with the

appearance of diffusive barriers between epidermis and dermis compartments. Although such diffusive barriers were known, our approach brings novel information in terms of active compound mapping and its relation with tissue organization. Such an achievement is made possible with the combination of label free, molecular specific and quantitative coherent Raman microscopy (CARS) together with unspecific native auto-fluorescence (TPEF). The development of such optical techniques should shine a new light on percutaneous absorption and tissue bioavailability, there are furthermore fully compatible with in-vivo investigations on human bodies [125].

Chapter 3

Eccrine sweat gland and antiperspirant activity - *in vivo* study

The structural complexity and functional importance of human skin is not only embodied by its multiple layers [3], but also by its various cutaneous appendages located in skin, such as hairs follicles, sweat glands, sebaceous glands and nails. They are all related and act together as an entire system to realize the full function of skin.

Sweat gland is one of the major cutaneous appendages, the principal function is thermoregulation during exposure to a hot environment or under physiological stress. They distribute widely all over the body and the daily insensible water loss for a standardised individual (surface area 1.8 m^2) is from 0.6 to 2.3 liters, this number is even higher depending upon the level and type of stimulation [126]. However, hyperhidrosis, or excessive sweating, is a condition characterized by increased perspiration, in excess of that required for regulation of body temperature. It can be generalized or limited to some anatomic area such as axilla, palms, soles, scalp or face. Commonly, for personal hygiene and aesthetic purpose, many people prefer to control excessive sweating, especially in the axilla region. Therefore, sweat glands as well as their secretions, become one of the main targets of cosmetic compositions such as deodorants or antiperspirants.

Various techniques have been explored over years to monitor sweat activities. Older techniques include starch-iodine paper [127], plastic imprint, collection of sweat accumu-

lated under mineral oil [128]. Recent techniques include infrared thermography imaging [129], direct video monitoring [130], optical coherence tomography [9,131] and colorimetric mapping using hydrochromic polymers [132]. However, most of these techniques (except OCT) are not suitable to measure instantaneous sweating, indeed in the case of mental and physical stress, sweat gland have been shown to discharge sweat in pulsative fashion [133]. Single-sweat-gland activity (SSGA) has been monitored continuously at the skin surface using dedicated chamber and electrical conductivity measurement [134]. Nevertheless, the method measures the electrolyte secretion rate that is not the real sweat rate. Furthermore it provides no information about the sweat pore inner morphology.

In this chapter, we take here a different approach and explore, for the first time, *in vivo* human single sweat gland morphology and activity as well as antiperspirant activity using nonlinear imaging. (1) Two photon excited fluorescence (TPEF) microscopy is used to study an individual sweat pore inner morphology *in vivo* in 3D; (2) Coherent anti-Stokes Raman scattering (CARS) microscopy is applied to monitor SSGA with oil covering the skin surface, detailed sweating process and sweating rate are explored. Additionally, 2 types of antiperspirant salts, *in situ* Calcium Carbonate (*is*CC) and aluminium chlorohydrate (ACH), are studied in terms of SSGA. Their distribution inside sweat pore and the change of sweating volume or rate are observed to evaluate the antiperspirant activity properly.

3.1 Human Sweat glands

Sweating, as a thermoregulation process of the body, is one of the most important functions of the skin. The regulation of human body temperature is crucial for survival: protein denaturation and cell death can happen when the body temperatures is above 40 °C, which can finally lead to multiple organ failure [135]. Sweat is produced in sweat glands, long tubes tipped with a coiled ball at their base which are located mostly in the dermis, and moves toward the surface of the skin. Sweat glands and their biology have been studied anatomically and physiologically, mostly by histological approaches [127], however, few literature has been published on the mechanism of sweat process because *in vivo* observation is required.

3.1.1 Introduction

In humans, there are 2 main types of sweat glands: eccrine glands and apocrine glands, they are distinct from one another structurally, developmentally and functionally. This classification of sweat glands was first introduced in 1922 by Schiefferdecker [136] and referred in most of the literatures. Besides, Sato *et al.* [137] described in 1987 another type of sweat gland: apoeccrine gland, which is a mixed type gland that possesses certain morphologic and functional features of eccrine and apocrine glands. They found such glands develop from eccrine glands with age and are only located in the axillae region. Nevertheless, most recently, Bovell *et al.* in 2007 doubted the existence of apoeccrine sweat glands and they demonstrated that no evidence of apoeccine glands was found by histology or by immunofluorescence [138]. In this chapter, we introduced the 2 types of sweat glands defined by Schiefferdecker [136] and widely accepted by the community.

Eccrine and apocrine sweat glands already exist on human body at birth but apocrine sweat gland does not become active until stimulated by hormonal changes in puberty. Eccrine sweat glands distribute almost all over human body whereas apocrine sweat glands are restricted only to hairy body areas such as axillae, anogenital region and periumbilical region, which are related with their different morphologies (see Fig. 3.1). Eccrine sweat gland has a secretory coil (500 - 700 μm in outer diameter) that is located in the lower dermis and subcutaneous tissue. The long and thin eccrine duct ($<$ 3 mm in length [139], 10 - 20 μm in inner diameter and 50 - 80 μm in outer diameter [135]) passes through the dermis. The acrosyringium is the continuation of eccrine duct in the epidermis layer and becomes wider at the end on the skin surface, which is the opening of eccrine gland to the environment [140]. Compared with eccrine sweat glands, the apocrine gland coil is bigger ($\sim$ 800 μm in outer diameter) and locates deeper in skin than eccrine coil; the apocrine gland duct is a bit wider but much shorter than eccrine gland duct, it opens into the upper portion of the follicular canal [135] to connect with the environment.

The perspiration is caused by both thermal (high temperature) and emotional stimuli (such as anxiety, fear, pain or sexual arousal). Thermoregulatory sweating involves eccrine sweat glands and it occurs over the whole body surface, whereas emotional sweating involves both eccrine and apocrine sweat glands, it can occur over the body surface as thermal sweating but most evident on palms, soles and in axillary region [140].

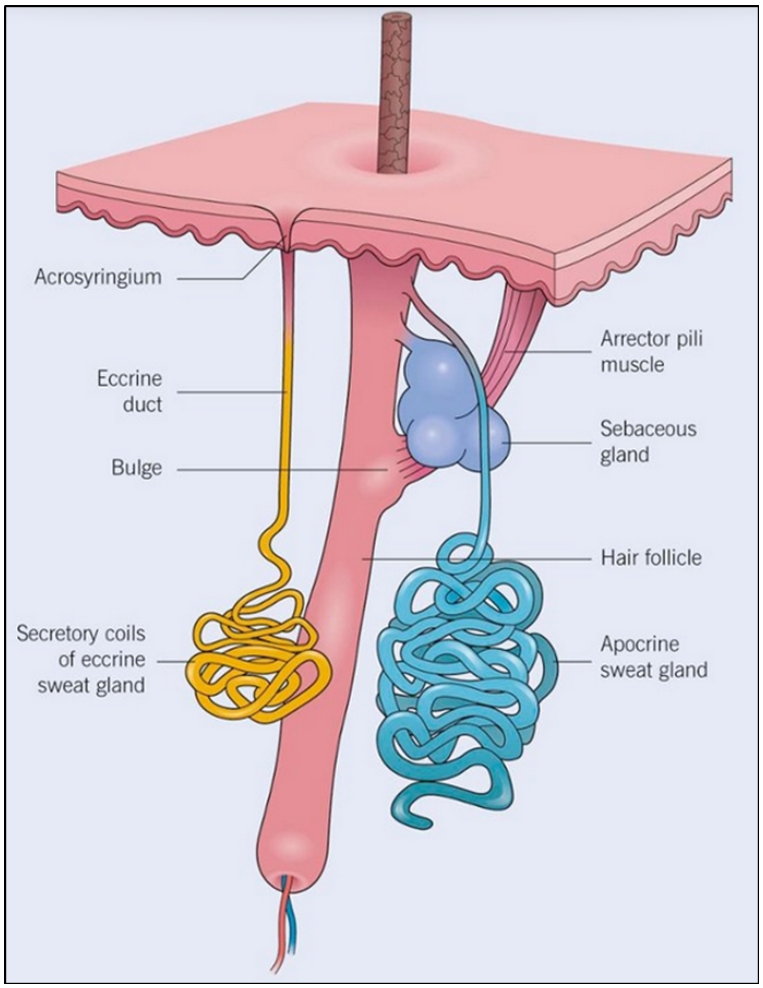

Figure 3.1: Diagram of eccrine sweat glands and apocrine sweat glands morphologies [140]. Eccrine sweat gland is constituted of 3 parts: secretory coils that is located in lower dermis and subcutaneous tissue; eccrine duct which is a thin and long tube passing through dermis; and acrosyringium which is located in the epidermis and opens to skin surface. Apocrine sweat gland has a bigger secretory coils and a very short duct, which opens to the upper portion of the hair follicular canal.

Most of our daily water loss are contributed from eccrine sweat glands, the secretion is primarily water with sodium chloride (NaCl), potassium and bicarbonate, which makes clear and colorless sweat. Apocrine sweat glands continuously secrete very small quantities of an oily fluid. This sweat is sterile, odorless and viscous, with a pH between 5.0 and 6.5. It is rich in precursors of odoriferous substances (cholesterol, triglycerides, fatty acids, cholesterol esters, squalene) and also contains androgens, carbohydrates, ammonia and ferric iron [140].

Table 3.1: Comparison of eccrine and apocrine sweat glands

	Eccrine glands	Apocrine glands
Localization	Almost entire skin surface	Axillae, anogenital, mammary areolae, ear canals, eyelids
Number	1.5 - 4 million	100 000
Secretory coil	small ($\sim$ 600 μm in diameter)	big ($\sim$ 800 μm in diameter)
Duct	long and thin	short and wide
Duct opening	ducts open onto skin surface	ducts open into upper portion of hair follicle
Secretion amount	large amounts (1 - 3 L/day)	very small amounts
Secretion appearance	clear, colorless, low viscosity	turbid and viscid
Secretion chemistry	primarily water with NaCl	lipids, carbohydrates, iron
Function	Thermoregulatory sweating and emotional sweating	Emotional sweating (especially hormonal)

The detailed comparison of eccrine and apocrine sweat glands are listed in Table 3.1 [135, 140]. The work reported in this manuscript focuses on eccrine sweat gland, which opens to skin surface and contributes for most of the daily water secretion, thus, it can be observed directly and easily from skin surface and it is an important target of antiperspirants.

3.1.2 Eccrine sweat glands

Eccrine sweat glands (1.5 - 4 million) can be found almost over the whole body surface (with only 2 exceptions: lips and glans penis [141]) and function through out the life. Despite the numerous works reporting eccrine sweat pore density on human body, divergences remain quite severe [126,135] whatever the physical or chemical methods used. For instance, Sato *et al.* got the lowest density on human back (64 sweat glands/cm^2) [141] while Talor *et al.* reported it twice higher (132 sweat glands/cm^2) [126]. This controversy may be due to the different techniques used for its determination and the age, gender, even personal dependence, as well as the consideration of anatomical eccrine sweat glands or active glands. Nevertheless, according to the literature, most of the studies agree that, the average density on the whole body surface is around 200 sweat glands/cm^2 anatomically, and the highest density can be found on the palms and soles (500 - 700 sweat glands/cm^2), yet 5% to 10% of them are inactive [126,135,141]; Note that this percentage is not affected by the environment nor stimulation [9,127].

Eccrine sweat gland can be generally considered into three parts: secretory coil, eccrine duct and acrosyringium.

The secretory coils of eccrine sweat glands, which are coiled tubular systems, are typically about 3.5 mm long, approximately 30 - 40 μm in inner diameter and 60 - 120 μm in outer diameter, have a volume close to 0.004 mm^3. The tubule of secretory coil is lined with a single cell layer organized as epithelial cells surrounded by discontinuous myoepithelial cells. The myoepithelial cells provide the structural support that permit the generation of the hydrostatic pressures required to overcome downstream friction and to open the duct pore; whereas the epithelial cells, including clear and dark epithelial cells, produce the primary sweat [126,140].

The eccrine duct is a thin and long tubule with a relatively straight form (compared with the spiral form when the duct travels through the epidermis) which traverses through dermis. It is in total less than 3 mm in length, 10 - 20 μm in inner diameter and 50 - 80 μm in outer diameter [135]. The ductal epithelium is composed of two or more layers of cuboidal cells. The eccrine duct is responsible for the reabsorption of sodium, chloride and water from primary sweat to generate the final sweat, at the same time, the diameter of duct distends with the accumulation of sweat and shrink with water reabsorption [9].

The acrosyringium is the continuation of eccrine duct and the intraepidermal portion of the duct, the lower acrosyringium travels though the epidermis with a spiral shape whereas the upper acrosyringium opens at the end to skin surface, which is generally known as ductal pores or sweat pores. The lower portion of the acrosyringium is surrounded by 2 layers of cuboidal epithelial cells which is similar than eccrine duct and the sweat pore is surrounded by keratinised cells with no clear distinction or border to the stratum corneum [126]. They can be identified over most of the skin surface with its funnel-like appearance and an inner diameter of about 60 - 80 μm [142].

3.1.3 Eccrine sweat glands distribution on palm

In this chapter, the human palm is chosen to be the experimental area for the observation of morphology of sweat duct and sweating process, as well as the evaluation of antiperspirants. This area is reported to have a very high density of eccrine sweat glands (500 - 700 sweat glands/cm^2), and is very sensitive to thermal or physical stress.

The localization of sweat pores is found to be relative to skin creases and ridges: On the hairy skin the pores usually open where creases converge whereas on the palms and the soles the pores open at the ridges [141] as it is showed in Fig. 3.2. The sweat glands are very well organized close to each other along the ridges lines (Fig. 3.2c) on human palm. This makes their finding simpler. Most importantly, on palm, the acrosyringium is closer to skin surface (see Fig. 3.2d), which is an advantage for optical microscopy.

The following sections focus on the imaging of palm, where we use two-photon excited fluorescence (TPEF) and coherent anti-Stokes Raman scattering (CARS) microscopy to observe individual eccrine sweat ducts *in vivo* in 3D as well as the occurrence of sweat events on skin surface.

3.2 Eccrine sweat gland morphology *in vivo*

Eccrine duct structure was observed histologically and the spiral shape in epidermis was reported [143], but dynamic study of sweat pross remains questionable and difficult since

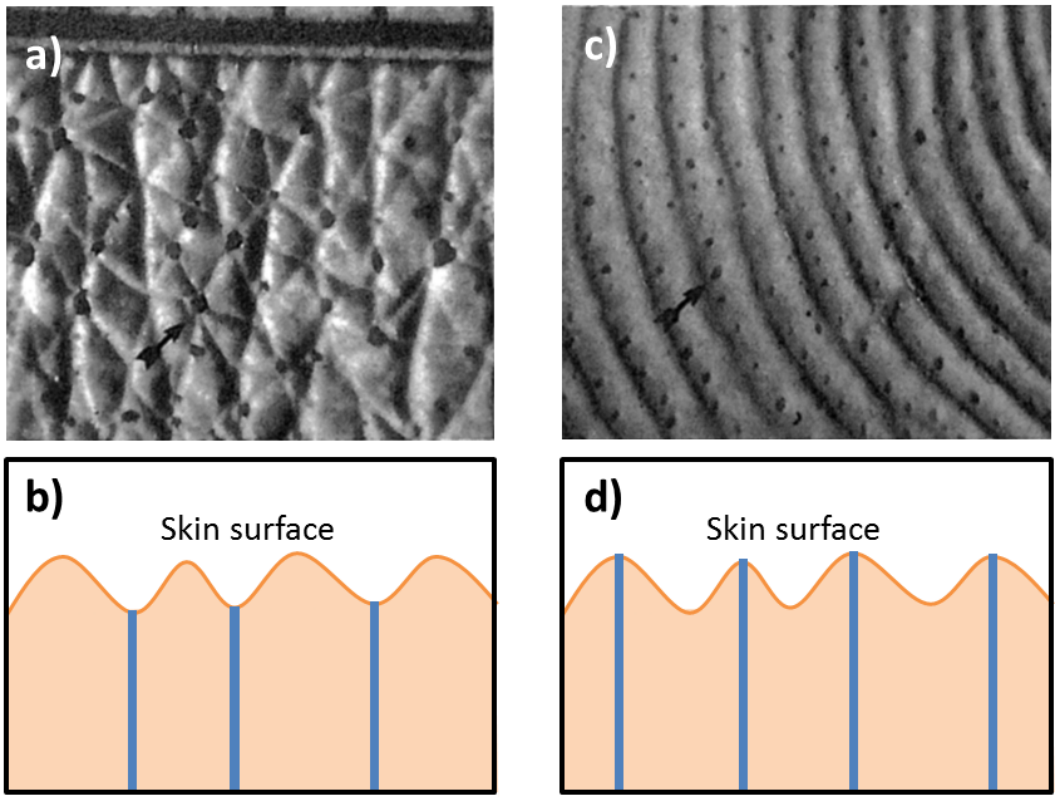

Figure 3.2: Localization of sweat pores on hairy skin and on palm. (a) The sweat pores are located where creases converge in hairy skin (see arrow), clear diagram of cross section is showed in (b); (c) The sweat pores open at the creases ridges on human palm (see arrow) and are very well organized along the grain lines, the diagram of cross section is showed in (d). Image adapted from [141].

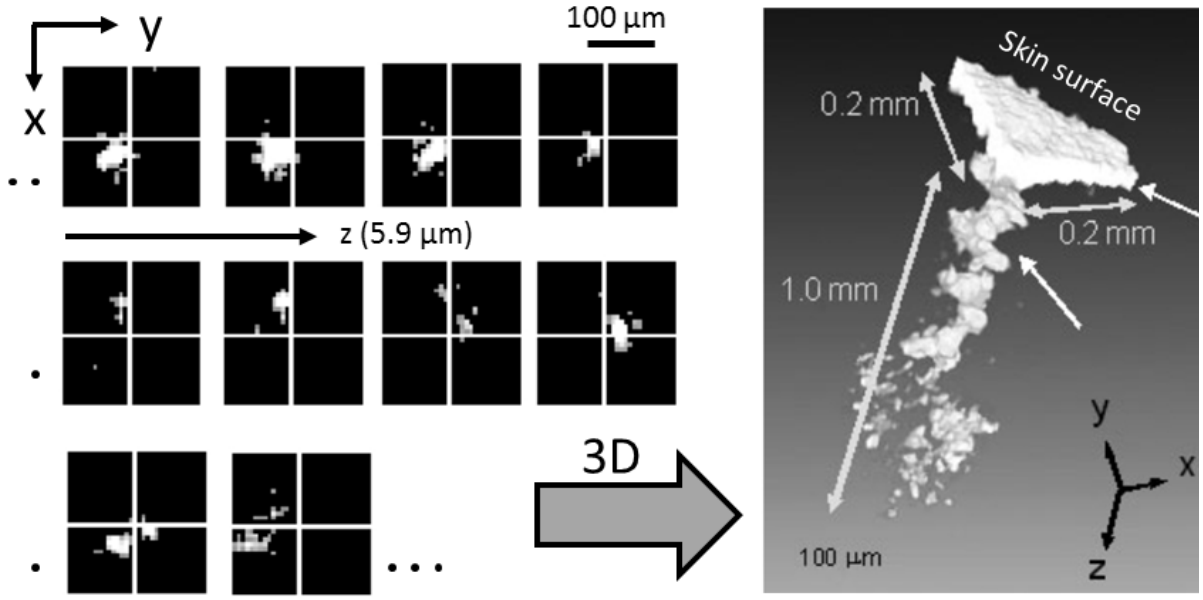

Figure 3.3: Optical coherence tomography (OCT) was used to image the spiral lumen in stratum corneum of epidermis in 3D by measuring the reflectance from water inside sweat duct. Resolution: 12.5 μm in X-Y plane and 5.9 μm in Z axis. Image adapted from [9].

the functionality is lost *in vitro*. In recent years, more *in vivo* investigations of eccrine duct have been reported, for instance, optical coherence tomography (OCT) has been used to observe mental sweating of a group of sweat glands on a human fingertip [9]. The spiral lumen in stratum corneum is imaged up to 1 mm depth from skin surface and the relation between mental stimuli and sweating events are studied. However, OCT is limited by its resolution (12.5 μm in X-Y plane and 5.9 μm in Z axis in the study of Ohmi *et al.* [9]) to provide detailed information of sweating (see Fig. 3.3).

To get more insight into single-sweat-gland activity (SSGA), a high-resolution and non-invasive imaging technique, which also allow imaging in depth in thick biology tissue, is required. Moreover, the technique should be fast enough to follow sweating process in real-time.

3.2.1 Intrinsic fluorophores

Intrinsic fuorophores present in biological tissues allow the imaging of native structures without introducing artificial compounds as it is explained in Chapter 2 (Section 2.2.1). The eccrine duct is a tubule with normally 2 layers of epithelial cells as the tubular wall and it is located in epidermis. We concentrate in this work in human palm where the epidermis has a quite thick SC (0.8 - 1.4 mm [84]). Using TPEF and CARS microscopies, the maximum depth reachable is $\sim$ 150 μm and the eccrine duct is always located in a quite homogeneous environment within this depth on palm. Besides, the eccrine duct lumen, where the sweat locates, does not give autofluorescence.

Therefore, three parts should be visible when using TPEF contrast: (1) the epidermis acts as a homogeneous background, (2) the eccrine duct walls (two layers of epithelial cells) are highlighted, and (3) sweat, which is primarily water, inside eccrine shows as a dark area.

3.2.2 Imaging single sweat pore *in vivo* by TPEF microscopy

Two-photon excited fluorescence (TPEF) microscopy permits high-resolution and non-invasive imaging in thick tissue. In our experimental setup, the maximum imaging depth in skin is 150 μm with the near-infrared excitation laser; each image takes 0.3s - 0.5s (depending on image quality required) using a homemade fast galvanometric mirror scanning technique. Thus, we can not only understand the detail structure of sweat pore and eccrine duct but also follow the sweating process in real-time *in vivo*.

Figure 3.4 shows the modified microscope for *in vivo* application. Based on the home-built optical setup introduced in Chapter 1, we adapted it for *in vivo* imaging (see Fig. 3.4a), where special holders were developed to fix arm and hand during experiments. First we choose a relatively flatter area on the palm to be investigated (Fig. 3.4a); then the hand is securely fixed on a homemade hand holder with adhesive tape; a necessary coverslip is lying between the skin surface and the holder (Fig. 3.4b). The hand together with its holder is then fixed on the microscope stage with magnet (Fig. 3.4c). The excitation laser is coming from a water objective (Olympus 40$\times$) and the back reflected signal is collected by the same objective in Epi-detection, A scheme of the experiment is depicted

in Fig. 3.4d.

With this *in vivo* adapted setup, we can observe a single sweat pore from the skin surface. The excitation laser wavelength is 735 nm, and the maximum power we use *in vivo* is $\sim$ 30 mW. The sweat duct can be distinguished up to a depth of 150 μm from the skin surface (in these conditions).

Figure. 3.5 shows the TPEF imaging process of an individual sweat duct. An area is chosen on human palm to be imaged (Fig. 3.5a), a stack of X-Y plane images are taken from skin surface up to the depth of 150 μm, with a z-step of 1 μm. As expected, the dark eccrine duct lumen and bright borders are visualized from the homogeneous epidermis background (Fig. 3.5b). In the upper part of acrosyringium segment (Fig. 3.5b, 0 μm and 10 μm), there is no clear distinction or border between keratinised cells surrounding the duct and stratum corneum; On the contrary, in the lower part of acrosyringium segment (Fig. 3.5b, 26 μm - 100 μm), the two layers of epithelial cells are clearly highlighted. Obviously, the contrast is getting weaker with increased depth because of the loss of both excitation and detection efficiency (Fig. 3.5b, $>$ 100 μm). Only a weak fluorescence from epidermis can be collected at a depth of 150 μm. Figure 3.5c is a X-Z cut of the image stacks, where the funnel-like sweat pore at skin surface and the spiral lumen of eccrine duct in epidermis are visible.

3.2.3 3D morphology of sweat pore

To build a 3D model of sweat gland from TPEF images (Fig. 3.5) requires further image processing that we shall describe now.

Image segmentation

To represent the morphology of sweat duct, we choose the inner lumen of eccrine duct, which is the dark area inside the bright epithelial cell walls. This option is valid for two cases: (1) in the acrosyringium segment where the background is relatively homogeneous and (2) in the duct segment where the bright border is visible.

Most of thresholding methods that are commonly used for medical image segmentation (whether region-based method or edge-based method), have difficulties to remove multiple

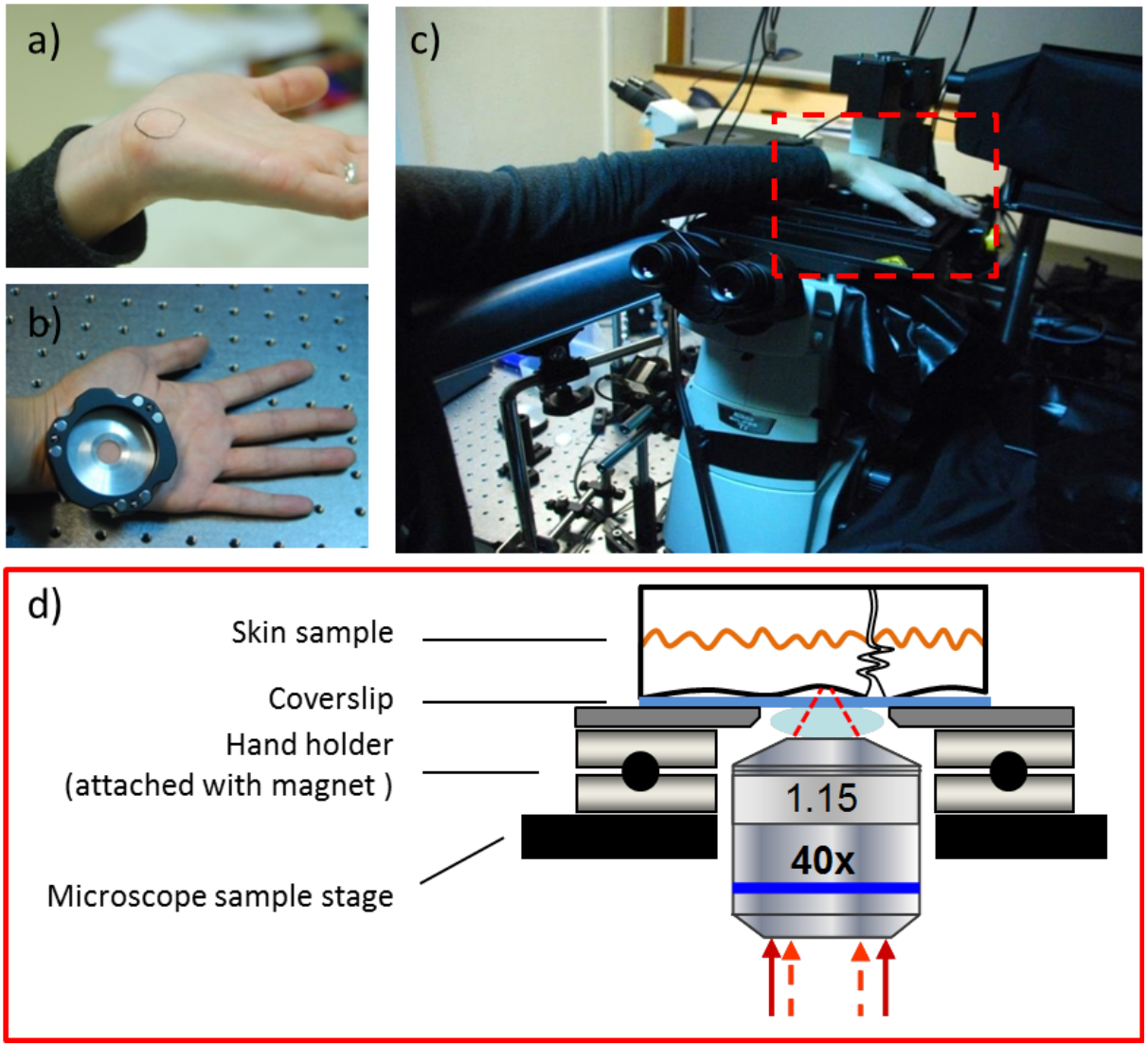

Figure 3.4: Home-built setup for imaging human hand *in vivo*. (a) Experimental area selected on human hand. (b) The hand is fixed to the hand holder with a coverslip between them. (c) The arm is fixed on an arm holder whereas the hand is kept immobile with the hand holder attached to the microscope sample stage with magnet; (d) To image a sweat pore, excitation laser is sent from a Olympus 40× water objective and the back reflected signal is collected by the same objective.

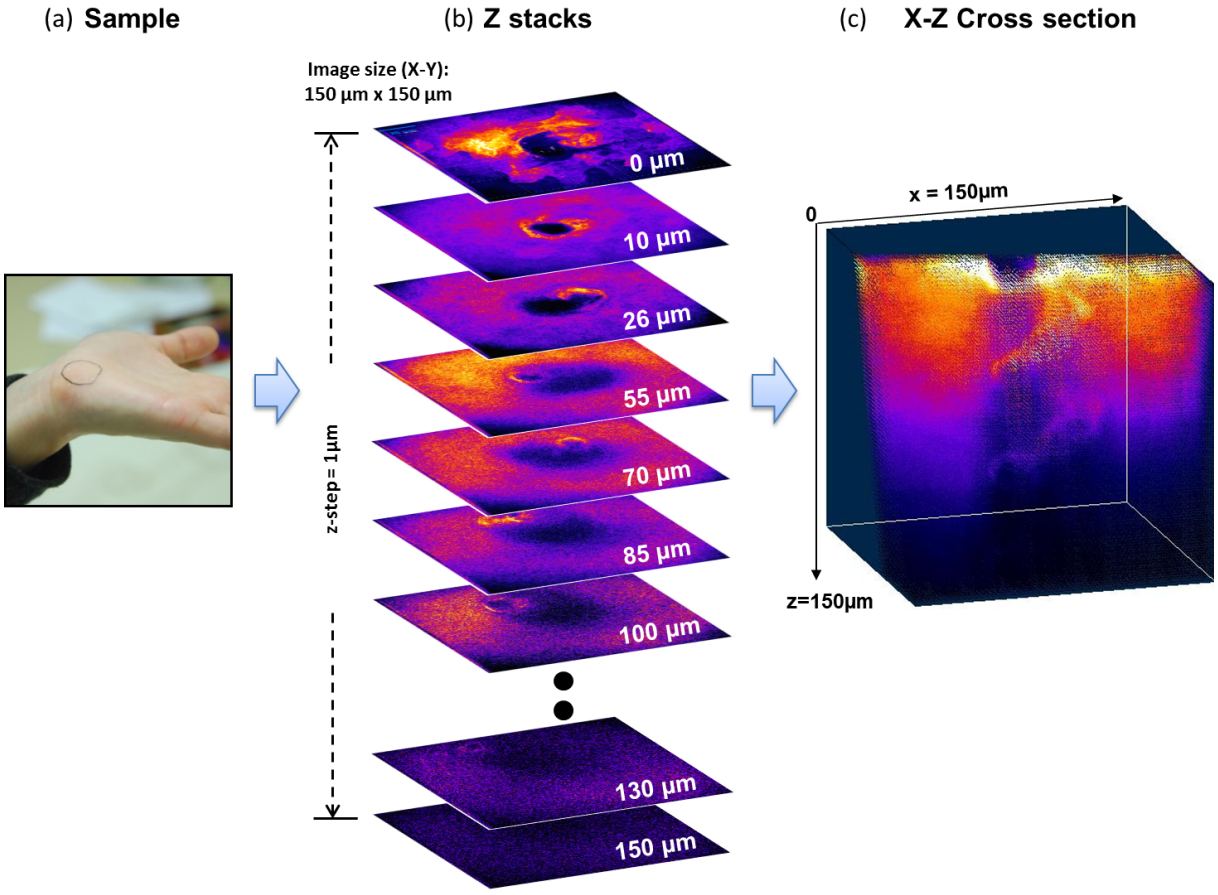

Figure 3.5: An individual sweat duct *in vivo*. (a) Experimental area selected on human hand. (b) Z-stacks of TPEF images from skin surface up to a depth of 150 μm with a z-step of 1 μm, X-Y image size is 150 μm $\times$ 150 μm (250 $\times$ 250 pixels). Strong autofluorescence can be seen from the sweat duct wall, homogeneous fluorescence surrounding the sweat duct is from Epidermis, and the lumen inside sweat duct appears dark as filled with air or water. (c) X-Z cross section where the spiral lumen of sweat duct is clearly visible.

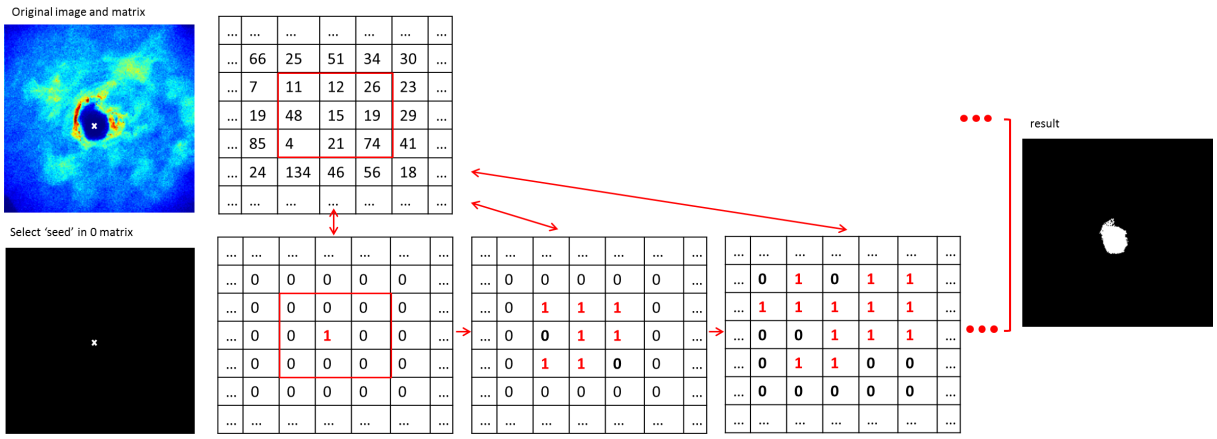

Figure 3.6: An example of "region growing method". "Seed" point is selected manually in the original image and the neighboring pixels are in a window of 3 × 3 pixels, the corresponding position of "seed" in 0 matrix becomes "1"; when neighboring pixels in original image agree with the conditions (see text), the corresponding position in 0 matrix becomes "1" and it becomes the new "seed", otherwise it keeps "0"; the "1" region keeps growing until there is no neighboring pixels fulfilling the conditions.

and/or unexpected background automatically. This is especially true in our case where images show low-contrast with a background evolving with depth. Thus, we have chosen a more controlled semiautomatic image segmentation method named "region growing method".

The "region growing method" is looking for groups of pixels with similar intensity staring from a pixel or a group of pixels selected (called "seed"). Then the neighboring pixels are examined with a condition on intensity to decide whether they will be removed or added to the growing region. The object is finally represented by all pixels that have been accepted during the growing procedure [144]. Figure 3.6 showes an example of semiautomatic region growing method applied on our experimental image. The original image is a 250 × 250 pixels matrix with different intensities on each pixel, there is another corresponding 250 × 250 pixels matrix with only 0 intensity. The "seed" is firstly selected manually from the original matrix within the dark region that we expected to be eccrine duct lumen, then the same position of the 0 matrix becomes "1"; the neighboring pixels (within a window of 3 × 3 pixels) in the original matrix are examined, when it is in accordance with the conditions (see below), the corresponding position in 0 matrix becomes "1"

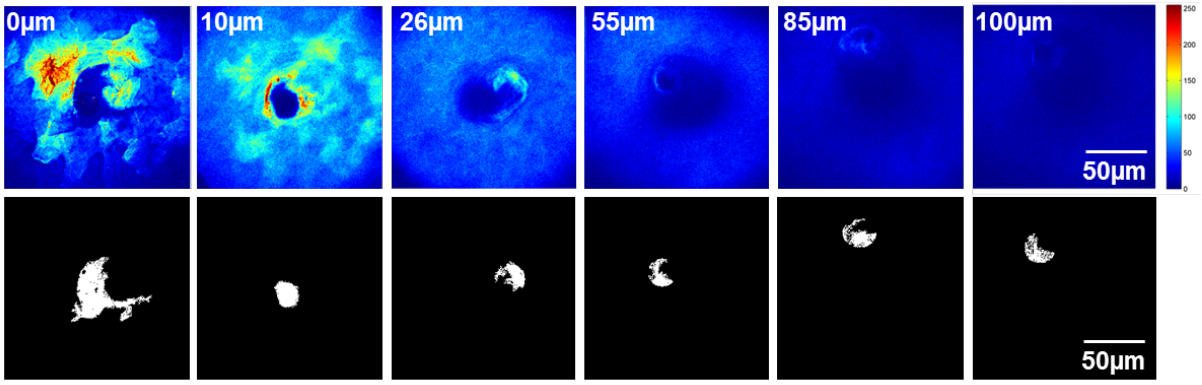

Figure 3.7: Two-photon excited fluorescence (TPEF) z-stacks images of one sweat pore and the segmentation results.

and this pixel is added to the growing region, otherwise it keeps "0". The new "1" position becomes "seed" automatically and its neighboring pixels are examined in the next step. The "1" region keeps growing until there is no neighboring pixels in accordance with the condition. The final segmentation is represented by all pixels with intensity "1" as showed in Fig. 3.6.

To select only the dark region inside eccrine duct lumen, we set multiple conditions: (1) in the acrosyringium segment, the difference of intensity between neighboring pixel and "seed" is within 10 - 15 (manually chosen but it means the same for all z-stacks); (2) in the duct segment, the neighboring pixel is within a distance of 40 pixels (equal to 24 μm, which is bigger than the normal inner diameter of a eccrine duct) to the original "seed"; the intensity of neighboring pixel is less than the mean of the whole original image; the difference of intensity between neighboring pixel and "seed" is within 10 - 15 (the same as (1)). With this method, the dark region that represents the duct lumen is selected from the two-photon native autofluorescence coming from sweat pore borders and epidermis. When it is applied on all z-stacks images, the "seed" is manually selected for each X-Y image (see Fig. 3.7), but the condition for neighboring pixel remains the same.

3D model

The 3D model of sweat pore at skin surface and the eccrine duct in epidermis can be built by the images after segmentation (see Fig. 3.8), the funnel-like appearance of acrosyringium and the spiral shape of sweat duct in epidermis can be clearly distinguished

up to the depth of 100 μm.

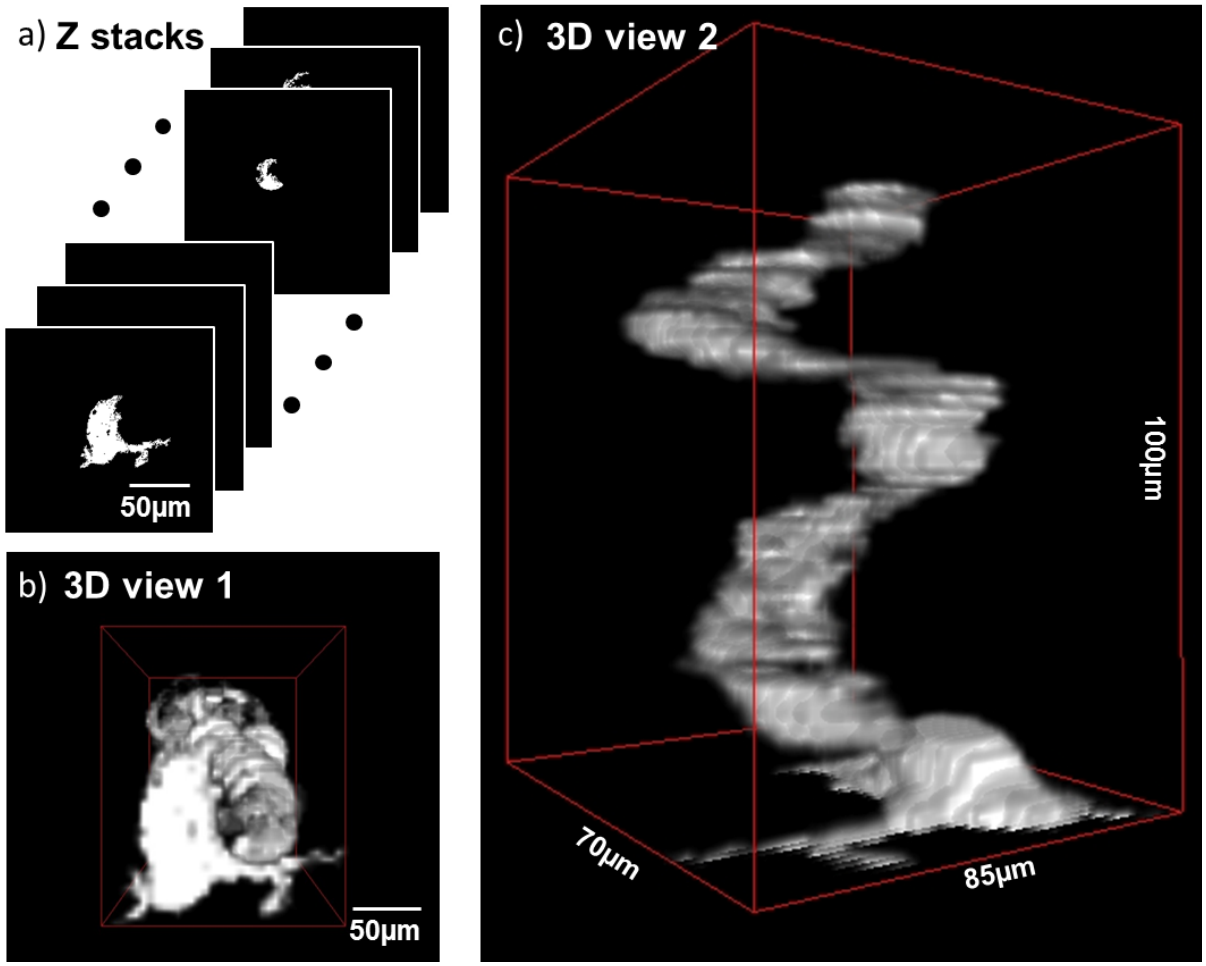

Figure 3.8: 3D model of eccrine duct. (a) Z-stacks segmentation images of eccrine duct from surface to 100 μm depth. (b) Bottom view of sweat gland 3D model. (c) Side view of sweat gland 3D model.

3.3 Imaging and quantification of sweating process

Vibrational imaging techniques such as coherent anti-Stokes Raman scattering (CARS) have chemical sensitivity and have proved to exhibit excellent label free contrast mechanism suitable for fast imaging. However, the secretion of eccrine sweat gland is mostly water, which is difficult to image on *in vivo* skin. The reason is that the interface between skin and coverslip is immediately filled by sweat water. It is therefore difficult to distinguish the water secreted by a single sweat pore, from the water accumulated between skin and coverslip, and resolving from previous secretion events. We have then devised an original method making use of oil that have the property of not be dissolved in water.

3.3.1 Method

The method of observing discharged sweat droplets on skin covered with oil was first devised by Jürgensen in 1924 [145]; he observed sweat drops in the colored oil under light microscope. Then in 1936, Ichihashi improved this method to photograph the sweat drops by observing the sweat droplets attached on a glass plate beneath the oil layer [128]. However, they observed only the discharged sweat drops when it went out of sweat pores and fell on the coverslip but not the sweating flow. This type of approaches are still very useful, but more as a simple and practical method for measuring the total amount of sweating in a selected skin area [146].

Moreover, the appearance of sweat drops is considerably influenced by the properties of the oil. With a relatively fresh oil of low viscosity, sweat drops change their forms quickly in variable manners, often enlargement and contraction alternate; while with thick oil, the change is very slowly and only a gradual increase or decrease in size is observed [128]. In this work, since we are interested to the brief event corresponding to single sweat pore secretion, a thick oil (olive oil) is considered to be a proper solution.

To observe sweat droplets in oil *in vivo*, first we modify the hand holder on the microscope sample stage by adding a spacer of 0.5 mm thick between the skin sample and the coverslip to create a "pool" of oil, but notice that the focus plane is still on the skin surface (see Fig. 3.9).

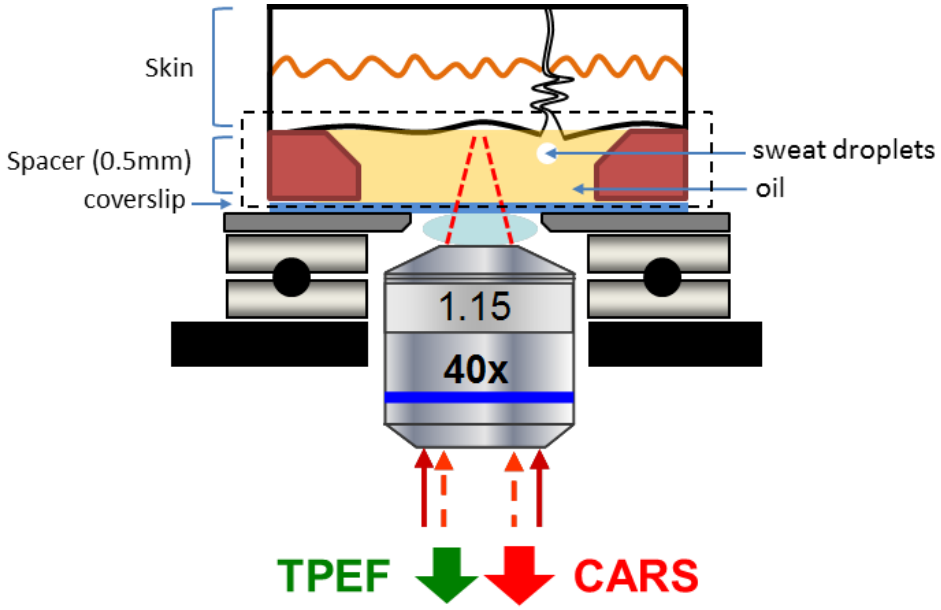

Figure 3.9: Imaging sweat droplets in oil. A spacer of 0.5mm thick is added between skin and coverslip to create a oil layer (inside dashed square), notice that in the experiment, the focus plane is still on the skin surface.

To achieve the strongest contrast we target the vibrational resonance of lipid at 2845 cm^{-1}. The excitation pump beam is set at 735 nm whereas the Stokes beam is set at 929 nm, the anti-Stokes signal is then generated at 608 nm. At the same time, skin tissue is excited mostly by pump beam and emits TPEF signal in the range of 400 - 600 nm. The maximum total power for the 2 laser beams at skin surface is 30 mW. With this, the maximum reachable depth shows to be 50 μm. The back-reflected TPEF signal from skin and the CARS signal from oil are both collected and measured in Epi-detection (see Fig. 3.10), images are scanned in X-Y plane (with a maximum field of view 300μm $\times$ 300μm); the objective can be controlled in the Z direction with z-step of 1 μm (within a maximum working range of 400 μm).

The morphology of acrosyringium in depth is shown in TPEF images (Fig. 3.10a) whereas the oil that fills the acrosyringium is showed in CARS images (Fig. 3.10b). We notice that oil can penetrate in a single sweat pore but only up to the depth of acrosyringium. During a sweat event, the oil is flushed out of the sweat pore as showed with CARS contrast in Fig. 3.10c: a dark area associated to the sweat droplet appears from

the bright background of oil. Therefore, when combining TPEF and CARS microscopies, the morphology of a single sweat duct together with its sweating flow can be observed at the same time and in 3 dimensions. In the following measurement, depending on the information required, X-Y plane (0.3s - 0.5s per image) and X-Z plane ($\sim$ 10s per image) are performed.

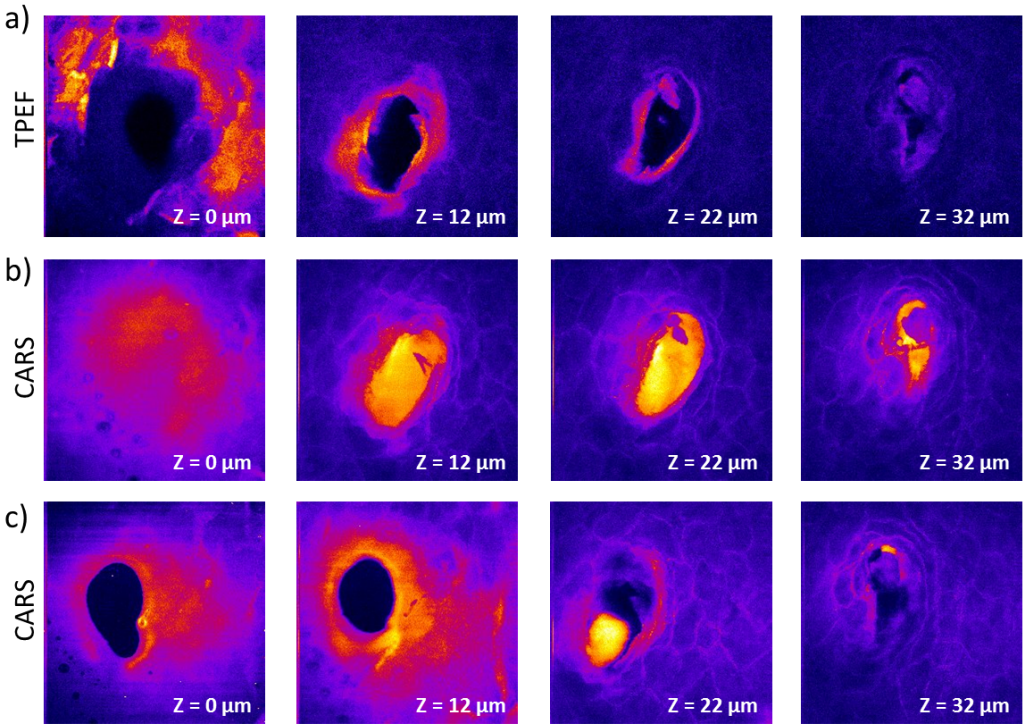

Figure 3.10: Imaging a single sweat pore (TPEF) and sweating process (CARS) in 3D. (a) TPEF: sweat pore morphology (100μm $\times$ 100μm) with increasing depth. (b) CARS: oil applied at skin surface penetrates inside a sweat pore (same depth as (a)). (c) CARS: when a sweat event happens, oil is flushed out of sweat pore: the black bubble associated to the sweat droplet is observed from a bright background of oil.

3.3.2 Surface imaging (X-Y plane)

In X-Y plane imaging, we focus on skin surface to observe the moment when a droplet just gets out of sweat pore. Figure 3.11 shows a single observation of an individual sweat pore during 10 minutes (following the arrow direction in Fig. 3.11a). First the oil slowly flows into the sweat pore (this is confirmed as well in X-Z plane imaging where the oil fills the whole acrosyrigium). After $\sim$ 40 seconds, the first droplet is secreted from the pore with a sudden ejection (within 3 seconds), when it reaches the skin surface, we observe a gradually increase of the sweat area during 20 - 30 seconds, this process can be understood as a combination of sweating and the droplet formation change in oil. The whole sweating process repeats continuously. When analyzing the image sequence, we could define a "relax time" and a "sweat time": "Relax time" is defined from the time when oil starts to flow into sweat pore and stays still inside, whereas "sweat time" is defined as the duration of water ejection (until the biggest water area is observed on skin surface). Clearly, in Fig. 3.11, there are two sweat events happening during the 10 minutes of observation, the "sweat time" is around 40 seconds, and between the two sweat events, the "relax time" is around 6 minutes. In the next subsection, more sweating events are quantified using the same method to estimate the average sweating rate.

3.3.3 Depth imaging (X-Z plane)

Besides, the sweating process can be also visualized in the X-Z plane (see Fig. 3.12). Compare with X-Y plane image, X-Z plane image takes longer time ($\sim$ 9 seconds per image) which is not enough to image the fastest sweat ejection ($<$ 3 s), nevertheless, we can observe the process of sweat accumulation inside acrosyringium as it is showed in Fig. 3.12. Oil fills the whole acrosyringium space at the beginning, then during the first $\sim$ 30 seconds corresponding to a sweat event, sweat was accumulating inside acrosyringium and the volume of oil is gradually decreasing. A thin oil layer is still visible on the surface at 32" (seconds) time, but disappears completely at 46" time when sweat is ejected out of acrosyringium. 1 min after, oil is found getting back to acrosyringium. In this observation, the "sweat time", as it is defined before, is around 37 seconds (from 00'32" to 01'09") which is in good agreement with the results coming from the X-Y plane observations. Additionally, from X-Z observation, we notice that there is a gradual process of water

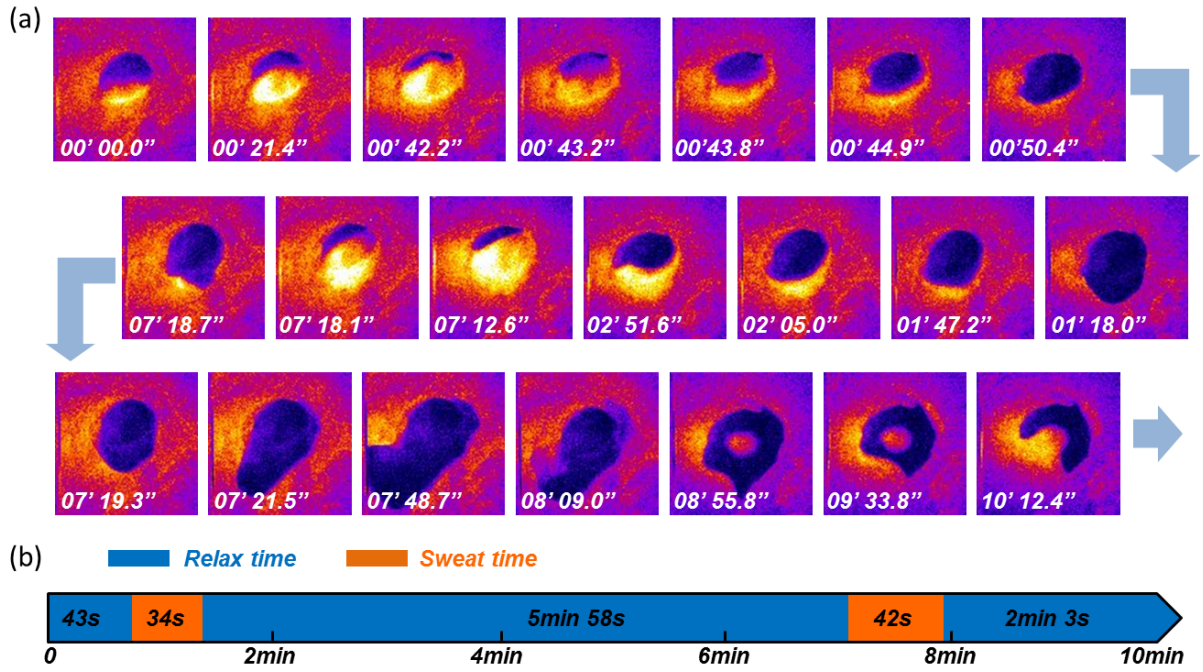

Figure 3.11: Sweating process of a single sweat pore on skin surface (X-Y plane). (a) Imaging sweating process continuously during 10 minutes, two sweat events happen in this observation. (b) Quantification of "relax time" and "sweat time" from a.

accumulation (from 00'0" to 00'32") before the sweat ejection (oil is flushed out of sweat pore) in this sweat event, which has never been reported before, we propose this process as "early stage sweat".

In human palm, where it is not oily skin, the "early stage sweat" can be cause by the artificial process: the sweat pore is filled by the topical applied oil. On the contrary, in the oily skin (such as human face and back), there is a possibility that the sweat pores are covered naturally by the oil secreted from skin itself. Therefore, the "early stage sweat" process that has been observed in this work, has to be further proved if it is a natural process.

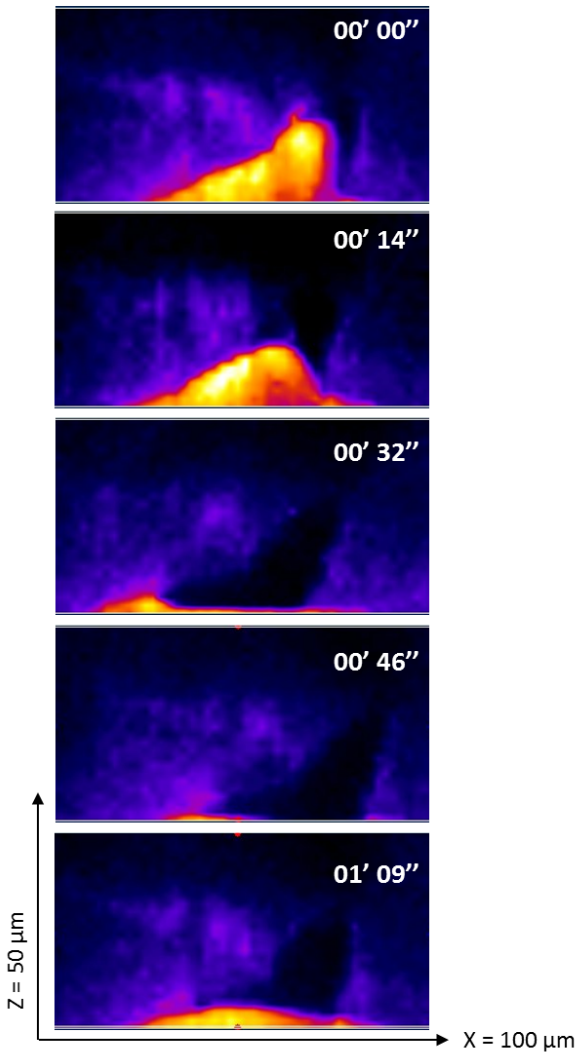

Figure 3.12: Imaging sweating process in X-Z plane. Gradual water accumulation inside the acrosyringium is during first 32 seconds until a thin oil film found on the sweat pore surface; the oil is ejected out of the sweat pore afterwards (to 46"); when the sweat event ends, the oil goes back again to the sweat pore gradually.

3.3.4 Quantification

Using both X-Y and X-Z observations planes, we want to quantify the average sweat rate and a single sweat droplet volume. The quantifications are based on the measurements from two volunteers: (1) Asian, female, 28 years old, and, (2) Caucasian, female, 28 years old. Since the sweating response are found quite differently in age, gender and race [147, 148], the quantification results in this study are proposed only for the young female group. The "spontaneous sweating", which is defined as normal neurogenic stimuli which cause perpetual "spontaneous" palmar-digital sweating [148], of eccrine sweat glands of the volunteers are measured (volunteers are not forbidden from daily activities such as drinking water or physical movement).

The sweat rate quantification is based on the "sweat time" and the "relax time" definitions, that can be calculated directly from X-Y imaging. We made statistics of "sweat time" and "relax time" (Fig. 3.13) with all the sweat pores and sweat events observed in this work ($\sim$ 10 sweat pores and $\sim$ 20 sweat events). Most of the "relax time" happened within a 2 - 4 minutes duration with an average duration of 2.9 minutes. The "sweat time" histogram is more dispersed from 0 to 50 seconds, yet the average sweat time is 30.5 seconds. According to this two parameters, the sweat rate of an individual sweat pore can be defined as the sum of the "sweat time" and the "relax time", which is 3.5 minutes in average. In other words, the sweat events happen every 3.5 minutes in average.

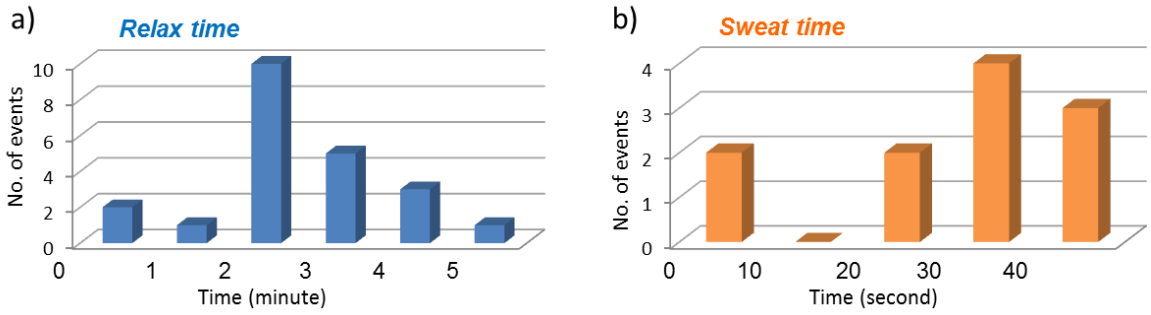

Figure 3.13: Sweat rate quantification. (a) "Relax time" histogram. (b) "Sweat time" histogram.

Besides, the volume of oil flushed out of sweat pore in a SSGA can be roughly calculated from the X-Z plane images with a simple model as showed in Fig. 3.14. A hemisphere

model is chosen according to the shape of acrosyringium, whose radius "R" can be obtained from X-Y plane surface images as showed in Fig. 3.14a (where the shape of oil is roughly a circle) and hight "h" can be obtained from X-Z image as showed in Fig. 3.14b. The average volume of oil flushed out of sweat pore in a sweat event is $\sim$ 20 pL, which represents the sweat volume in the early stage that cannot be observed on the skin surface.

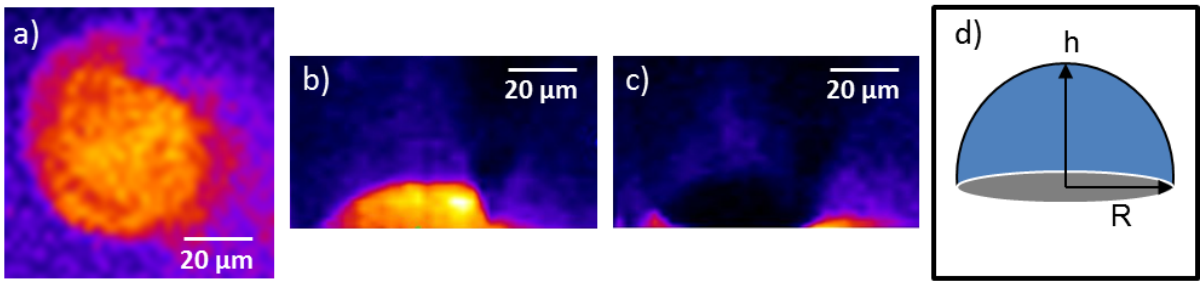

Figure 3.14: Quantification of sweat droplet volume. (a) The acrosyringium shape seen from the surface (X-Y plane). (b) Oil filled the whole sweat pore before sweating (X-Z plane). (c) Oil is flushed out when a sweat event happens. (d) a hemisphere model used in the early stage sweat volume quantification.

Few quantitative techniques were reported to test the sweat volume ejected from a single sweat gland but failed to investigate the dynamic process [127]. Even though, among those few reported studies there are still disputes. Provitera *et al.* reported that the sweat volume of a single gland is 4.7 $\pm$ 0.7 nL/min on the lower limb skin [149] whereas Lee *et al.* [150] considered this value is $\sim$ 1000 times bigger (9.45 $\pm$ 1.08 $\times$ 10^3 nL/min when assuming the density of sweat is $\sim$ 1kg/m^3) on the inner forearm skin. More recently, the dynamic process of sweat was presented by Ohmi *et al.* [9], they used optical coherence tomography to measure the reflection light intensity of the sweat pore which represents the amount of sweat passing the skin surface (sweat flux) (see Fig. 3.15).

Figure 3.15 presents the dynamic change during a sweat process. We found that there is actually a process of early stage sweat when the water is accumulated inside sweat pore, which is during $\sim$ 30s and with the volume of $\sim$ 20 pL. This process can be only discovered by observing the sweating process in 3D but not on the skin surface (Fig. 3.15a) [9]. Then there is a sudden ejection with high flux but during very short time ($<$ 3s) and a gradual decreased "tail" follows it until the end of the sweat process (as we discussed before), which is agree with the study by Ohmi *et al.* [9].

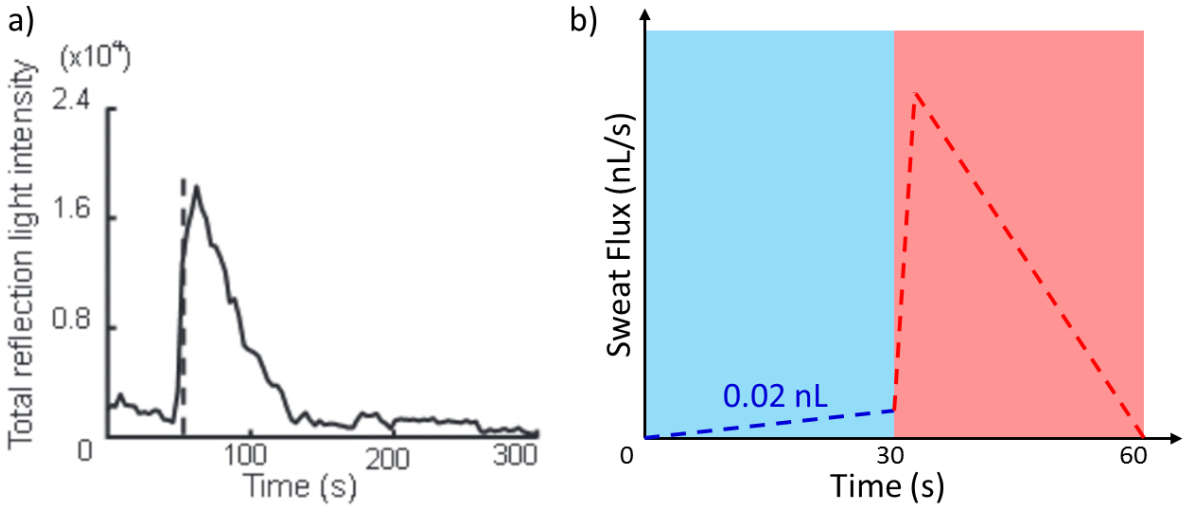

Figure 3.15: (a) Total reflection light intensity of the sweat pore by optical coherence tomography which represents the amount of sweat reaching the skin surface (sweat flux), image adapted from [9]. (b) Simulation of sweat flux from our study, blue area is the early stage sweat when the water is accumulated inside sweat pore (cannot be observed on the skin surface) whereas red area is the "sweat time" (as we defined before) during which the sweat flows out of sweat pore (can be observed on the skin surface).

3.4 Antiperspirant action

Despite the importance of thermoregulation, the notably increased perspiration under certain conditions such as physical exercises or emotional stress (for instance, nervous, fear or panic) is not pleasant. Thus, generally, for personal hygiene and aesthetic purpose in daily life, many people prefer to control excessive perspiration especially in the axilla region.

Antiperspirant, which is a commonly used cosmetic product, can prevent sweat from reaching the skin surface. This objective could be possibly achieved by physical (eccrine ducts are physically occluded by antiperspirant component), chemical (antiperspirant component can flocculant proteins in skin or sweat) or biological (antiperspirant component change the morphology or activity of sweat gland) methods [151].

The most widely used antiperspirant agents are topically applied aluminium salts such

as Aluminium Chlorohydrate (ACH). Their mechanisms of action have been studied for decades [151–153] since 1916 when aluminum chloride was introduced as an antiperspirant for the first time [154]. Beside, more recently, calcium salt or oxide is used to enhance the stability of the conventional antiperspirants [155, 156]. At the same time, the possible antiperspirant efficacy of calcium salt (such as calcium carbonate) was investigated as alternative antiperspirant salt [157]. However, up to now, all studies reporting antiperspirant salts localization in sweat ducts were performed by histological approaches requiring biopsies, an *in vivo* method is extremely needed to understand their localization and correlation with antiperspirant efficacy.

In this chapter, we described the first results obtained using non-invasive imaging techniques to investigate antiperspirant distribution in human sweat pore and antiperspirant efficacy *in vivo*. Two compounds are tested in this work: (1) *In situ* Calcium Carbonate (*is*CC), the penetration and distribution in sweat pore on human palm is directly observed in 3D by TPEF and CARS microscopies. The antiperspirant efficacy of *is*CC is measured clinically and independently; (2) Aluminium Chlorohydrate (ACH), the distribution is observed indirectly by a contrary contrast (see below) and a statistical method based on the change of SSGA is proposed to evaluate antiperspirant efficacy since ACH does not generate workable Raman signature.

3.4.1 Antiperspirant action of *is*CC

"*In situ* calcium carbonate" (*is*CC), which is formed *in situ* from the chemical reaction between solution of calcium chloride ($CaCl_2$, 0.5 M) and sodium bicarbonate ($NaHCO_3$, 0.5 M) (see Eq. 3.1), leads to crystal formation.

$$CaCl_2 + 2NaHCO_3 \longrightarrow 2NaCl + CaCO_3 + H_2O + CO_2 \tag{3.1}$$

The average size of $CaCO_3$ crystals formed from calcium chloride and sodium bicarbonate solutions are generally has diameter > 5 μm. Time-separated application of $CaCl_2$ and $NaHCO_3$ solutions was used to avoid the crystallization of $CaCO_3$ on the skin surface.

In this study, for antiperspirant efficacy investigation of *is*CC, the solution of calcium chloride (0.5 M) was applied first on human skin and sodium bicarbonate (0.5 M) was applied with 1h delay. This application regime allows $CaCl_2$ molecules penetrate into sweat duct, and the chemical reaction happens in depth when $NaHCO_3$ is applied. Additionally, longer delay time is not used because the concentration of $CaCl_2$ can be significantly decreased with time (few *is*CC crystals can be found even on the skin surface with 2h delay in the experiment). The contrary application ($NaHCO_3$ solution first and $CaCl_2$ solution after 1 h) is not used neither, because human skin surface is naturally in the acidic range (PH from 4.0 to 7.0) [158], $NaHCO_3$ can be decomposed in an acidic environment if it is applied first on the skin.

CARS microscopy was used to acquire high resolution three dimensional images after topical application of antiperspirant salts *is*CC on palmar region *in vivo*. The *is*CC crystal ($CaCO_3$) has a strong vibrational signature from carbonates due to its totally symmetric stretch (see Fig. 3.16).

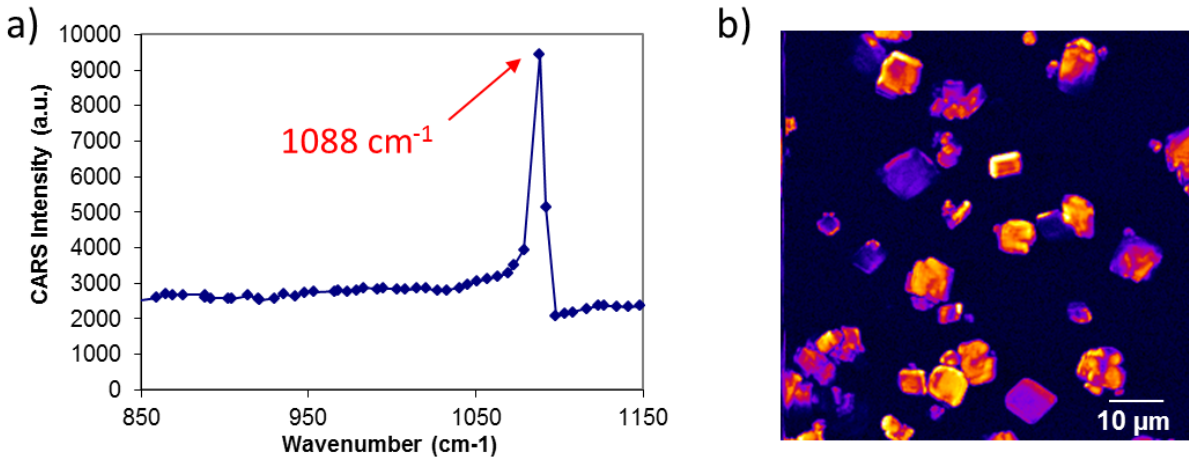

Figure 3.16: CARS spectrum and CARS on resonance image of $CaCO_3$ crystal (reacted from $CaCl_2$ and $NaHCO_3$ solutions). (a) CARS spectrum of $CaCO_3$, the strongest vibrational signature is found at 1088 cm^{-1} in CARS signal with good signal-to-noise ratio. (b) CARS image is taken at the resonance (= 1088 cm^{-1}), the $CaCO_3$ crystals are clearly visible.

We applied $CaCl_2$ solution on human palm first, and $NaHCO_3$ solution with 1h delay. TPEF microscopy was used to observe the morphology of sweat pore whereas

CARS microscopy was used to follow the distribution of *is*CC.

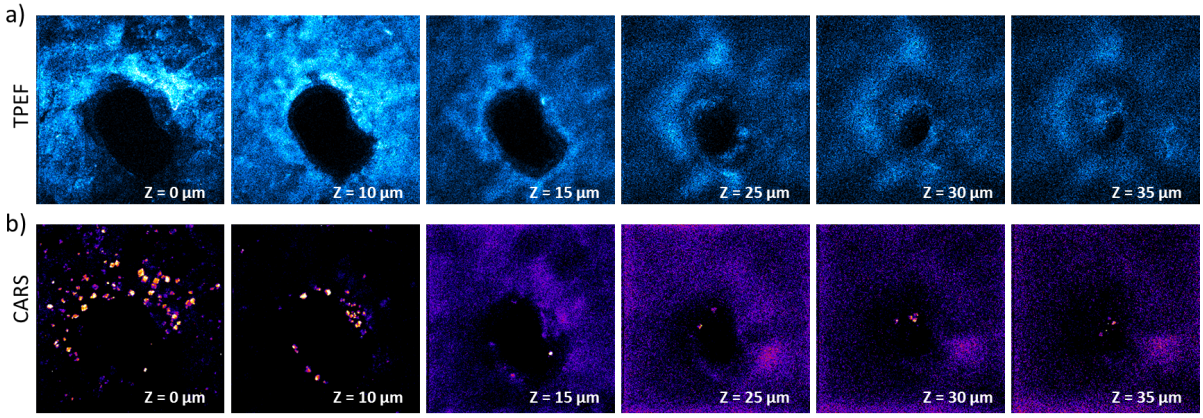

Figure 3.17: *Is*CC crystals distribution in sweat pore in depth (X-Y plane), image size = 100μm $\times$ 100μm. (a) TPEF images show the morphology of sweat pore (the acrosyringium segment) up to a depth of 35 μm. (b) CARS resonance images shows the distribution of *is*CC crystals at the same depth.

Figure 3.17 shows the X-Y images of sweat pore and the *is*CC crystals distributed inside. Plenty of the crystals are visible on the skin surface, with the depth, the crystals are found attached on the wall of sweat pore. Nevertheless, notice that at the end of the acrosyringium segment (30 μm & 35 μm) when the duct becomes very thin, a stack of crystals are located. This can be seen even more clearly in the X-Z image (Fig. 3.18).

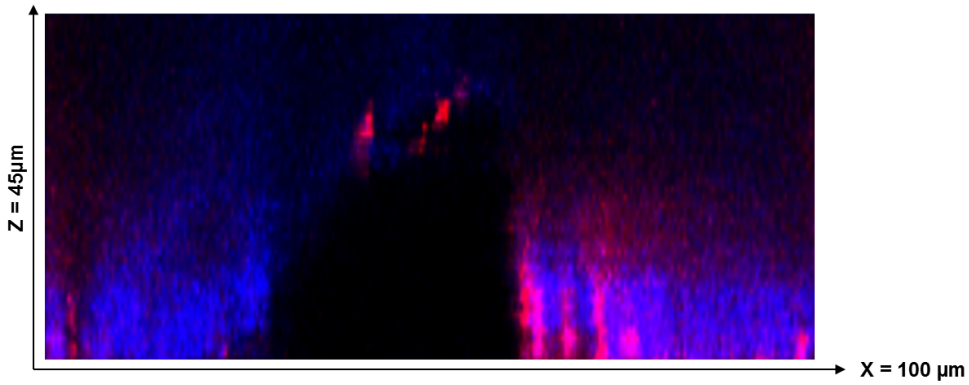

Figure 3.18: *Is*CC crystals distribution in sweat pore in depth (X-Z plane). A stack of crystals are clearly visible at the end of acrosyringium (TPEF: blue; CARS: fire).

To our knowledge this is the first time that CARS imaging technique is applied on

human skin for the purpose of exploring the distribution of products inside sweat pores *in vivo*. The penetration and distribution of *is*CC crystals can be followed up to a depth ~ 35 μm and they are found attached on the wall of sweat pore up to the beginning of the duct. Additionally, CARS signature represents the characteristic of molecules, in the other word, the crystal inside sweat pore is certainly constituted of $CaCO_3$ molecules. This is consistent with antiperspirant mechanism of *is*CC which involves crystals formed deep inside sweat pore.

The antiperspirant efficacy of *is*CC was also evaluated according to a standardized protocol [159] where a significant reduction of sweat of 29 to 42% is found on human back (L'Oréal unpublished results).

In conclusion, the *in situ* Calcium Carbonate (*is*CC) was investigated to explore its antiperspirant action: (1) An efficient time-separated application regime (calcium chloride is applied first and sodium bicarbonate is applied after one hour delay) is was used and proved experimentally. (2) We observed the penetration and distribution of *is*CC in sweat gland by treating the human palm with the application regime proposed in (1), the crystals can be found up to a depth of 35 μm attached on the wall of sweat pore especially at the junction of sweat pore and the duct. According to the CARS signature and crystal formations, this is consistent with the *is*CC antiperspirant mechanism.

3.4.2 Antiperspirant action of ACH

Aluminium Chlorohydrate (ACH) is generally believed to dissolve in the sweat on the skin surface and to some extents to diffuse down the sweat duct. The dissolved salts forms a gel *in situ* in the presence of proteins, creating a "plug" in the duct near the sweat pore, thus reducing the sweat flux reaching skin surface. Additional biological effects of aluminium salts on sweat production have also been described, such as ionic exchange blockage at the distal acrosyringium and structural changes of eccrine glands [151]. In a recent article, Yanagishita et al, clarified localization of Al in palmar skin after topical aluminium chloride treatment by histology. They confirmed the precipitation of an amorphous cast including keratin and polysaccharide in the sweat duct in the stratum corneum [160].

Unfortunately, there is no workable vibrational signature that can be obtained from

ACH molecules, we have failed to observe ACH penetration into sweat pore directly by CARS microscopy, however, the "oil" regime is used again to image the contrary contrast. We want to follow the sweat events in time and observe their changes by applying ACH, to evaluate its antiperspirant action statistically. During the observation period, we found also the "plug" formed by ACH and protein under certain application conditions.

Normal sweat without any treatment was measured first, the purpose was to measure the percentage of non-active sweat pores (non-active sweat pores / all sweat pores tested), this value was measured again after treatments to evaluate the impact of ACH. ACH was dissolved in two solutions for further treatments: water and cosmetic formulation (from L'Oréal). The two solutions (ACH/water of 15% by mass, and ACH/formulation of 15% by mass) were applied on selected regions on palm individually, and a group of sweat pores along a ridges line on human palm was observed during 5 minutes, the results are compared with the non-treated situation:

- No treatment
  - 36 sweat pores are tested and 7 of them are not active, the non-active percentage is 19% (7/36).
- 15% ACH/Water (mass) for one-time application
  - 2h after the treatment, a crystalised "film" appears and covers most of the sweat pores, 95% of the sweat pores are not active;
  - When we clean the skin surface with water, the ACH "film" disappears, sweat events happen again as in the "no treatment" case.
- 15% ACH/formulation (mass) with periodical applications (every 12h)
  - 24h after the treatment, 10% of the sweat pores are not active (3/31);
  - 36h after the treatment, small gel structures appeared on skin surface and in sweat pores, 29% of the sweat pores are not active (6/21);
  - 48h after the treatment, big gel structures were observed deep inside of sweat pores (see below), 89% of the sweat pores are not active (25/28).

The results of 3 conditions are listed above: (1) no treatment, (2) ACH/Water and (3) ACH/formulation. In condition (1), the non-active percentage of sweat glands is 19% in our experimental environment which is in agreement with literature [126], the results of the other two conditions (with treatment) are compared with it. In condition (2), when 15% ACH/Water was applied on human palm, the solution crystalised whin 30 minutes and a crystal "film" was visible on skin surface. Then we applied the oil on the skin surface and observe it with TPEF and CARS microscopy, square formation of crystals can be observed in the bright background from oil, it prevents the oil penetrate into sweat pore and no sweat event was found. Then we washed hand with water and repeat the same observation, the crystalized "film" was disappeared and the sweat events happen as in condition (1). Therefore, although sweat was prevented from reaching the skin surface by the "film" when ACH/Water was applied, this is not an efficient way to stop sweating in daily life because skin surface is often in contact (such as clothes) or cleaned frequently. To achieve antiperspirant purpose in the daily life, it is important to stop sweat deep inside of sweat pore.

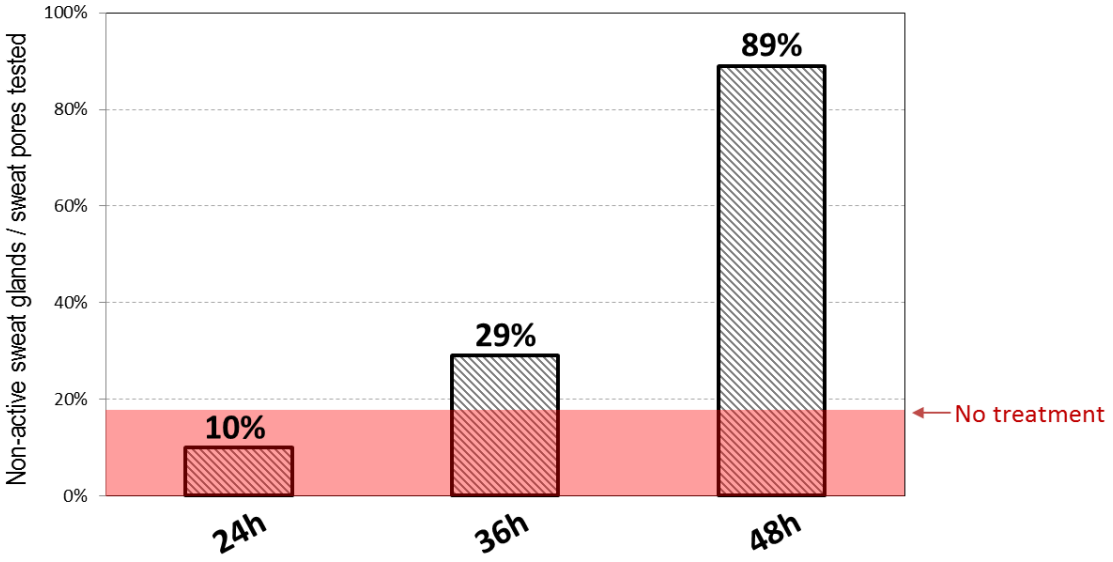

Figure 3.19: The percentage of non-active sweat pores increases with treatment time (15% ACH/formulation by mass, periodical applications). The red area is the level of non-active sweat pores without any treatment in our experimental condition.

In condition (3), 15% ACH/formulation was applied on palm periodically, any "film" was showed on the skin surface after the treatment. The sample was observed after 24

h, 36 h and 48 h, a clear increase of the percentage of non-active sweat glands with time, as shown in Fig. 3.19 (10% - 89%), compared with the non-treated skin ($\sim$ 19% of sweat pores are not active in our experimental condition). We believe that the increased percentage of non-active sweat pores (70% increase) is related to the antiperspirant action of ACH. This is consistent with reported sweat volume reduction from ACH (50% - 70% depending on ACH concentration) [152].

Furthermore, the impact of ACH (15% ACH/formulation) is observed as early as 36 hours treatment time (29% non-active sweat glands). It is known that aluminum salts can react with proteins from sweat or skin surface to gradually form a flocculant or gel [151, 160]. The floccular "plugs" grow with time and finally can block the sweat duct to achieve antiperspirant purpose. The reaction time depends on the *in situ* conditions such as sweat flow, protein concentration, PH and type of aluminum salt [161].

In Fig. 3.20, we show an example of "plugs" observed at sweat pore entrance after 48 h treatment by 15% ACH/formulation, suggesting that the "plugs" is big enough to block sweat duct. From the contrary contrast of "oil" regime, the acrosyringium morphology is visible from TPEF images (Fig. 3.20a) whereas the oil filled inside the sweat pore can be seen from CARS images (Fig. 3.20b). Oil distributed homogeneously on the skin surface (z = 0μm) and filled inside sweat pore in the deeper location (z = 14 μm). However, at Z = 20 μm, a gel structure appeared in the oil region up to Z depth = 35μm. The "plugs" structure and location can be seen more clearly in the X-Z and Y-Z plane images in Fig. 3.20c and Fig. 3.20d (inside red circle), it is amorphous in structure and located at the entrance of sweat pore and deep inside. Such "plugs" can thus block the sweat pores and prevent sweat from reaching the skin surface. The blockage may remain active in daily life because the "plugs" are located deep inside the sweat pore. To our knowledge, this is the first time that sweat pore plugging is observed *in vivo* using a non-invasive technique.

3.5 Conclusion

Nonlinear microscopy, including 2-photon excited fluorescence (TPEF) and coherent anti-Stokes Raman scattering (CARS), was used to study a single sweat gland activity (SSGA)

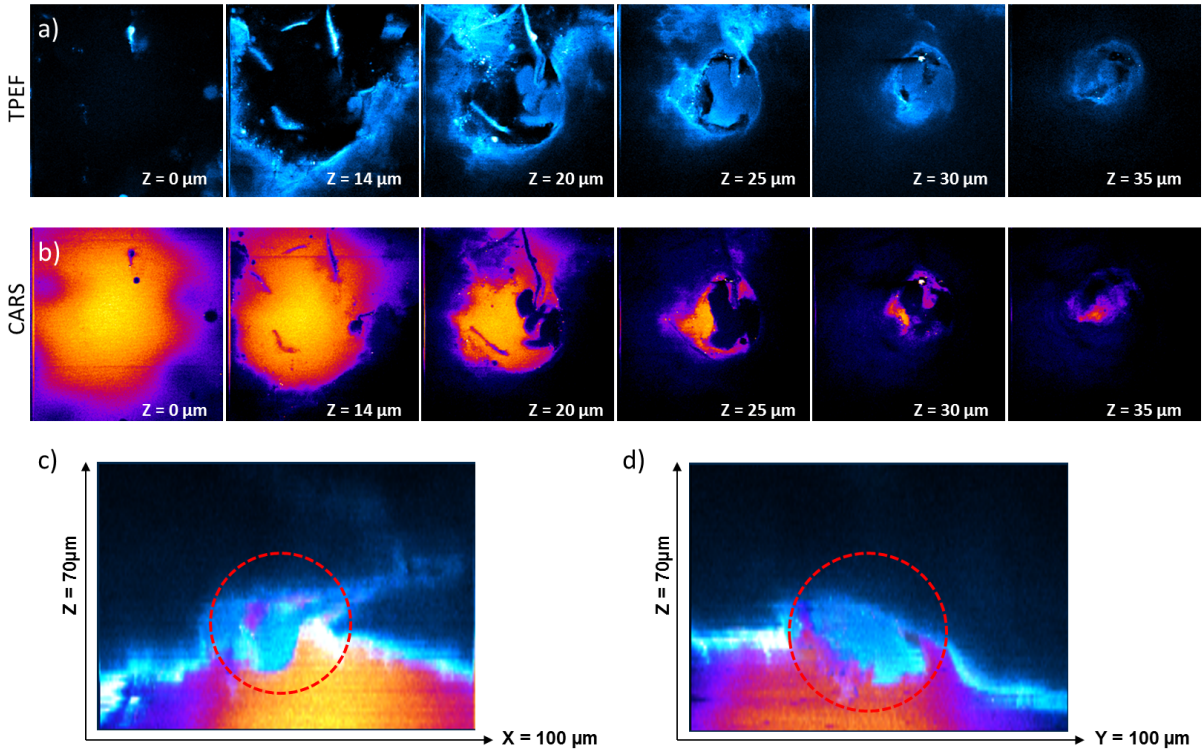

Figure 3.20: The gel structure ("plugs") found inside sweat pore after 48h treatment of 15% ACH/formulation which reflects the antiperspirant mechanism. (a) TPEF images show the morphology of sweat pore. (b) CARS images show the oil filled inside sweat pore, the gel formation can be seen from the bright background of oil with depth. X-Z plane (c) and Y-Z plane (d) images are obtained from X-Y stacks where the "plugs" are highlighted inside the red circle (TPEF: blue, CARS: fire).

in vivo. This non-invasive imaging method provides excellent high-resolution contrast in 3D in thick biological tissue. Together with fast scanning technique, the sweating flow can be observed in real-time as well as the sweat pore morphology. In this work we used (1) TPEF microscopy to map the sweat pore inner spiral lumen structure and (2) CARS microscopy to monitor SSGA. Additionally, with specific designed methods based on these two techniques, we also explored the localizations and activities of antiperspirant salts (*is*CC and ACH).

Firstly, the morphology of a single eccrine sweat pore on human palm was imaged by TPEF microscopy from skin surface to the depth of 150 μm (acrosyringium portion).

In the upper part of acrosyringium segment (up to $\sim$ 20 μm), the dark sweat pore is visible over the bright background because there is no clear distinction or border between keratinised cells of acrosyringium and stratum corneum. When it moves to the lower acrosyringium, the dark duct lumen and the highlighted epithelial cells layers surrounded are clearly showed over the homogeneous background coming from epidermis. A 3D view is reconstructed based on TPEF images where the funnel-like appearance of sweat pore and the spiral shape of sweat duct in epidermis can be clearly distinguished up to the depth of 100 μm.

Secondly, CARS microscopy was used to monitor sweating process in real-time with oil covered skin surface. Vibrational imaging techniques has the specific chemical selecting ability and has proved to exhibit excellent label free contrast mechanism suitable for fast imaging especially when tuned to the aliphatic C-H bond at $\sim$ 2850 cm^{-1} found in oils. We look for the sweat droplet formation and ejection, which appears in negative contrast over the bright oil "pool". The sweating process was observed in 3D in real-time, the "sweat time" and "relax time" were recorded to quantify the sweat rate whereas the volume of oil was calculated to estimate the volume of early stage sweat.

Thirdly, the *in situ* Calcium Carbonate (*is*CC) was investigated to explore its localization in sweat pore. The penetration and distribution of *is*CC in sweat pore was observed by CARS microscopy, the crystal formations were found up to a depth of 35 μm attached on the wall of sweat pore, especially accumulated at the junction of sweat pore and duct. Since the $CaCO_3$ molecules are confirmed by CARS signature, it is possible that the antiperspirant mechanism of *is*CC is partly based on physical process: the *in situ* formed crystals block the sweat pore at the place closing to eccrine duct and prevent sweat flux to reach the skin surface.

Finally, the Aluminum Chlorohydrate (ACH) was investigated by the "oil" regime (since ACH does not generate workable vibrational signature for CARS microscopy). 15% of ACH was dissolved in a commercial formulation (from L'Oréal), and applied on human palm periodically (every 12h), we monitored a group of sweat glands and compared the percentage of non-active sweat glands before and after certain application time (24h/36h/48h). The percentage of non-active sweat glands was found significantly higher when treatment time increases (10% - 89%) until 48 hours. In the observation after 48h treatment, the gel structures were found inside sweat pores at the end of sweat pore

closing to eccrine duct (at a depth of 35 μm). The location of those "plugs" is quite similar than *is*CC crystals, and they could block the sweat pores to achieve the antiperspirant purpose.

We applied successfully nonlinear microscopy for *in vivo* applications on human hand, monitored SSGA and antiperspirant activities, this study shines a new light on human *in vivo* research.

Chapter 4

Towards endoscope development for *in vivo* imaging

Nonlinear spectroscopy and microscopy open a door to video rate label-free imaging with applications in biology and medical science. In the preceeding chapters, we have applied two-photon excited fluorescence (TPEF) and coherent anti-Stokes Raman scattering (CARS) on skin research *ex vivo* and *in vivo*. However, reviewing most of the studies of skin using nonlinear imaging technique [18, 28, 29] as well as our work, it is apparent that there are two main limitations especially for *in vivo* application: (1) In scattering biological tissue, the image quality decreases with increasing imaging depth, and beyond a certain depth (typically 0.5 mm [162]) imaging is not feasible. Even in TPEF microscopy which is known for being very robust against image degradation due to scattering [163], the maximum depth that has been reported is only 1 mm [46]. (2) The clinical application of current state of the art nonlinear microscopes is limited, because of the lack of stability, compactness and flexibility of the optical system. Thus, there is a strong demand to integrate nonlinear imaging in a flexible endoscope for the minimally invasive clinical diagnostics and industrial applications.

In this chapter, in order to overcome the two limitations mentioned, we developed an "endoscope-like" system for the nonlinear imaging modes, TPEF, SHG, and CARS, by introducing a special type of hollow-core photonic crystal fiber - a kagomé fiber - as the delivery and collection fiber. This system was applied successfully for imaging

mice skin samples, which is the first step in the development of a nonlinear imaging endoscope. Additionally, several possible improvements based on this system are proposed for the future work to achieve a practical nonlinear endoscope for both multiphoton and vibrational imaging.

4.1 State of the art

Optical fibers, which transmit information over long distances at exceptionally high speed, are one of the major technological successes of the 20th century, covering broad areas such as telecommunications, sensor technology, spectroscopy and medicine. The light guiding mechanism of conventional optical fibers relies on the total internal reflection, a higher refractive index of the core compared to the surrounding media is required in such fibers [164]. However, since 1980s, the interest of researchers and engineers has been attracted by the ability of materials with structures on the scale of the optical wavelength, a fraction of a micrometer or less, in order to develop a new optical medium, known as a photonic crystal [165]. Photonic crystal fibers (PCFs), which is a new class of optical fibers, are designed with a solid or hollow core surrounded by the photonic crystal cladding that confines light to the core. One of the most important advantages offered by PCFs, compared to standard optical fibers, is the high design flexibility for controlling the bandgaps and optical properties. Since PCFs provide new and improved features, beyond what conventional optical fibers offer, they are finding an increasing number of applications in ever-widening areas of science and technology. Especially its application in the flexible endoscope is showing promise.

As demonstrated in this work, nonlinear imaging techniques have shown their powerful abilities for biological and chemical imaging. For this reason as well as the fact that nonlinear microscopes have limited imaging depth, many efforts are aimed at transferring nonlinear microscopy to endoscopy for label free, non-invasive deep tissue imaging. Endoscopic implementations of one-photon fluorescence and TPEF imaging [166], SHG [30], optical coherence tomography [31] and spontaneous Raman spectroscopy [32] have been reported numerous times in the literature. However, when it comes to CARS and SRS imaging, only very few examples of endoscopic implementations exist. The reason for this difference is that CARS and SRS involve two excitation pulses of different wave-

length in CARS and SRS processes, the fiber transmission range has to be broad enough; more difficultly, these two frequencies can interact with the fiber core and generate nonlinear signal which is difficult separate from the signal of the sample since they are of the same frequency. B.G. Saar *et al.* have developed an optical-fiber-delivered coherent Raman scattering (CRS) imaging system [35], where they delivered the excitation beams of CARS and SRS through the fiber, but the signal was detected directly in the forward direction instead of being collected by the fiber. On the other hand, the backward reflected CARS and SRS signal can be collected by using double-clad hollow-core fiber [36], however, the hollow-core fiber is normally suffered of narrow transmission range, the laser wavelengths can be tuned only in a very limited range, hence the vibrational resonance of biological tissue (generally in lipid range) cannot be achieved for efficient imaging. Z. Chen *et al.* reported recently that CARS together with TPEF and SHG can be performed simultaneously using fiber bundles, where the nonlinear signal generated in the fiber is removed before exciting the sample in this device [34]. Nevertheless, the signal has to be collected by another separate fiber in this system which increases the complexity.

4.2 Photonic crystal fibers

Photonic crystal fibers represent one of the most active research areas in the field of optics. These fibers and their properties appeal to applications by opening up the possibility of guiding light in a radically new way compared to conventional optical fibers [164]. Two types of PCFs - solid-core PCFs and hollow-core PCFs - are introduced in this section, among which, the kagomé fiber was chosen in this work for the development of the endoscopic system.

4.2.1 Solid-core and hollow-core PCFs

solid-core photonic crystal fibers (SC-PCFs)

In SC-PCFs, the core is made of silica while the photonic cladding is made of a lattice of air holes. The presence of low refractive index air holes in the cladding leads to a cladding with an average refractive index which is lower than that of the core. This gives rise to a

guiding mechanism called modified total internal reflection, which is quite similar to the guiding mechanism of standard optical fibers. According to recent reported results, solid-core PCFs have relatively low optical loss, which is typically 1dB/km with the improved fabrication process [165] and the lowest loss yet achieved is 0.15 dB/km [167]. For nonlinear imaging, an ultra-short pulsed laser source is normally required, these pulses would have to be delivered by the fiber in a nonlinear endoscope. The nonlinear interactions between ultra-short pump pulses and silica fibers have been previously reported [168,169], such as the pulse dispersion and four-wave mixing effect when two laser beams are delivered. The magnitude of these effects in SC-PCFs prevented the demonstration of CARS in endoscopes based on SC-PCFs [170], strong CARS signal is generated in the solid fiber core [171].

hollow-core photonic crystal fibers (HC-PCFs)

HC-PCFs are mostly fabricated from silica glass, it comprises a hollow core surrounded by a honeycomb lattice with a large air-filling fraction (typically $> 80\%$) [172]. Unlike SC-PCFs, HC-PCFs confine light not to a solid core but to a hollow core consisting only of air. The confinement relies on the presence of photonic bandgaps in the photonic crystal cladding. Thus this type of fiber can handle very high power because the hollow core has massively reduced nonlinearity compared to a solid core, which makes them attractive for high peak power laser pulse delivery [173]. Although theoretically the optical losses of HC-PCFs are lower than SC-PCFs since the majority of the light travels in the hollow core, in which scattering and absorption could be very low, the reported value are much higher because of limitations in the fabriation of HC-PCFs. Roberts et al. demonstrated that the transmission loss could be optimized to reach 0.1 dB/km in theory, the lowest loss in HC-PSFs (1.2 dB/km at 1600 nm) is still higher than SC-PCFs. The main drawback of these fibers is their intrinsically narrow transmission bandwidth determined by the bandgaps, the guiding bandwidth is usually around 15% of the central wavelength [165]. This excludes its implementation in a large number of applications in ultrafast nonlinear optics requiring broadband guidance or guidance in the visible and UV [174], and also excludes its application in a CARS or SRS endoscope.

Therefore, a fiber that can efficiently deliver two laser beams with different frequencies and high power, as well as collect the generated signal and return it back to the input side of the fiber for further analysis, is required for the realization of a nonlinear imaging

endoscope with CARS or SRS image contrast.

4.2.2 Kagomé fiber

The kagomé fiber is an alternative HC-PCF design which replaces the hexagonal lattice photonic cladding with a kagomé lattice [175, 176]. Indeed, the light propagates in an air core surrounded by an air / silica micro-structure, but this fiber does not have photonic bandgaps and the fiber-guided modes only weakly interact with the cladding modes due to the rapid phase modulation of the latter [174]. Due to this guiding mechanism, kagomé lattice HC-PCFs exhibit a broad transmission band covering the spectral range from the infrared up to the UV. Ghenuche *et al.* have taken advantage of the large transmission window of a kagomé fiber in Raman spectroscopy, where the excitation and the collected signal were transmitted through the same fiber [177]. It shows the potential of this fiber for collection of signal that covers a very broad spectral range.

The single-cell kagomé fiber (fiber code: 20090803#2) used in this work is from Russell Division, Max Planck Institute in Erlangen, it has been described in [172, 176]. Details of this fiber are shown in Fig. 4.1.

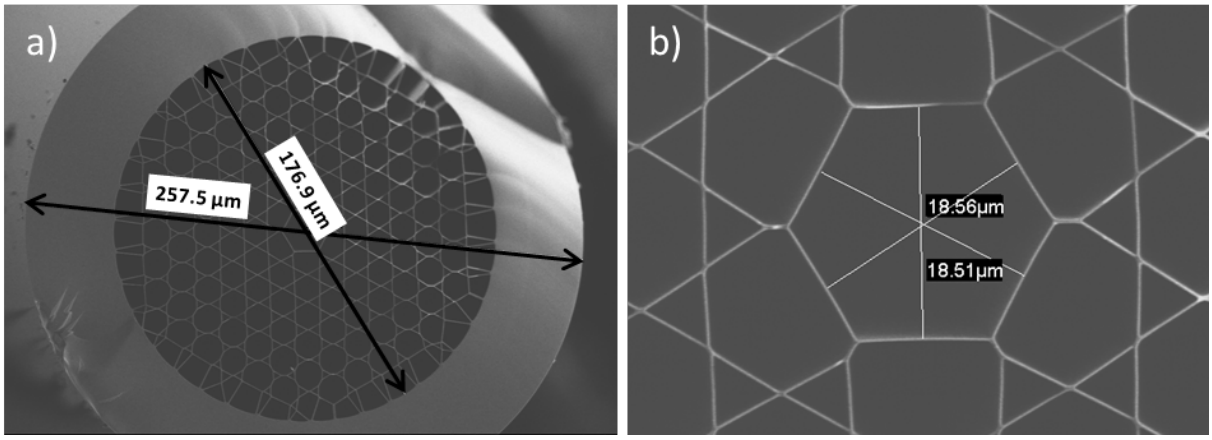

Figure 4.1: Electronic microscopic image of single-cell kagomé fiber. (a) The cross section of the fiber with the outer diameter $\sim$ 258 μm and inner diameter $\sim$ 178 μm. (b) The fiber core with an average diameter $\sim$ 18.5 μm.

4.3 Characterization of Kagomé fiber

We have characterized the propagation of light in a kagomé fiber. The laser source comprises a high-power tunable mode-locked Ti:Sapphire laser (Chameleon Ultra II, pulse duration 140 fs, repetion rate 80 MHz, tuning range 680 nm to 1080 nm) and a Chameleon Compact OPO-Vis (pumped by the Ti:Sapphire laser, tuning range 1000 nm to 1600 nm). The two laser beams generated from this system (for further four-wave mixing imaging) propagated through the kagomé fiber, and the output was observed.

First of all, we characterized the power handling capability of the fiber (see Fig. 4.2). With the increasing input power (up to $\sim$ 250 mW), the output spectra was not shifted or broaden spectrally, and no self-phase modulation was observed. Thus there is no nonlinear effect happened inside the fiber even with high power. For the maximum, the fiber can afford average input power more than 1 W, which is a very important property for nonlinear imaging.

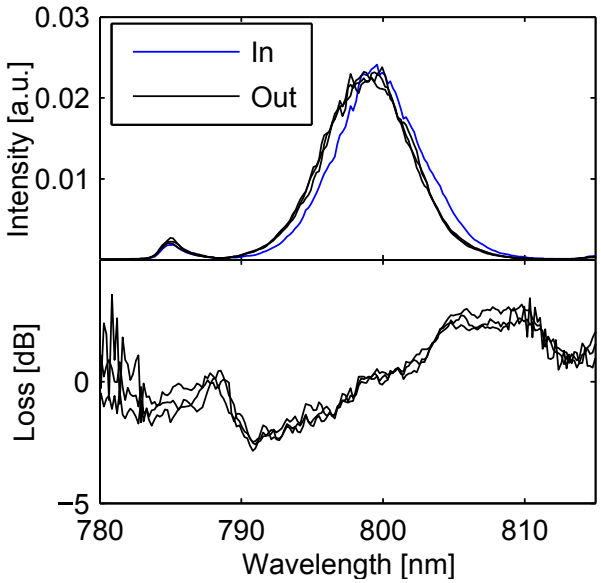

Figure 4.2: The output spectra with increasing input power. Top: Input and output spectra, output average power were 0.25, 4.56 and 31.87 mW (the length of fiber is $\sim$ 3 m, the transmission efficiency is $\sim$ 12%). Bottom: Relative loss in [dB] calculated from the input and output spectra.

Secondly, the effect of the kagomé fiber on pulse duration was measured. The pulse duration at different wavelength (from 750 nm to 1100 nm) was measured as input and output of fiber and they were found very similar (see Fig. 4.3a), the short laser pulses were delivered though the fiber almost without any dispersion.

More importantly, in order to generate CARS or SRS process, two laser beams are required, and we now confirm that the two pulses do not interact in the fiber. When the two beams of different wavelength (796 nm and 1005 nm) propagate through the fiber

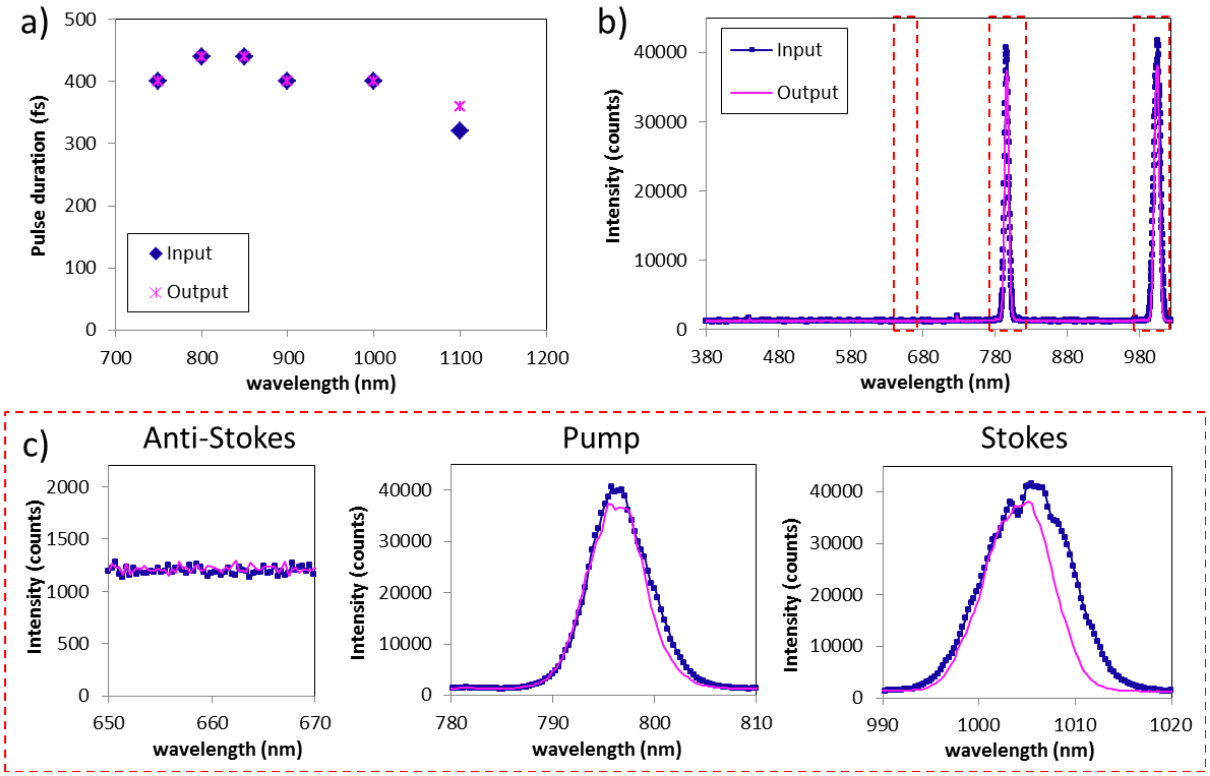

Figure 4.3: Untrashort laser pulse propagation in kagomé fiber. (a) Short pulse duration of different wavelength is measured at input and output of fiber, and it showed very similar time duration, which represents that the short pulse is not dispersed when it travels through this fiber. (b) Two beams (796 nm for pump and 1005 nm for Stokes) propagate through the fiber, the anti-Stokes signal supposes to be generated at 659 nm in CARS process. The magnified spectra of pump, Stokes and anti-Stokes region are shown in (c). The two input wavelength were not shifted and no anti-Stokes signal generated inside the fiber.

core simultaneously (see Fig. 4.3b), the input wavelengths are not shifted, and there is no four-wave mixing signal at the anti-stokes wavelength (659 nm) observed at the output of fiber (see Fig. 4.3c). Therefore, it is possible to deliver the high power ultrashort pulse laser beam through this fiber for further nonlinear imaging.

At last, we characterized the transmission range of the kagomé fiber. The transmission band (550 nm - 1000 nm and 1110nm) covers the near-infrared and visible range (see Fig. 4.4a). This transmission range can cover the wavelength of both excitation laser (in the possible operating range of the laser system) and emission signal for (1) TPEF (excitation: infrared, emission: 400 nn - 600 nm); (2) SHG (excitation: 1110 nm, emission

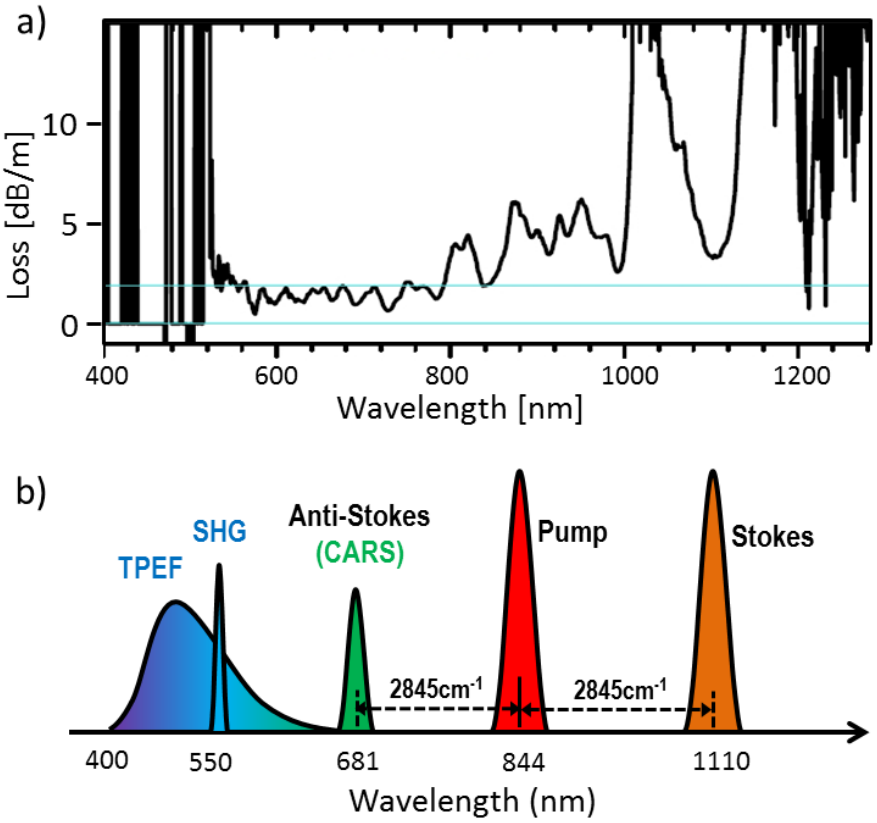

Figure 4.4: Corresponding to the spectral transmission range of kagomé fiber in (a) (manufacturer's specifications), the excitation wavelengths (844 nm for pump and 1110 nm for Stokes) are operated within the possible range of the laser system, and the emission signals are all within the transmission window of the fiber as shown in (b).

which doubles the excitation: 555 nm); (3) CARS in lipid range at 2845 cm^{-1} (excitation: pump = 844 nm, Stokes = 1110 nm, emission: anti-Stokes = 681 nm) (see Fig. 4.4b). Thus, the signal can be collected with the same fiber as the one that delivers the excitation laser beams to the sample.

However, the kagomé fiber exhibits higher losses than the other HC-PCFs (2 - 5 dB/m depending on the wavelength), thus even in the ideal condition, when the light passing through 1 m long fiber, the transmission efficiency will be 30% to 50%. In our configuration, the pump beam is operated at 844 nm with input power of 140 mW, the output power is 30 mW (21%) whereas Stokes beam is operated at 1110 nm with input power of 190 mW, the output powe is 35 mW (18%). This is almost the best condition that can be achieved in practice with our laser system.

In conclusion, the kagomé fiber has high power handling capability, broad spectral transmission window, and the ability of delivering short laser pulses without dispersion or nonlinear effects inside fiber core. These properties are well-suited for nonlinear, especially CARS and SRS, endoscope development.

4.4 “Endoscope-like” optical system

Figure 4.5 shows a schematic of the setup. With the laser source introduced before, the two beams from Ti:Sapphire laser and OPO are overlapped in time and space and sent into the kagomé fiber, the two beams are then delivered to a customized scanning microscope [36] and excite the sample by an NA=1.15 objective lens (Nikon APO LWD water 40 ×). The back reflected signal is collected by the same objective and then go to two different detection systems: (1) Epi-detection. The signal emitted by the sample is collected by the excitation objective, filtered by optical filters, and detected by one of three PMTs (Hamamatsu, R9110 Photomultiplier tube), which are available for TPEF/SHG/CARS imaging at the same time; (2) Endoscope-like detection. The signal travels back to the galvanometric mirrors and return to the same fiber, the signal is detected in the input side of kagomé fiber by an APD (avalanche photodiodes) running in photon counting regime.

In this system, pump beam (Ti:Sap) and Stokes (OPO) beam are operated for exciting

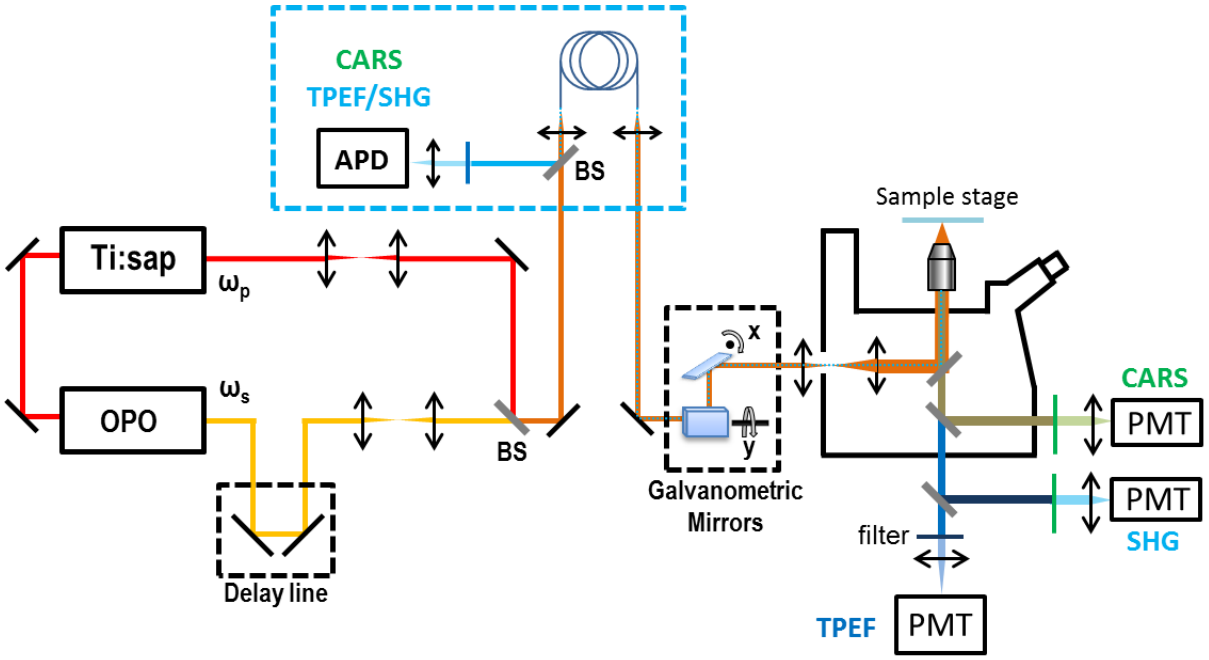

Figure 4.5: Nonlinear "endoscope-like" optical system. Ti:Sap: Ti:Sapphire laser (Chameleon Ultra IIOPO), OPO: optical parametric oscillator (Chameleon Compact OPO-Vis), BS: beamsplitter, PMT: photomultiplier tube, APD: avalanche photodiodes.

CARS signal in the lipid range (2845 cm^{-1}), at the same time, TPEF is mostly excited by pump beam while SHG is excited by Stokes beam. As demonstrated previously, the incident powers at the output side of the fiber are 30 mW for pump (844 nm) and 35 mW for Stokes (1110 nm), then, after passing through the galvanometric mirrors and objective, around 30% to 40% of the energy could arrive in the sample plane.

4.5 Nonlinear imaging (TPEF/SHG/CARS)

We will proceed to compare the two imaging modes (1) Epi-detection and (2) endoscope-like detection for a sample of mouse skin imaging. It remains difficult to image biological tissue, because the intrinsic signal from tissue is not as strong as chemicals, thus, even though TPEF [178] as well as CARS and SRS [179] imaging has been developed endoscopically and applied on imaging chemicals (polystyrene beads or organic crystal), they often failed to image tissue.

4.5.1 Mice melanoma samples

Mice skin sample is a cutaneous metastasis resected from mice with melanoma of the skin (Centre d'Immunologie de Marseille-Luminy, CIML). The sample was snap-frozen on dry ice soon after resection, and kept stored at - 80°C. The frozen tissues were embedded in O.C.T. Compound (Sakura Finetek, Zoeterwoude, the Netherlands), and sequential cryosections were cut with a Leica CM3050 cryostat, air-dried, and stored at - 80 °C until use. 7 μm thick tissue cross sections were mounted on standard 75×25×1 mm Superfrost Plus microscope slides (Thermo Scientific, Braunschweig, Germany).

4.5.2 Epi-detection

The laser beams were firstly delivered by kagomé fiber to the sample plane, the back reflected signal were collected in mode (1) Epi-detection, where TPEF/SHG/CARS signal can be obtained at the same time and selected by proper bandpass filters. A typical image acquired throughout this work is 100 μm × 100 μm (250 × 250 pixels), dwell time of 80 μs/pixel, accumulation of 20 times, the total acquisition time for a TPEF/SHG/CARS image is $\sim$ 100 s. This configuration is constant in Epi-detection and Endoscope-like detection.

Figure 4.6 shows the TPEF/SHG/CARS images obtained in Epi-detection. A region of the mouse skin sample closing to skin surface that was free from melanoma was imaged. The TPEF image shows the morphology of epidermis (bright border at the left-bottom) and dermis, the SHG image shows the collagen fibers distributed only in dermis and the CARS image shows the lipid content in the sample. The three contrasts were then merged where the clear distinction can be seen. The two beams are well delivered to the sample and performed good overlapping in plane and in space since CARS image is well obtained. The signal-to-noise ratio in those images from Epi-detection is $\sim$ 2000 with this configuration, which proves that the sample was efficiently excited by the fiber-delivered laser beams.

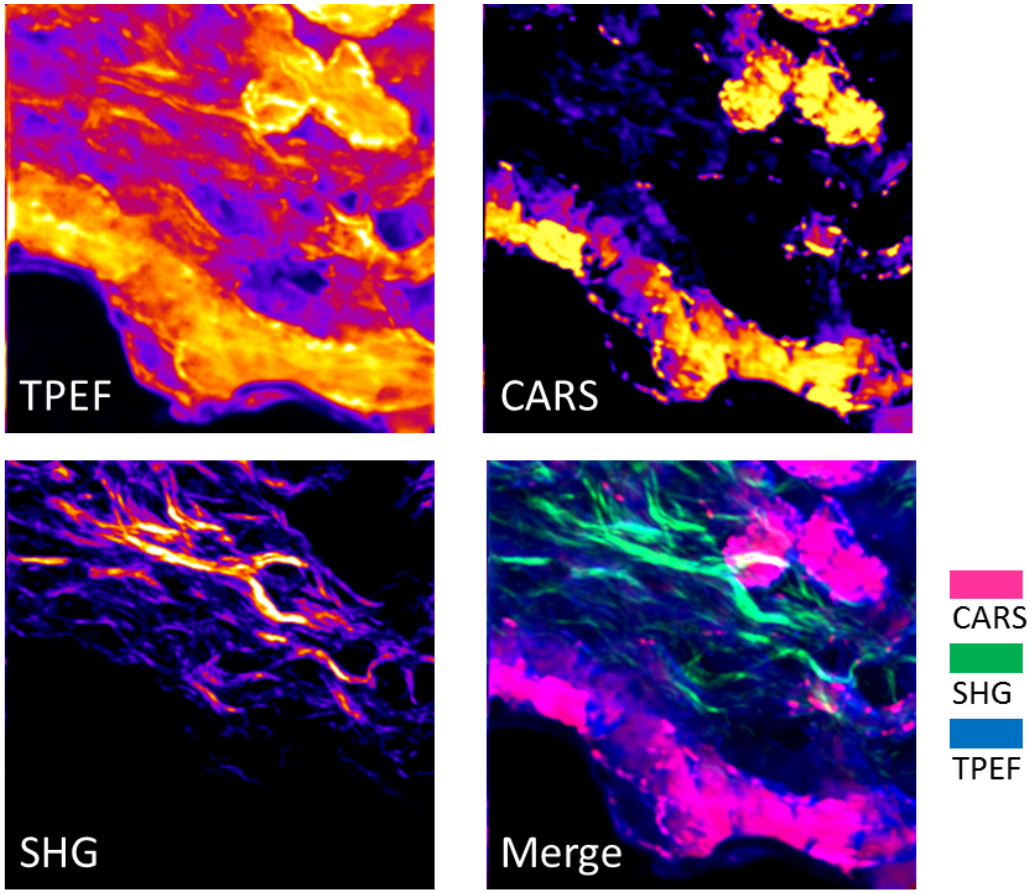

Figure 4.6: Imaging mouse skin sample with fiber-delivered laser excitation, where TPEF/SHG/CARS images can be obtained at the same time in Epi-detection and shown here with false color. The merged image shows the distinction of those three contrasts. Image size: 100 μm $\times$ 100 μm (250 $\times$ 250 pixels).

4.5.3 Endoscope-like detection

The signal was then detected in mode (2) endoscope-like detection. The setup was operated as the same configuration as in mode (1) as well as the imaging configuration. The same region on the mice skin sample was imaged and shown in Fig. 4.7.

The TPEF/SHG/CARS images show similar information as the ones from Epi-detection, where the morphology of skin is shown in the TPEF image, the collagen fibers are shown in the SHG image and the lipid content is shown in the CARS image. However, many

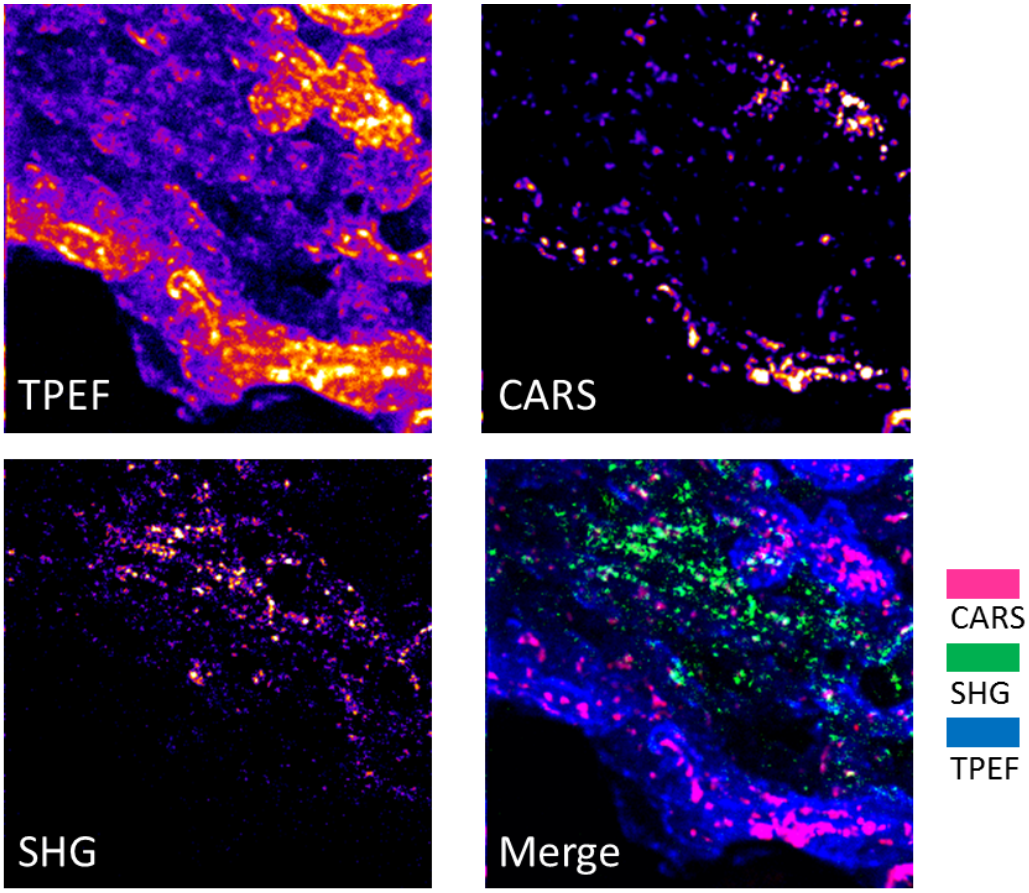

Figure 4.7: Imaging mouse skin sample (the same region as Fig. 4.6) by endoscope-like detection, TPEF/SHG/CARS images were obtained separately by adding proper filters and shown here with false color. The merged image shows the distinction of those three contrasts. Image size: 100 μm $\times$ 100 μm (250 $\times$ 250 pixels).

details of the sample are missing in those images. The fluorescence signal was relatively strong in skin compared with SHG and CARS, thus, the skin morphology imaged by TPEF is very similar than in Fig. 4.6, but the signal-to-noise ratio is hundreds times lower ($\sim$ 10). This represents the fact that, even under the same excitation condition in this system, only less than 1% of the signal collected in Epi-detection were collected in endoscope-like detection. Whereas in SHG and CARS images, not only the signal-to-noise ratio was extremely low (down to 2-3), but also a "discontinuous structure" was found in the images.

Comparing Epi-detection and endoscope-like detection, the images are of much lower quality from endoscope-like detection. First of all, the signal-to-noise ratio was hundreds times lower when the sample was imaged by the endoscope-like detection, which is mainly caused by the low collection efficiency since the sample was proved to be efficiently excited in this system. In this system, the scattered signal has to pass a long optical passway before arriving the detector, where a significant optical loss can be caused by mirrors, lenses, beam splitters, especially the scanning galvanometric mirrors. The signal loss can be also happened when it was collected back to the fiber due to its small numerical aperture (NA) and low transmission efficiency [177].

Another difference between images from these two detections is that a "discontinuous structure" was found in the endoscope-like detection. The TPEF images in both detections are of similar information, but the SHG and CARS images in endoscope-like detection show "discontinuous structure" where the information is partly missing. The reason is that, TPEF process is an incoherent process which causes homogeneous scattering in the backward direction, whereas SHG and CARS processes are coherent. Thus, in coherent processes, the signal was not scattered homogeneously in the backward direction depending on the structure of the sample, which is the phase-matching effect. However, in our system, the signal has to be collected in kagomé fiber core where the NA is extremely small (~ 0.01), so the scattered signal which is not inside the collection angle of the fiber core is cut by the fiber core. And also, the phase phase-matching is a necessary condition for strong signal to be obtained in coherent processes.

After all, the kagomé fiber shows many advantages for nonlinear imaging technique, and an "endoscope-like" system was developed with this fiber. The mice skin intrinsic fluorophores, collagen fibers and lipid can be imaged by TPEF, SHG and CARS respectively in this system, which represents the its potential for nonlinear endoscope development. However, the collection efficiency remains a challenge.

4.6 Conclusion and perspectives

The nonlinear microscopic imaging technique has been applied on human skin investigations in literature [18, 28, 29] and in this thesis (Chapter 2 and Chapter 3). In this

chapter, to break the limitation of observation depth and the flexibility of the equipments, the kagomé fiber is introduced to transfer nonlinear imaging techniques to an endoscope. An "endoscope-like" optical system was built based on this fiber and it was successfully applied on skin sample imaging.

A fixed mice skin sample was imaged in this chapter, two-photon excited fluorescence (TPEF), second harmonic generation (SHG) and coherent anti-Stokes Raman scattering (CARS) were applied to image the skin morphology, collagen distribution and lipid content respectively. The system shows that the excitation beams are efficiently delivered to the sample plane but the collection efficiency in the endoscope-like detection remains low due to the signal loss in the scanning microscope and the low numerical aperture of the fiber core. Even though, the nonlinear endoscopic imaging of multi-photon fluorescence and vibrational contrast moves from chemicals to biological tissues, which is one step closer to *in vivo* and clinical applications.

For the perspectives, concerning the problems remaining in the "endoscope-like" system, there are two aspects can be further improved in the future of this work.

(1) Fiber collection efficiency. Double-clad PCFs with solid core or hollow core have been previously demonstrated to significantly enhance the detection efficiency by incorporating a large multimode second cladding [179–181]. This concept can be also applied to kagomé fiber (see Fig. 4.8, IRCICA, Université Lille 1). In our experiments, the endoscope-like configuration collected hundreds of times less signal than Epi-detection under the same excitation condition, the signal loss was mostly caused by the collection efficiency, which is the key point to improve the image quality. The double-clad kagomé fiber in Fig. 4.8 has an outer cladding with a numerical aperture of 0.5, which means that it will collect $\sim 27\%$ of light emitted by a point source located in proximity to the fiber end face, this is around 30 time more than the signal can be collected by the fiber core. Besides, when the signal was collected by the second cladding, the light propagates though solid instead of air, thus, the transmission efficiency is much higher. Therefore, by adding a second cladding, the back reflected signal can be hopefully much more efficiently collected through the fiber.

(2) Fiber-optic scanning system. In the "endoscope-like" system, we used a scanning microscope at the fiber output side to scan the the focus point over the sample, which

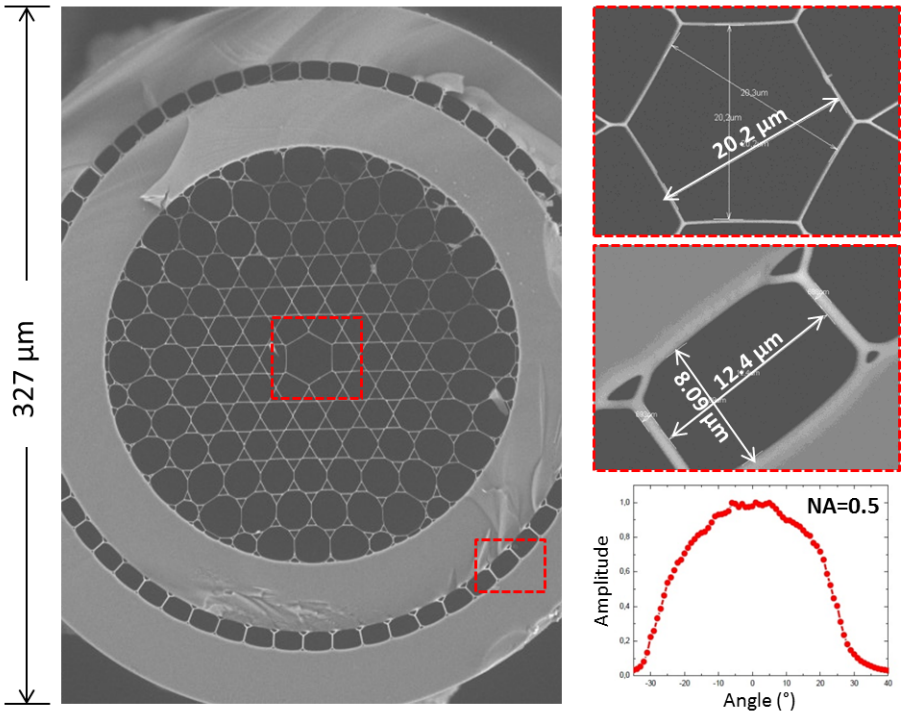

Figure 4.8: Double-clad kagomé fiber produced by IRCICA, Université Lille 1. The NA of the outer cladding is 0.5 which is much higher than the kagomé fiber core (~ 0.01)

not only caused a huge optical loss but also is not suitable for a practical endoscope. To develop an endoscope, fiber-optic scanning system is required to replace the scanning microscope. A fiber-optic scanning system has been designed and applied on two-photon fluorescence endoscope [178, 182], where a piezoelectric tube is used to move the fiber tip in X-Y plane, the beam is then magnified through a lens system (such as GRIN lens) and scans over the sample plane. Such a fiber-optic scanning system can be used to replace the scanning microscope in the "endoscope-like" system for the development of a real endoscope. This real endoscopic scheme would also eliminate many of the beam clipping issues present in the endoscope-like scheme.

In conclusion, the "endoscope-like" optical system developed in this chapter has proved the feasibility of the kagomé fiber based endoscope for nonlinear imaging on biological tissue. In the future, with the two achievable improvements proposed above, there stands a great chance of developing a real endoscope for nonlinear imaging which can be applied on skin research *in vivo* and the other clinical applications.

Conclusion and perspective

In this thesis, human skin, its appendages as well as cutaneous molecular penetration and absorption were investigated *in vitro* (reconstructed skin sample), *ex vivo* (excised skin sample) and *in vivo* (human palm), in a quantitative way using nonlinear spectroscopy and microscopy (two-photon excited fluorescence, TPEF, spontaneous Raman scattering, and coherent anti-Stokes Raman scattering, CARS). Furthermore, the nonlinear imaging technique has been transferred towards a proof-of-principle endoscopic system for skin imaging.

First of all, skin (reconstructed skin and excised skin) morphology and functionality were studied in 3D and the penetration of active molecules through skin barriers was demonstrated. We have designed a framework for imaging and reconstructing molecular concentration in complex skin samples using CARS and endogenous TPEF, to quantify and map active compound penetration in 3D. Studying reconstructed skin samples, we have highlighted the complex interplay between the diffusion through corneocyte "bricks" and the lipid "mortar" that dictate the penetration of active compounds depending on their hydrophobicity. On the other hand, excised human skin samples bring higher the degree of complexity with the appearance of diffusive barriers between epidermis and dermis compartments. This approach brings novel information in terms of active compound mapping and its relation with respect to the tissue organization.

Secondly, and more specifically in skin research, an individual sweat gland activity (SSGA) as well as the distribution and efficacy of antiperspirant salts (*in situ* Calcium Carbonate, *is*CC, and aluminum chlorohydrate, ACH) were studied *in vivo* on human palm. The morphology of a single eccrine sweat pore was imaged by TPEF microscopy and a 3D view of acrosyringium portion was reconstructed, where the funnel-like appearance of

sweat pore and the spiral shape of sweat duct in epidermis can be clearly distinguished. Afterwards, an "oil " regime was designed to monitor SSGA in real-time, with which the sweating process was observed and quantified in space and in time. Based on these methods, the penetration and localization of antiperspirant salts such as *is*CC and ACH inside sweat pore were studied, as well as their antiperspirant activity and mechanism were explored.

At last, to overcome the technical limitation (observation depth and setup flexibility) of nonlinear microscopy in skin research for further clinical applications, the nonlinear imaging technique was transferred to an endoscope with the help of hollow-core kagomé fibers. An "endoscope-like" optical system was developed based on this fiber and it was then applied successfully on skin sample imaging, where skin epidermis and dermis morphology, collagen distribution and lipid content were imaged by TPEF, SHG and CARS respectively. Therefore, the feasibility of transferring nonlinear imaging technique to a kagomé fiber based endoscope was demonstrated, which is one step closer to *in vivo* research and clinical applications.

Overall, nonlinear spectroscopy and microscopy have been proven to exhibit excellent label free contrast mechanism suitable for fast imaging. Multiphoton fluorescence can image biological tissue morphology using the intrinsic fluorophores while vibrational technique has the specific chemical selectivity. They have been applied on human skin investigations in literature [18, 20, 28, 29, 56] as discussed previously. Comparing with the reported studies, in this thesis (1) nonlinear spectroscopy and microscopy was applied for skin investigations, their applications were broadened especially for *in vivo* research; (2) Concerning specific subjects such as molecular absorption in epidermis or molecular distribution in sweat pore, proper innovative methods were proposed to solve specific problems; (3) Molecular cutaneous penetration and absorption were explored comprehensively and improved from a qualitative to a quantitative level. To our knowledge, it is the first time the concentration mapping can be achieved in 3D; (4) Nonlinear imaging technique was transferred to an endoscopic system and it was applied successfully on skin sample and not just chemicals, which lay a foundation for further *in vivo* skin research over the whole body and the other clinical applications. Therefore, this work takes nonlinear spectroscopy and microscopy one step further in the direction of quantitative analysis in skin research by its creativity and innovation, and perhaps leads to new technical development and biological applications in imaging research.

In order to understand all the mysteries of skin, different new methods are required according to specific subjects since skin is well known for its multiformity and complexity. For quantitative studies, more signal and image processing algorithms can be involved, for instance, cluster analysis based on Raman spectroscopy or CARS/SRS hyperspectral imaging. Finally, concerning clinical applications, an endoscope for nonlinear imaging is strongly demanded. Based on the "endoscope-like" optical system developed in this thesis, with further proposed improvements, there stands a great chance to develop a flexible nonlinear imaging endoscope for *in vivo* clinical applications.

Bibliography

[1] L. Sherwood. *Human Physiology: from cells to systems*. Yolanda Cossio, Belmont, CA 94002-3098, USA, 2010.

[2] M. Comel. *Fisiologia normale e patologica della cute umana*. Fratelli Treves Editori, Milan, Italy, 1953.

[3] W. Montagna and P. Parakkal. *The Structure and Function of Skin (third edition)*. Academic Press. INC, New York, 1974.

[4] G.K. Menon and A.M. Kligman. Barrier Functions of Human Skin: A Holistic View. *Skin Pharmacology and Physiology*, 22(4):178–189, 2009.

[5] M. Malpighi. *De externo tactus organo*. Neapoli, 1665.

[6] G.W. Hambrick and H. Blank. Whole mounts for the study of skin and its appendages. *Investigative Dermatology*, 23:437–453, 1954.

[7] J.A. Bouwstra, P.L. Honeywell-Nguyen, G.S. Gooris, and M. Ponec. Structure of the skin barrier and its modulation by vesicular formulations. *Progress in Lipid Research*, 42(1):1–36, 2003.

[8] G. Zonios, J. Bykowski, and N. Kollias. Skin Melanin, Hemoglobin, and Light Scattering Properties can be Quantitatively Assessed In Vivo Using Diffuse Reflectance Spectroscopy. *The Society for Investigative Dermatology*, 117(6):1452–1457, 2001.

[9] M. Ohmi, M. Tanigawa, Y. Wada, and M. Haruna. Dynamic analysis for mental sweating of a group of eccrine sweat glands on a human fingertip by optical coherence tomography. *Skin research and technology*, 0:1–6, 2003.

[10] M. Benzarti, M.B. Tkaya, C.P. Mattei, and H. Zahouani. Hair Mechanical Properties Depending on Age and Origin. *World Academy of Science, Engineering and Technology*, 5(2):418–424, 2001.

[11] R.L. Bronaugh, H.L. Hood, M.E.K. Kraeling, and J.J. Yourick. Determination of percutaneous absorption by in vitro techniques 2. *Cutaneous and Ocular Toxicology*, 20(4):423–427, 2001.

[12] F. Hueber-Becker, G.J. Nohynek, W.J.A Meuling, F. Benech-Kieffer, and H. Toutain. Human systemic exposure to a [14C]-para-phenylenediamine-containing oxidative hair dye and correlation with in vitro percutaneous absorption in human or pig skin. *Food and Chemical Toxicology*, 42(8):1227–1236, 2004.

[13] F.F. Sahle, S. Lange, B. Dobner, J. Wohlrab, and R.H. Neubert. Development and validation of LC/ESI-MS method for the detection and quantification of exogenous ceramide NP in stratum corneum and other layers of the skin. *J Pharm Biomed Anal*, 60:7–13, 2012.

[14] C. Herkenne, I. Alberti, A. Naik, Y.N. Kalia, F. Mathy, V. Preat, and R.H. Guy. In vivo methods for the assessment of topical drug bioavailability. *Pharmaceutical Research*, 25(1):87–103, 2008.

[15] C. Tran, J.F. Michelet, L. Simonetti, F. Fiat, A. Garrigues, A. Potter, E. Segot, R.E.B. Watson, C.E.M. Griffiths, and O.de Lacharriere. In vitro and in vivo studies with tetra-hydro-jasmonic acid (LR2412) reveal its potential to correct signs of skin ageing. *J Eur Acad Dermatol Venereol*, 28(4):415–423, 2013.

[16] S. El Gammal, C. El Gammal, K. Kaspar, C. Pieck, P. Altmeyer, M. Vogt, and H. Ermert. Sonography of the skin at 100 MHz enables in vivo visualization of stratum corneum and viable epidermis in palmar skin and psoriatic plaques. *Journal of Investigative Dermatology*, 113(5):821–829, 1999.

[17] J. Welzel, E. Lankenau, R. Birngruber, and R. Engelhardt. Optical coherence tomography of the human skin. *Journal of the American Academy of Dermatology*, 37(6):958–963, 1997.

[18] B.R. Masters, P.T. So, and E. Gratton. Multiphoton excitation fluorescence microscopy and spectroscopy of in vivo human skin. *Biophys J*, 72(6):2405–2412, 1997.

[19] W. Zipfel, R. Williams, R.Christie, and *et al.* Live tissue intrinsic emission microscopy using multiphoton- excited native fluorescence and second harmonic generation. *Proc Natl Acad Sci USA*, 100(12):7075–7080, 2003.

[20] K. Konig and I. Riemann. High-resolution multiphoton tomography of human skin with subcellular spatial resolution and picosecond time resolution. *Journal of Biomedical Optics*, 8(3):432–439, 2003.

[21] S.Y. Chen, H.Y. Wu, and C.K. Sun. In vivo harmonic generation biopsy of human skin. *Journal of Biomedical Optics*, 14(6):060505, 2009.

[22] A. Zumbusch, G.R. Holtom, and X.S. Xie. Three-Dimensional Vibrational Imaging by Coherent Anti-Stokes Raman Scattering. *Physical review letters*, 82(20):4142–4145, 1999.

[23] C.W. Freudiger, W. Min, B.G. Saar, S. Lu, G.R. Holtom, C. He, J.C. Tsai, J.X. Kang, and X.S. Xie. Label-free biomedical imaging with high sensitivity by stimulated Raman scattering microscopy. *Science*, 322(5909):1857–1861, 2008.

[24] P. Nandakumar, A. Kovalev, and A. Volkmer. Vibrational imaging based on stimulated Raman scattering microscopy. *New J. Phys.*, 11:033026, 2009.

[25] J.X. Cheng, Y.K. Jia, G. Zheng, and X.S. Xie. Laser-scanning coherent anti-Stokes Raman scattering microscopy and applications to cell biology. *Biophysical Journal*, 83(1):502–509, 2002.

[26] C.W. Freudiger, R. Pfannl, D.A. Orringer, B.R. Saar, and *et al.* Multicolored stain-free histopathology with coherent Raman imaging. *Laboratory Investigation*, 92(10):1492–1502, 2012.

[27] R. Mittal, M. Balu, T. Krasieva, E.O. Potma, and *et al.* Evaluation of Stimulated Raman Scattering Microscopy for Identifying Squamous Cell Carcinoma in Human Skin. *Lasers in Surgery and Medicine*, 45(8):496–502, 2013.

[28] B. Saar, L. Contreras-rojas, X. Xie, and R. Guy. Imaging Drug Delivery to Skin with Stimulated Raman Scattering Microscopy. *Molecular Pharmaceutics*, 8(3):969–975, 2011.

[29] N.A. Belsey, L.R. Contreras-Rojas, N.L. Garrett, J.J. Moger, G.J. Price, and R.H. Guy. Imaging drug delivery in the skin using coherent Raman scattering microscopy. *International Journal of Cosmetic Science*, 34(4):360–360, 2012.

[30] D.R. Rivera, C.M. Brown, D.G. Ouzounov, I. Pavlova, D. Kobat, W.W. Webb, and C. Xu. Compact and flexible raster scanning multiphoton endoscope capable of imaging unstained tissue. *Proceedings of the National Academy of Sciences*, 108(43):17598–17603, 2011.

[31] T.H. Tsai, J.G. Fujimoto, and H. Mashimo. Endoscopic Optical Coherence Tomography for Clinical Gastroenterology. *Diagnostics*, 4:57–93, 2014.

[32] H. Zeng. *Diagnostic Endoscopy.* Taylor & Francis Group. LLC, Boca Raton, 2014.

[33] F. Ganikhanov X.S. Xie, F. Legare and C. Evans. System and method for coherent anti-stokes raman scattering endoscopy., April 2007. Patent WO 2007047176 A2.

[34] Z. Chen, G. Liu, M. Balu, B. Tromberg, and E.O. Potma. System and method for efficient coherence anti-stokes raman scattering endoscopic and intravascular imaging and multimodal imaging, November 2013. US Patent 8582096 B2.

[35] B.G. Saar, R.S. Johnston, C.W. Freudiger, X.S. Xie, and E.J. Seibel. Coherent Raman scanning fiber endoscopy. *Optics letters*, 36(13):2396–2398, 2011.

[36] S. Brustlein, P. Ferrand, N. Walther, S. Brasselet, C. Billaudeau, D. Marguet, and H. Rigneault. Optical parametric oscillator-based light source for coherent Raman scattering microscopy: practical overview. *J Biomed Opt*, 16(2):021106, 2011.

[37] W. Zipfel, R. Williams, and W. Webb. Nonlinear magic: multiphoton microscopy in the biosciences. *Nature biotechnology*, 21(11):1369–1377, 2003.

[38] J.B. Pawley. *Handbook of Biological Confocal Microscopy (3rd Editon).* Sringer., Berlin, 2006.

[39] P. Török. *Optical Imaging and Microscopy.* Springer-Verlag Berlin Heidelberg New York, Germany, 2003.

[40] R.W. Boyd. *Nonlinear Optics (Third Edition).* Academic Press Inc., USA, 2008.

[41] W. Denk, JH. Strickler, and W. Webb. Two-photon laser scanning fluorescence microscopy. *Science*, 248(4951):73–76, 1990.

[42] B.E.A. Saleh and M.C. Teich. *Fundamentals of Photonics.* Jouhn Wiley & Sons, Inc., 1991.

[43] M. Goeppert-Mayer. Über elementarakte mit zwei quantensprüngen. *Annalen der Physik*, 401:273, 1931.

[44] I.D. Abella. Optical double-photon absorption in cesium vapor. *Phys. Rev. Letters*, 9:453, 1962.

[45] P.T.C. So, C. Dong, B. Masters, and K. Berland. Two-Photon Excitation Fluorescence Microscopy. *Annu. Rev. Biomed. Eng.*, 2:399–429, 2000.

[46] P. Theer, M.T. Hasan, and W. Denk. Two-photon imaging to a depth of 1000 μm in living brains by use of a Ti:Al_2O_3 regenerative amplifier. *Optics letters*, 23(12):1022–1024, 2003.

[47] K.H. Kim, C. Buehler, and P.T.C. So. High-speed, two-photon scanning microscope. *Applied Optics*, 38(28):6004–6009, 1999.

[48] J.B. Guild and W.W. Webb. Line scanning microscopy with two-photon fluorescence excitation. *Biophys. J.*, 68:290a, 1995.

[49] G.J. Brakenhoff, J. Squier, T. Norris, A.C. Bliton, W.H. Wade, and B. Athey. Real-time two-photon confocal microscopy using a femtosecond, amplified Ti:sapphire system. *J. Microsc.*, 181:253–259, 1996.

[50] J. Bewersdorf, R. Pick, and S.W. Hell. Multifocal multiphoton microscopy. *Opt. Lett.*, 23:655–657, 1998.

[51] A.H. Buist, M. Muller, J. Squier, and G.J. Brakenhoff. Real time two-photon absorption microscopy using multipoint excitation. *J. Microsc.*, 192:217–226, 1998.

[52] W.B. Amos and J.G. White. How the Confocal Laser Scanning Microscope entered Biological Research. *Biology of the Cell*, 95:335–342, 2003.

[53] J. Paoli, M. Smedh, A. Wennberg, and M.B. Ericson. Multiphoton Laser Scanning Microscopy on Non-Melanoma Skin Cancer: Morphologic Features for Future Non-Invasive Diagnostics. *Journal of Investigative Dermatology*, 128:1248–1255, 2007.

[54] B.R. Masters. *Confocal Microscopy and Multiphoton Excitation Microscopy: The Genesis of Live Cell Imaging.* SPIE Press Monograph, USA, 2006.

[55] A.J. Radosevich, M.B. Bouchard, S.A. Burgess, B.R. Chen, and E.M.C. Hillman. Hyperspectral in vivo two-photon microscopy of intrinsic contrast. *Optics Letters*, 33(18):2164–2166, 2008.

[56] H.A. El-Madani. *Microscopie multiphotonique in vivo chez l'homme: Application à l'analyse dynamique des modifications structurales et fonctionelles cutanées et à l'évaluation de la réponse thérapeutique*. PhD thesis, L'université Paris Diderot Paris 7, December 2011.

[57] F. Helmchen, M.S. Fee, D.W. Tank, and W. Denk. A Miniature Head-Mounted Two-Photon Microscope: High-Resolution Brain Imaging in Freely Moving Animals. *Neuron*, 31(6):903–912, 2001.

[58] R. Feynman. *The Feynman Lectures on Physics (Volume I): Mechanics.* Addison - Wesley, United States, 1964.

[59] P. Berto. *Microscopie et spectroscopie de phase. Développements en diffusion Raman cohérente (CRS) et en thermo-plasmonique.* Optique photonique et traitement d'image, Aix-Marseille University, January 2013.

[60] P. Klocek. *Handbook of Infrared Optical Materials.* MARCEL DEKKER, Inc., USA, 1991.

[61] N.B. Colthup, L.H. Daly, and S.E. Wiberley. *Introduction to Infrared and Raman Spectroscopy (3rd Edition).* Academic Press Inc., San Diego, 1990.

[62] S. Mukamel. *Principles of nonlinear optical spectroscopy.* Oxford University Press, 1995.

[63] C.V. Raman and K.S. Krishnan. A new type of secondary radiation. *Nature*, 121:501–502, 1928.

[64] G.S. Landsherg and L.I. Mandelstam. New phenomenon in scattering of light. *Journal of the Russian Physico-Chemical Society*, V60:335, 1928.

[65] N. Huang, M. Short, J. Zhao, H. Wang, and *et al.* Full range characterization of the Raman spectra of organs in a murine model. *Optics Express*, 19(23):22892–22909, 2011.

[66] C. Kendall, M. Isabelle, F. Bazant-Hegemark, J. Hutchings, L. Orr, J. Babrah, R. Baker, and N. Stone. Vibrational spectroscopy: a clinical tool for cancer diagnostics. *The Royal Society of Chemistry*, 134:1029–1045, 2009.

[67] H. Rigneault and E. Andresen. Fast and label-free. *Nature photonics*, 6:802–803, 2012.

[68] P. Maker and R. Terhune. Study of optical effects due to an induced polarization third order in the electric field strength. *Phys. Rev.*, 137:A801–818, 1965.

[69] M.D. Levenson, C. Flytzanis, and N. Bloembergen. Interference of resonant and nonresonant threee-wave mixing in diamond. *Physical Review*, B6:3962–3965, 1972.

[70] C.L. Evans and S. Xie. Coherent anti-Stokes Raman scattering microscopy: chemical imaging for biology and medicine. *Annual Review of Analytical Chemistry*, 1:883–909, 2008.

[71] H. Rigneault and D. Gachet. *Raman Imaging.* Chapter12: Background-free Coherent Raman Imaging: The CARS and SRS Contrast Mechanisms. Springer Series in Optical Sciences, 2012.

[72] R.L. Farrow, R.P. Lucht, G.L. Clark, and R.E. Palmer. Species concentration measurements using CARS with nonresonant susceptibility normalization. *Applied Optics*, 24(14):2241–2251, 1985.

[73] E.J. Woodbury and W.K. Ng. Ruby Laser Operation in Near IR. *Proceedings of the Institute of Radio Engineers*, 50:2347–2348, 1962.

[74] G. Eckhardt, R.W. Hellwarth, F.J. McClung, S.E. Schwarz, D. Weiner, and E.J. Woodbury. Stimulated Raman Scattering From Organic Liquids. *Physical Review Letters*, 9(11):455–457, 1962.

[75] M.D. Levenson and S.S. Kano. *Introduction to Nonlinear Laser Spectroscopy.* Academic Press, San Diego, 1988.

[76] J-X. Cheng and X.S. Xie. *Coherent Raman Scattering Microscopy.* CRC Press, USA, 2013.

[77] P. Kukura, D.W. McCamant, and R.A. Mathies. Femtosecond Stimulated Raman Spectroscopy. *Annual Review of Physical Chemistry*, 58:461–488, 2007.

[78] Y. Ozeki, F. Dake, S. Kajiyama, K. Fukui, and K. Itoh. Analysis and Experimental Assessment of the Sensitivity of Stimulated Raman Scattering Microscopy. *Optics Express*, 17(5):3651–3658, 2009.

[79] M.B.J. Roeffaers, X. Zhang, C.W. Freudiger, B.G. Saar, M. Ruijven, G. Dalen, C. Xiao, and X.S. Xie. Label-free imaging of biomolecules in food products using stimulated Raman microscopy. *J. Biomed. Opt.*, 16(2):021118, 2011.

[80] D. Fu, F. Lu, X. Zhang, C. Freudiger, D.R. Pernik, G. Holtom, and X.S. Xie. Quantitative Chemical Imaging with Multiplex Stimulated Raman Scattering Microscopy. *J. Am. Chem. Soc.*, 134(8):3623–3626, 2012.

[81] B.G. Saar, C.W. Freudiger, J. Reichman, C.M. Stanley, G.R. Hiltom, and X.S. Xie. Video-Rate Molecular Imaging in Vivo with Stimulated Raman Scattering. *Science*, 330(6009):1368–1370, 2010.

[82] C-R. Hu, D. Zhang, M.N. Slipchenko, J-X. Cheng, and B. Hu. Label-free real-time imaging of myelination in the Xenopus laevis tadpole by in vivo stimulated Raman scattering microscopy. *J. Biomed. Opt.*, 19(8):0086005, 2014.

[83] The university of Chicago Medicine. Genetics of skin cancer, 2014.

[84] R.K. Freinkel and D.T. Woodley. *The Biology of the Skin.* The parthenon publishing group Inc, New York, USA, 2001.

[85] K.M. Halprin. Epidermal 'Turnover Time' a Re-examination. *British Journal of Dermatology*, 86(1):14–19, 1972.

[86] G. Solanas and S.A. Benitah. Regenerating the skin: a task for the heterogeneous stem cell pool and surrounding niche. *Nature Reviews Molecular Cell Biology*, 15:737–748, 2013.

[87] F. Bernerd, C. Marionnet, and C. Duval. Solar ultraviolet radiation induces biological alterations in human skin in vitro: Relevance of a well-balanced UVA/UVB protection. *Indian Journal of D. V. L.*, 78(7):15–23, 2012.

[88] Z. Ya-Xian, T. Suetake, and H. Tagami. Number of cell layers of the stratum corneum in normal skin: relationship to the anatomical location on the body, age, sex and physical parameters. *Arch Dermatol Res.*, 291(10):555–559, 1999.

[89] P. Agache and P. Humbert. *Measuring the skin.* Springer - Verlag, Germany, 2004.

[90] J.M. Waller and H.I.Maibach. Age and skin structure and function, a quantitative approach (I): blood flow, pH, thickness, and ultrasound echogenicity. *Skin Res. Technol.*, 11(4):221–235, 2005.

[91] M. Lorencini, C.A. Brohem, G.C. Dieamant, N.I.T. Zanchin, and H.I. Maibach. Active ingredients against human epidermal aging. *Ageing Research Reviews*, 15:100–115, 2014.

[92] J.M. Waller and H.I.Maibach. Age and skin structure and function, a quantitative approach (II): protein, glycosaminoglycan, water, and lipid content and structure. *Skin Res. Technol.*, 12(3):145–154, 2006.

[93] M.J. Koehler, K. König, P. Elsner, R. Bückle, and M. Kaatz. In vivo assessment of human skin aging by multiphoton laser scanning tomography. *Optics letters*, 31(19):2879–81, 2006.

[94] Z.X. Jiang and J. DeLaCruz. Appearance benefits of skin moisturization. *Skin research and technology*, 17:51–55, 2011.

[95] Z. Merali. Human skin to replace animal tests. *New Scientist*, 2614:14, 2007.

[96] R. Roguet, C. Cohen, K.G. Dossou, and A. Rougier. Episkin, a reconstituted human epidermis for assessing in vitro the irritancy of topically applied compounds. *Toxic. in vitro*, 8(2):283–291, 1994.

[97] B.A. Vick and D.C. Zimmerman. Biosynthesis of Jasmonic Acid by Several Plant Species. *Plant Physiol*, 75:458–461, 1984.

[98] E.W. Chehab, R. Kaspi, T. Savchenko, H. Rowe, F. Negre-Zakharov, D. Kliebenstein, and K. Dehesh. Distinct Roles of Jasmonates and Aldehydes in Plant-Defense Responses. *PLoS one*, 3(4):e1904, 2008.

[99] R.A. Creelman and J.E. Mullet. Jasmonic acid distribution and action in plants: regulation during development and response to biotic and abiotic stress. *PNAS*, 92(10):4114–4119, 1995.

[100] E.E. Farmer and C.A. Ryan. Interplant communication: airborne methyl jasmonate induces synthesis of proteinase inhibitors in plant leaves. *Proc. Natl. Acad. Sci. USA*, 87(19):7713–7716, 1990.

[101] S. Cohen and E. Flescher. Methyl jasmonate: A plant stress hormone as an anticancer drug. *Phytochemistry*, 70(13-14):1600–1609, 2009.

[102] J.F. Michelet, C. Olive, E. Rieux, D. Fagot, L. Simonetti, J.B. Galey, M. Dalko-Csiba, B.A. Bernard, and R. Pereira. The anti-ageing potential of a new jasmonic acid derivative (LR2412): in vitro evaluation using reconstructed epidermis episkin^{TM}. *Experimental Dermatology*, 21:390–400, 2012.

[103] A. Leo, C. Hansch, and D. Elkins. Partition coefficients and their uses. *Chemical Reviews*, 71(6):525–616, 1971.

[104] H.I. Maibach M. Lodén. *Dry Skin and Moisturizers: Chemistry and Function*. CRC PRESS, Florida, US, 1999.

[105] W. Min, C.W. Freudiger, S. Lu, and X.S. Xie. Coherent nonlinear optical imaging: beyond fluorescence microscopy. *Annu Rev Phys Chem*, 62:507–530, 2011.

[106] A.J. Wright, S.P. Poland, J.M. Girkin, C.W. Freudiger, C.L. Evans, and X.S. Xie. Adaptive optics for enhanced signal in CARS microscopy. *Optics Express*, 15(26):18209–18219, 2007.

[107] G.K. Menon, G.W. Cleary, and M.E. Lane. The structure and function of the stratum corneum. *Int. J. Pharm.*, 435(1):3–9, 2012.

[108] A.M. Barlow, K. Popov, M. Andreana, D.J. Moffatt, and *et al.* Spatial-spectral coupling in coherent anti-Stokes Raman scattering microscopy. *Optics Express*, 21(13):15298–15307, 2013.

[109] J.X. Cheng, L.D. Book, and X.S. Xie. Polarization Coherent Anti-Stokes Raman Scattering Microscopy. *Optics Lett.*, 26:1341, 2001.

[110] D. Gachet, S. Brustlein, and H. Rigneault. Revisiting the Young's Double Slit Experiment for Background-Free Nonlinear Raman Spectroscopy and Microscopy. *Phys Rev Lett*, 104:213905, 2010.

[111] E.M. Vartiainen, H.A. Rinia, M. Müller, and M. Bonn. Direct extraction of Raman line-shapes from congested CARS spectra. *Optics Express*, 14(8):3622–3630, 2006.

[112] Y. Liu, Y.J. Lee, and M.T. Cicerone. Broadband CARS spectral phase retrieval using a time-domain Kramers-Kronig transform. *Opt. Lett.*, 34:1363, 2009.

[113] E.O. Potma and X.S. Xie. Detection of single lipid bilayers with coherent anti-Stokes Raman scattering (CARS) microscopy. *Journal of Raman Spectroscopy*, 34(9):642–650, 2003.

[114] X. Chen, S. Grégoire, F. Formanek, J-B Galey, and H. Rigneault. Quantitative 3D molecular cutaneous absorption in human skin using label free nonlinear microscopy. *Journal of Controlled Release*, 200:76–86, 2015.

[115] H.J.V. Merali. The Origin and Present Status of Fick's Diffusion Law. *Journal of Chemical Education*, 41(7):397–400, 1964.

[116] C. Herkenne, A. Naik, Y.N. Kalia, J. Hadgraft, and R.H. Guy. Pig Ear Skin ex Vivo as a Model for in Vivo Dermatopharmacokinetic Studies in Man. *Pharmaceutical Research*, 23(8):1850–1856, 2006.

[117] C. Herkenne, A. Naik, Y.N. Kalia, J. Hadgraft, and R.H. Guy. Ibuprofen Transport into and through Skin from Topical Formulations: In Vitro/In Vivo Comparison. *Journal of Investigative Dermatology*, 127:135–142, 2007.

[118] F. Pirot, Y.N. Kalia, A.L. Stinchcomb, G. Keating, A. Bunge, and R.H. Guy. Characterization of the permeability barrier of human skin *in vivo*. *Proceedings of the National Academy of Sciences - PNAS*, 94(4):1562–1567, 1997.

[119] J. Crank. *Mathematics of diffusion.* 44–51. Oxford Univ., Oxford, 1975.

[120] F. Netzlaff, M. Kaca, U. Bock, E. Haltner-Ukomadu, P. Meiers, C.M. Lehr, and U.F. Schaefer. Permeability of the reconstructed human epidermis model Episkin® in comparison to various human skin preparations. *European Journal of Pharmaceutics and Biopharmaceutics*, 66:127–134, 2007.

[121] X. Wen, Z. Mao, Z. Han, W.Tuchin, and D. Zhu. In vivo skin optical clearing by glycerol solutions: mechanism. *J Biophotonics*, 3(4):252, 2010.

[122] Y. Ozeki, W. Umemura, Y. Otsuka, and *et al.* High-speed molecular spectral imaging of tissue with stimulated Raman scattering. *Nature Photonics*, 6:845–851, 2012.

[123] F. Netzlaff, C.M. Lehr, P.W. Wertz, and U.F. Schaefer. The human epidermis models EpiSkin®, SkinEthic® and EpiDerm®: An evaluation of morphology and their suitability for testing phototoxicity, irritancy, corrosivity, and substance transport. *J Biomed Opt*, 60:167–178, 2005.

[124] Y. Dancik, M.A. Miller, J. Jaworska, and G.B. Kasting. Design and performance of a spreadsheet-based model for estimating bioavailability of chemicals from dermal exposure. *Advanced Drug Delivery Reviews*, 65(2):221–236, 2013.

[125] H.G. Breunig, M. Weinigel, and *et al.* Clinical coherent anti-Stokes Raman scattering and multiphoton tomography of human skin with a femtosecond laser and photonic crystal fiber. *Laser Physics Letters*, 10(2):025604, 2013.

[126] N. A. Taylor and C.A. Machado-Moreira. Regional variations in transepidermal water loss, eccrine sweat gland density, sweat secretion rates and electrolyte composition in resting and exercising humans. *Extreme Physiology & Medicine*, 2:4:1–29, 2013.

[127] K. Sato and R.L. Dobson. Regional and individual variations in the function of the human eccrine sweat gland. *The Journal of Investigative Dermatology*, 54(6):443–449, 1970.

[128] T. Ichihashi. Method of observing sweat drops on the skin covered with oil, and several observations with this method. *J Orient Med*, 25:107–108, 1936.

[129] Y-S. Kim and Y-S. Yoon. The new diagnostic method for hyperhidrosis using digital infrared thermographic imaging. *Clin Neurol Neurosurg*, 99:S156, 1997.

[130] D.S. Gomez, U. Mariani, A.A. Leirner, M. Mazzetto, J.R. Sampel, and M.C. Ferreira. A new method for acoring active sweat glands. *Clinics*, 60(6):505–506, 2005.

[131] E. Jonathan. In vivo sweat film layer thickness measured with Fourier-domain optical coherence tomography (FD-OCT). *Optics and Lasers in Engineering*, 46:424–427, 2008.

[132] J. Lee, M. Pyo, S h. Lee, J. Kim, M. Ra, W-Y. Kim, B.J. Park, C.W. Lee, and J-M. Kim. Hydrochromic conjugated polymers for human sweat pore mapping. *Nature Communications*, 5(3736):1–10, 2014.

[133] T. Ogawa and J. Sugenoya. Pulsatile sweating and sympathetic sudomotor activity. *Jpn J Physiol*, 43(3):275–289, 1993.

[134] A.K. Shamsuddin and T.Togawa. Continuous monitoring of single-sweat-gland activity. *Physiol Meas*, 21(4):535–540, 2000.

[135] K. Wilke, A. Martin, L. Terstegen, and S.S. Biel. A short history of sweat gland biology. *International Journal of Cosmetic Science*, 29:169–179, 2007.

[136] P. Schiefferdecker. Die Hautdrüsen des Menschen und der Säugetiere, ihre biologische und rassenanatomische Bedeutung, sowie die Muscularis sexualis. *Zoologica*, 27:1–154, 1922.

[137] K. Sato and R. Leidal amd F. Sato. Morphology and development of an apoeccrine sweat gland in human axillae. *Am J Physiol*, 252:166–180, 1987.

[138] D.L. Bovell, A.D. Corbett, S. Holmes, A. MacDonald, and M. Harker. The absence of apoeccrine glands in the human axilla has disease pathogenetic implications, including axillary hyperhidrosis. *British journal of dermatology*, 156:1278–1286, 2007.

[139] K. Sato. The physiology, pharmacology, and biochemistry of the eccrine sweat gland. *Rev Physiol Biochem Pharmacol*, 79:51–131, 1977.

[140] J.L. Bolognia, J.L. Jorizzo, and J.V. Schaffer. *Dermatology (3rd edition).* 44–51. Elservier Health Sciences, USA, 2012.

[141] K. Sato, W.H. Kang, K. Saga, and K.T. Sato. Biology of sweat glands and their disorders. I. Normal sweat gland function. *Journal of American Academy of Dermatology*, 20(4):537–563, 1989.

[142] K. Sato and F. Sato. Individual variations in structure and function of human eccrine sweat gland. *American Journal of Physiology*, 245(2):R203–R208, 1983.

[143] J.B. Holyoke and W.C. Lobitz. Histologic Variations in the Structure of Human Eccrine Sweat Glands. *The Journal of Investigative Dermatology*, 18:147–167, 1952.

[144] I.N. Bankman. *Handbook of medical image processing and analysis*. Elsevier, USA, 2009.

[145] E. Jürgensen. Mikrobeobachtungen der Schweisssekretion der Haut des Menschen unter Kontrastfärbung. *Deutsch. Arch. f. klin. Med.*, 144:193–201, 1924.

[146] G.R. Brisson, P. Boisvert, F. Peronnet, H. Perrault, D. Boisvert, and J.S. Lafond. A simple and disposable sweat collector. *Eur J Appl Physiol*, 63:269–272, 1984.

[147] C.L. Johnson and M.M. Landon. Eccrine sweat gland activity and racial differences in resting skin conductance. *Phychophysiology*, 1(4):322–329, 1965.

[148] A. Silver, W. Montagna, and I.Karacan. Age and sex differences in spontaneous, adrenergic and cholinergic human sweating. *The journal of investigative dermatology*, 43:255–265, 1964.

[149] V. Provitera, M. Nolano, G. Cporaso, A. Stancanelli, L. Santoro, and W.R. Kennedy. Evaluation of sudomotor function in diabetes using the dynamic sweat test. *Neurology*, 1(74):50–56, 2010.

[150] J-B. Lee, T-W. Kim, Y-O. Shin, Y-K. Min, and H-M. Yang. Effect of the Heat-exposure on Peripheral Sudomotor Activity Including the Density of Active Sweat Glands and Single Sweat Gland Output. *Korean J Physiol Pharmacol*, 14(5):273–278, 2010.

[151] E. Holzle and A.M. Kligman. Mechanism of antiperspirant action of aluminum salts. *J Soc Cosmet Chem*, 30:279–295, 1979.

[152] H.H. Reller and W.L. Lueders. Pharmacologic and toxicologic effects of topically applied agents on the eccrine sweat glands. *Advances in Modern Toxicology*, 4:1–54, 1977.

[153] R.P. Quatrale, D.W. Coble, K.L. Stoner, and C.B. Felger. The mechanism of antiperspirant by aluminum salts II: Histological observations of human eccrine sweat glands inhibited by aluminum chlorohydrate. *J Soc Cosmet Chem*, 32:107–36, 1981.

[154] A.W. Stillians. The control of localized hyperhidrosis. *J. Americ. Med. Assoc.*, 67:2015, 1916.

[155] Y.F Shen. Enhanced antiperspirant salts stabilized with calcium and concentrated aqueous solutions of such salts., June 2001. US Patent 6245325 B1.

[156] J. Mattai, X. Tang, M. Holerca, and K. LaTonya. Antiperspirant compositions., October 2007. US Patent 20070110687 A1.

[157] W.B. Shelley and H.J. Hurley. Anhydrous antiperspirant composition, October 2008. US Patent 7431918 B2.

[158] H. Lambers, S. Piessens, A. Bloem, H. Pronk, and P. Finkel. Natural skin surface pH is on average below 5, which is beneficial for its resident flora. *Int J Cosmet Sci.*, 28(5):359–370, 2006.

[159] O. Wunderlich, T. Frase, and B. Hughes-Formella. A Screening Technique for Antiperspirant Testing. *Cosmetics & Toiletries*, 118(12):59–62, 2003.

[160] T. Yanagishita, Y. Tamada, Y. Ohshima, K. Ito, Y. Akita, and D. Watanabe. Histological localization of aluminum in topical aluminum chloride treatment for palmar hyperhidrosis. *J. Dermatol. Sci.*, 67(1):69–71, 2012.

[161] O. Ceschaume, K.L. Shafran, and C.C. Perry. Interactions of Bovine Serum Albumin with Aluminum Polyoxocations and Aluminum Hydroxide. *Langmuir*, 22(24):10078–10088, 2006.

[162] C. Xu and F.W. Wise. Recent Advances in Fibre Lasers for Nonlinear Microscopy. *Nature Photonics*, 7:875–882, 2013.

[163] F. Helmchen and W. Denk. Deep Tissue Two-photon Microscopy. *Nature Methods*, 2:932–940, 2005.

[164] A. Bjarklev, J. Broeng, and A.S. Bjarklev. *Photonic crystal fiber*. Kluwer Academic Publishers, USA, 2003.

[165] F. Poli, A. Cucinotta, and S. Selleri. *Photonic Crystal Fibers: Properties and Applications*. Springer, USA, 2007.

[166] B.A. Flusberg, E.D. Cocker, W. Piyawattanametha, J.C. Jung, E.L.M. Cheung, and M.J. Schnitzer. Fiber-optic Fluorescence Imaging. *Nature Methods*, 2(12):941–950, 2005.

[167] K. Nagayama, M. Kakui, M. Matsui, I. Saitoh, and Y. Chigusa. Ultra-low-loss (0.1484 dB/km) pure silica core fibre and extension of transmission distance. *Electron. Lett.*, 38:1168–1169, 2002.

[168] A. Fuerbach, P. Steinvuzel, J.A. Bolger, A. Nulsen, and B.J. Eggleton. Nonlinear propagation effects in antiresonant high-index inclusion photonic crystal fibers. *Opt. Lett.*, 30:830–832, 2005.

[169] B. Kibler, T. Martynkien, M. Szpulak, C. Finot, J. Fatome, J. Wojcik, W. Urbanczyk, and S. Wabnitz. Nonlinear femtosecond pulse propagation in an all-solid photonic bandgap fiber. *Opt. Express*, 17:10393–10398, 2009.

[170] F. Légaré, C.L. Evans, F. Ganikhanov, and X.S. Xie. Towards CARS Endoscopy. *Opt. Express*, 14:4427–4432, 2006.

[171] M. Balu, G. Liu, Z. Chen, B.J. Tromberg, and Potma E.O. Fiber delivered probe for efficient CARS imaging of tissues. *Opt. Express*, 18(3):2380–2388, 2010.

[172] G.J. Pearce, G.S. Wiederhecker, C.G. Poulton, S. Burger, and P.St.J. Russell. Models for guidance in kagome-structured hollow-core photonic crystal fibres. *Optical Society of America*, 15(20):12680–12685, 2007.

[173] G. Humbert, J. Knight, G. Bouwmans, P. Russell, D. Williams, P. Roberts, and B. Mangan. Hollow core photonic crystal fiber for beam delivery. *Opt. Express*, 12(8):1477–1484, 2004.

[174] S-J. Im, A. Husakou, and J. Herrmann. Guiding properties and dispersion control of kagome lattice hollow-core photonic crystal fibers. *Optical Society of America*, 17(15):13050–13058, 2009.

[175] F. Benabid, J.K. Knight, G. Antonopoulos, and P.St.J. Russell. Stimulated Raman Scattering in Hydrogen-Filled Hollow-Core Photonic Crystal Fiber. *Science*, 298(5592):399–402, 2002.

[176] F. Couny, F. Benabid, and P.S. Light. Large-pitch kagome-structured hollow-core photonic crystal fiber. *Optics Letters*, 31(24):3574–3576, 2006.

[177] P. Ghenuche, S. Rammler, N.Y. Joly, M. Scharrer, M. Frosz, J. Wenger, P.St.J. Russell, and H. Rigneault. Kagome hollow-core photonic crystal fiber probe for raman spectroscopy. *Opt. Lett.*, 37:4371–4373, 2012.

[178] M.T. Myaing, D.J. MacDonanld, and X. Li. Fiber-optic scanning two-photon fluorescence endoscope. *Optics Letters*, 31(8):1076–1078, 2006.

[179] S. Brustlein, P. Berto, R. Hostein, P. Ferrand, C. Billaudeau, D. Marguet, A. Muir, J. Knight, and H. Rigneault. Double-clad hollow core photonic crystal fiber for coherent raman endoscope. *Optics Express*, 19(13):12562–12568, 2011.

[180] M.T. Myaing, J.Y. Ye, T.B. Norris, T. Thomas, J.R. Baker, Jr., W.J. Wadsworth, G. Bouwmans, J.C. Knight, and P.St.J. Russell. Enhanced two-photon biosensing with double-clad photonic crystal fibers. *Optics Letters*, 28(14):1224–1226, 2003.

[181] L. Fu, X. Gan, and M. Gu. Nonlinear optical microscopy based on double-clad photonic crystal fibers. *Opt. Express*, 13(14):5528–5534, 2005.

[182] Y. Zhao, H. Nakamura, and R.J. Gordon. Development of a versatile two-photon endoscope for biological imaging. *Optical Society of America*, 1(4):1159–1172, 2010.